THE EFFECT OF ACTIVE MASS THICKNESS ON THE CYCLE LIFE OF LOW-ANTIMONY LEAD-ALLOY SPINE EMPLOYED IN DEEP-CYCLE BATTERIES

by

VAN HAO NGUYEN

A THESIS

submitted in partial fulfillment of the requirements for the degree

MASTER OF ENGINEERING SCIENCE

School of Chemical Engineering
The Faculty of Engineering, Computer and Mathematical Science (EMCS)

THE UNIVERSITY OF ADELAIDE
South Australia

January 2015

Declaration

I certify that this work contains no material which has been accepted for the award of any other degree or diploma in my name, in any university or other tertiary institution and, to the best of my knowledge and belief, contains no material previously published or written by another person, except where due reference has been made in the text. In addition, I certify that no part of this work will, in the future, be used in a submission in my name, for any other degree or diploma in any university or other tertiary institution without the prior approval of the University of Adelaide and where applicable, any partner institution responsible for the joint-award of this degree.

I give my consent for this copy of my thesis, when deposited in the University Library, being made available for loan and photocopying, subject to the provisions of the Copyright Act 1968.

I also give permission for the digital version of my thesis to be made available on the web, via the University's digital research repository, the Library Search and also through web search engines, unless permission has been granted by the University to restrict access for a period of time.

Abstract

The cycle life of conventional starting-lighting-ignition (SLI) lead-acid batteries with low-antimony lead-alloy grids is reduced when subjected to repetitive deep-discharge cycling. Reduced cycle life is caused by the rich layer of lead sulfate formed in the corrosion layer interface (Barrett et al. 1981; Chang & Valeriote 1985). However, the cycle life of the tubular traction lead-acid batteries containing low-antimony lead-alloy grids is unknown when subjected to identical conditions.

Preliminary forensic analysis of a tubular traction cell subjected to similar conditions at Pacific Marine Batteries (PMB) indicates the reduced cycle life was caused primarily by corrosion of the positive grids which may have caused by stress created by the increased in the corrosion volume produced during cycling. Rogatchev, Papazov and Pavlov (1983) and Garche (1995) demonstrated that with increased in thickness of the active mass in tubular-plate formation of the corrosion product is reduced, hence reduce internal stress. Alternatively, Garche (1995) suggested the stress corrosion may be reduced by the partial compensation of the thickness of the active mass. Likewise, Chang and Valeriote (1985) recommended that low-antimony lead-alloy grids may be more suitable to be used in the design of tubular grids for deep-discharge cycling. They believed easy pathway for the acid to reach the grid surface was the main cause for the rich layer of lead sulfate to form. Therefore, further research is needed to provide insights into, and understanding of, the implication of the preliminary forensic analysis, hence help to extend the cycle life of the batteries.

Cells were assembled with a tubular positive electrode and one flat negative plate. Low-antimony lead alloys spines ~ 2.0 wt.% Sb with a diameter of ~3 mm was used. The independent variable studied was the effect of 1.60 mm, 2.15 mm and 2.80 mm active mass thickness on cycle life of the positive spines subjected to repetitive deep-discharge cycling. Cross-sections of cycled electrodes at different stages during cycling were examined for mode of failure using electron probe micro analysis (EPMA), secondary electron microscopy (SEM) images and iTEM5 image analysis software.

Average cell performance of cycled tubular electrode under 20 h discharge rates for various active mass thicknesses indicated the capacity was not exhibit sign of rapid reduced capacity. Back-scattered electron images and quantitative electron microprobe analysis were used to investigate the elemental distribution of sulfur (S present as sulfate) in the corrosion layer interface have provided no evidence of rich layer of lead sulfate formation in the corrosion layer.

The results from the residual cross-sectional areas indicated that corrosion failure result from stresses was the primary cause of the positive spine of low-antimony lead-alloy tubular-plate traction batteries subjected to repetitive discharge cycling. The effect of the active mass thickness on positive grid corrosion (cycle life) was inconclusive due inconsistent data when subjected to repetitive deep-discharging cycling.

Acknowledgement

This thesis would not have eventuated without the help and support from a number of people, including the company for which I currently work who have contributed significantly to this research and I would like to express my gratitude to all.

PMB Defence for their encouragement and for providing the opportunity and support to further improve my study and knowledge which may be helpful for the company and my own achievement.

Associate Professor Brian O'Neill, School of Chemical Engineering, University of Adelaide, my principal supervisor, for his precious time to support, guide and assist my thesis writing.

Mr. Peter Chaplin, PMB Defence Engineer, my ex-manager and external supervisor, who has encouraged me to complete my Master Degree, and for his ideas and support to build test equipment to conduct this research.

Mr. Brenton Swansson, my current manager, who allowed me to conduct this research in the Laboratory and during work hours.

Ms. Rosalie Louey, PMB Defence Engineer, my current work colleague at PMB and Mr. Rocky Caruso, Exide Technologies, my ex-work colleague at Exide for their technical review of my thesis.

I would like to dedicate this thesis to my parents, wife (Jasmine) and sons (Jamie & Jordan) for their endless love and support.

I hope the results of my thesis would provide some contribution to PMB Defence and to society.

Table of Contents

List of Figures

List of Tables

Nomenclature

%	percentage
μm	micro meter
A	ampere
Ah	ampere hour
g	gram
h	hour
kg	kilogram
kV	kilovolt
ml	millilitre
mm	millimetre
V	volt
α	alpha
β	beta

Abbreviations

BEVs	battery electrical vehicles
BSE	backscattered electron
C/D	charge/discharge
CL	corrosion layer
DCSL	dense corrosion sub-layer
EPMA	electron micro-probe analysis
g/cc	gram per cubic centimetre
LAB	lead-acid battery
MAN	mean atomic number
Me	metal
NAM	negative active mass
PAM	positive active mass
PCSL	porous corrosion sub-layer
PMB	Pacific Marine Batteries
PVC	polyethylene vinyl chloride
sat.	saturated
SEM	scanning electron microscope
sp. gr.	specific gravity

tp	polarization time
v/v	volume/volume
WDS	wavelength-dispersive spectroscopy
wt.%	weight percentage
XRD	X-ray diffraction

Chemical abbreviations

Ag	silver
AgCl	silver chloride
Ca	calcium
H^+	hydrogen atom
H_2	hydrogen gas
H_2O	water
H_2SO_4	sulfuric acid
KCl	potassium chloride
O_2	oxygen
Pb	lead
Pb_3O_4	red lead powder
PbO	lead oxide
PbO_2	lead dioxide
$PbSO_4$	lead sulfate
Sb	antimony
Sn	tin

1 Introduction

Normally, traction lead-acid batteries with low-antimony lead-alloy grids for conventional starting-lighting-ignition (SLI) duties are used for less-severe cycling service (shallow depth-of-discharge). By contrast, higher antimony lead-alloy grids of conventional SLI containing 2 to 6 percent by weight of antimony (Sb) are generally used for more-severe cycling service (Prengaman 2009). However, when low-antimony or antimony-free lead-alloy grids for conventional SLI lead-acid batteries are subjected to repetitive deep-discharge cycling, their cycle life is drastically reduced (Barrett et al. 1981; Chang & Valorie 1985; Constanti, Hollenkamp, Koop & McGregor 1995; Berndt & Nijhawan 1976; Hollenkamp, Constanti, Koop & Apiiteanu 1994).

The current literature has shown when conventional SLI lead-acid batteries are used in traction applications and are subjected to repetitive deep-discharge cycling, cycle life is reduced due to passivation layer of lead sulfate formed in the corrosion layer interface surrounding the grid wire (Barrett et al. 1981; Chang & Valeriote 1985). Whereas for antimony-free tubular traction lead-acid battery employed under similar conditions, their cycle life is reduced due to poor conductivity caused by cracks formed between the corrosion layer and the metal interface (Prengaman 1995). However, Chang & Valeriote (1985) and Rogatchev et al. (1983) have indicated that cycle life can be improved using low-antimony lead-alloy tubular-plate configurations in conjunction with thicker active mass.

A forensic analysis of a decommissioned low-antimony lead-alloy tubular-plate traction cell at Pacific Marine Batteries (PMB) indicated that the reduced cycle life was caused primarily by corrosion of the positive grids which may be attributed by stress. This finding was contradicted to the literature. It is generally held that low-antimony or antimony-free lead-acid batteries have a short cycle life when used in deep-discharge cycling service. This prompted further investigation as there is very little information available on cycle life and the primary reasons for failures of low-antimony lead-alloy tubular-plate traction batteries subjected to repetitive deep-discharge cycling.

Therefore, the main objective of this study is to reconfirm the above preliminary finding. Secondly, to examine the effect of the active mass thickness on the cycle life which may be impacted by the present of either the lead sulfate passivation layer or primarily by corrosion. Test cells were constructed from the same batch of cast low-

antimony lead-alloy spines with varied active mass thickness . Cells were cycled under repetitive deep-discharge cycling. Individual cell performance was monitored and cross sections of cycled electrodes at different stages of cycle life are used to measure the reduced cross-sectional area of the spine. Scanning electron microscopy (SEM) equipped with electron probe micro capability for quantitative analysis was used to investigate the elemental distribution of sulfur, antimony, lead and oxygen across the corrosion layer and, in particular, focus on the characteristics of the corrosion layer interface to determine how it affects cycle-life and thus improve the service life of low-antimony lead-alloy tubular-plate traction batteries.

The materials and methods used in the conduct of this research are explained in Chapter 4.

2 Background

This section provides a brief historical overview of the key inventors, chronology and advances of the lead-acid battery (LAB) followed by an overview of improvements to its reserve capacity resulting from the introduction of various LAB plates.

2.1 Lead-acid battery background

The first rechargeable lead-acid battery (LAB) was invented by Raymond Gaston Plante´ in 1860. A photo of Gaston Plante´ is shown in Figure 1.

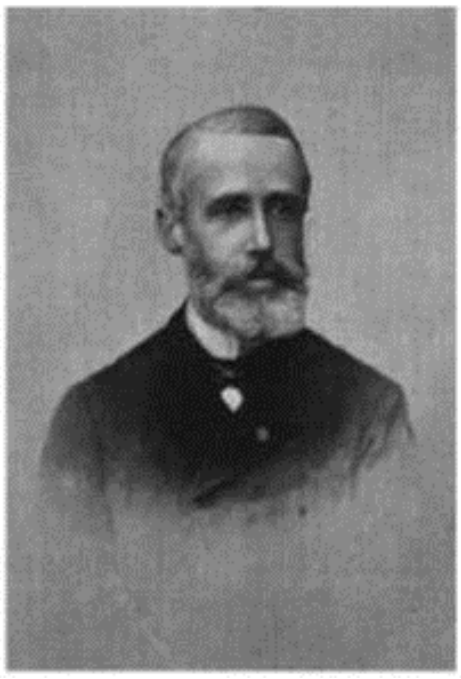

Figure 1- Portrait of Gaston Plante´ (Kurzweil 2010)

Plante´ constructed his first LAB using two long lead-foil strips wrapped with layers of cloth which he then immersed into a 10% (v/v) sulfuric acid solution. Unfortunately, the battery had very little capacity as there was no active mass to store reserve capacity. He conducted numerous experiments including corrosion of the lead foil to form active mass (illustrated in Figure 2) but the methods used to form the active mass were very ineffective. Consequently, attention turned to other methods to improve the reserve capacity and the production process, and in 1881 Faure introduced pasted lead foil electrodes using lead oxide-sulfuric pastes. Reserve capacity was significantly increased and Faure's pasted lead foil electrode was subsequently adopted and improved over the years.

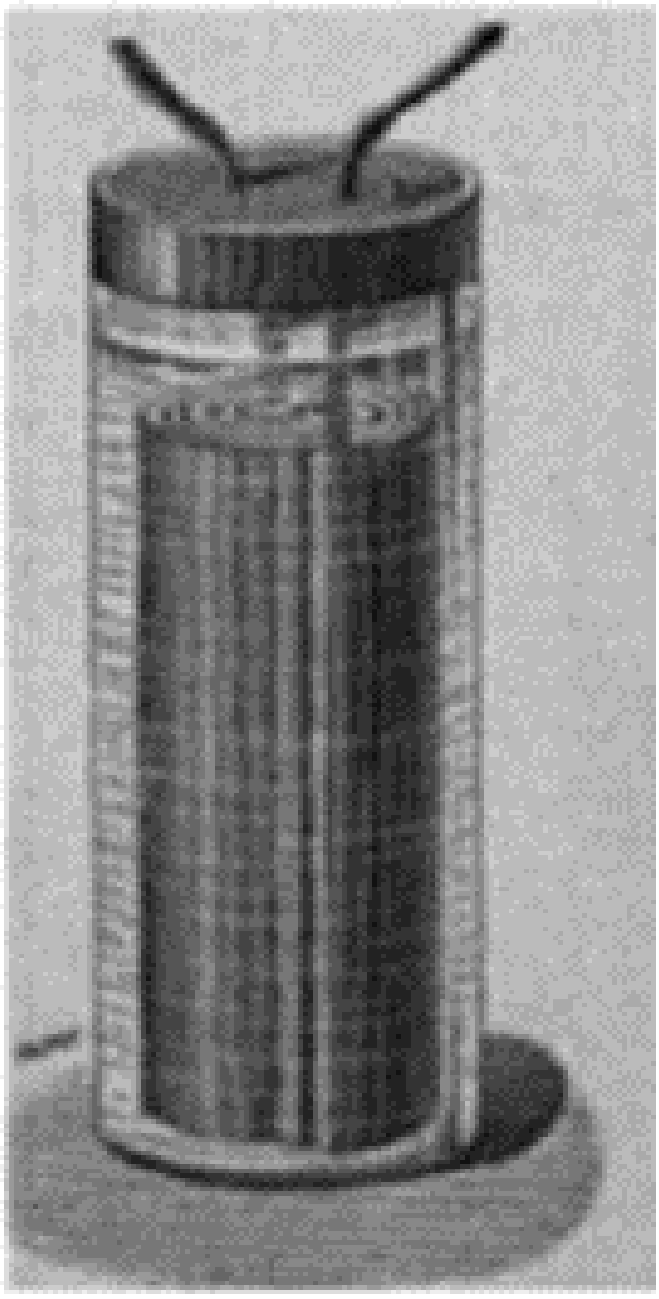

Figure 2 - Drawing of a secondary LAB cell with corroded coiled lead plates to illustrated the early development (Kurzweil 2010)

2.2 Construction of a lead-acid battery

The construction of batteries has significantly improved in both technology and design from the early tubular battery construction where the tubes are formed of hard rubber washers, piled upon one another (Figure 3) to the modern tubular construction which consists of woven retainer tubes (Figure 4). Battery performance and economics were significantly improved by replacing the hard rubber washers by woven retainer tubes (gauntlets). The tubes provided lower electrical resistance, better elasticity and higher acid diffusion rates.

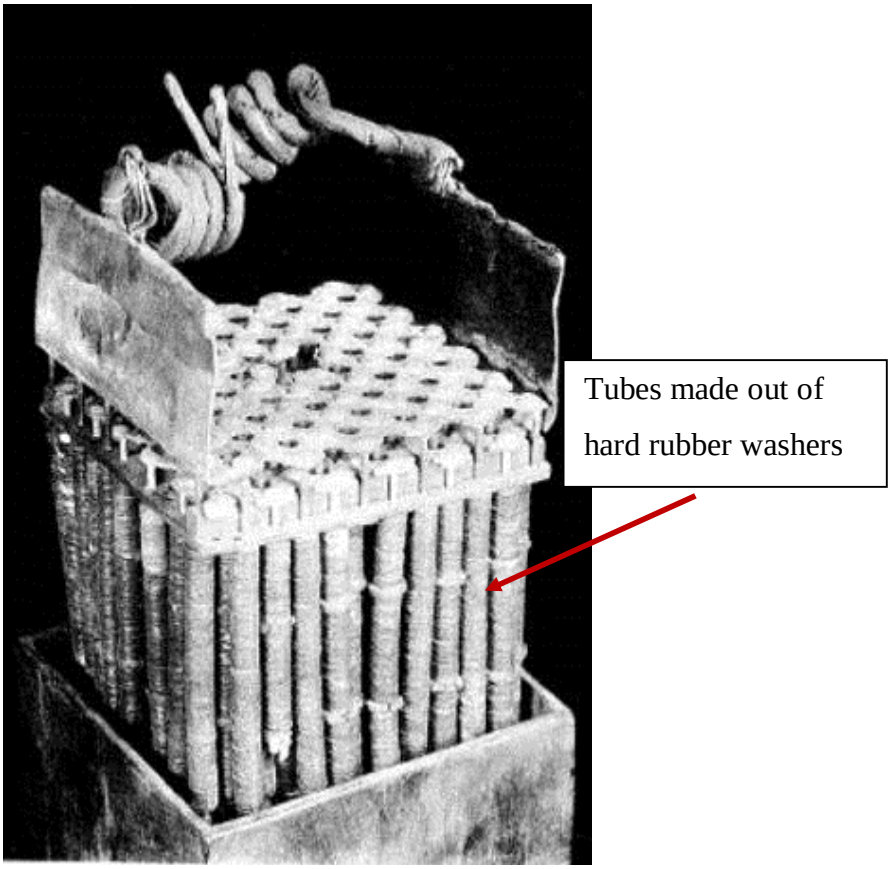

Figure 3 - Illustrates an early tubular battery constructed around 1900 using tubes of hard rubber washers piled upon one another (Ruetschi 1977)

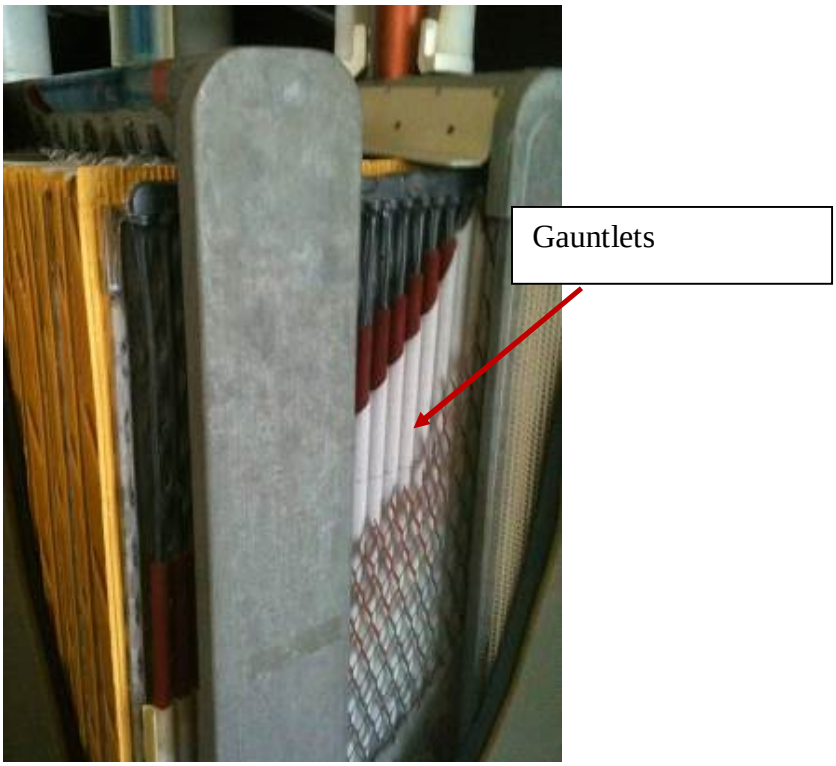

Figure 4 - Cut out section showing the inside of a modern traction, lead-acid battery with positive tubular-plate using gauntlets (Pacific Marine Batteries).

2.3 Plate types

Plates are the key components of the LABs as they provide reserve capacity. The dominant lead plates in current use are the pasted plate, introduced by Faure in 1881, and the tubular-plate, patented by S. Curie in 1890. Faure's pasted lead foil electrode has been adapted and improved over the years particularly by the introduction of the active mass which greatly increased its reserve capacity.

2.3.1 Flat pasted plate production

The process used to produce flat pasted plates has fewer steps and is simpler to manufacture than tubular-plates. To produce a flat pasted plate a wet paste mixture of lead oxide, water and sulfuric acid is constructed. The wet paste is then applied onto a cast or expanded lead grids (Figure 5) using a pasting machine and the plates are then"cured" in a curing oven. Curing is the process that converts the active mass in the plate into its desired chemical composition and its structural strength is developed (Figure 6).

Figure 5 - (a) Expanded grid (Pacific Marine Batteries) (b) cast grid (Exide Technologies) illustrating modern lead grid designs compared to a thin flat sheet of lead used for grid in early development.

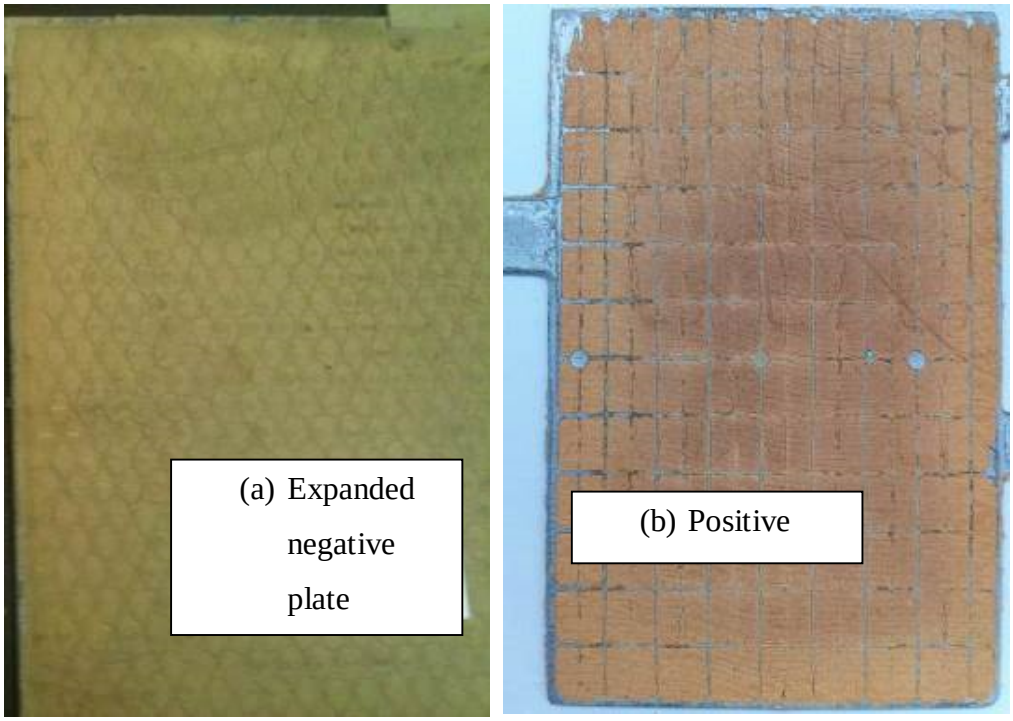

Figure 6 - Lead oxide pasted onto expanded and cast grids. (a) Dry unformed expanded negative flat plate (Pacific Marine Batteries) (b) Dry unformed flat positive plate (Exide Technologies)

2.3.2 Tubular-plate production

In this design of these plates, a central conducting 'spine' is surrounded by the active mass and the assembly is encased in a porous woven retainer tube known as the 'gauntlet'. The tubular-plate's design and manufacturing process are more complex than those for the flat pasted plate. First, a series of parallel lead spines are cast on to a bar composed of an antimonial lead alloy. Following casting, the gauntlet is fitted over the grid spines (Figure 7), and these tubes are then filled with a mixture of lead oxide and red lead powder by vibration. After the tubes are filled, the ends are sealed by knocking a plastic fitting onto the ends of the lead grid spines. The assembly is then "pickled" by soaking in a dilute sulfuric acid solution to convert the lead oxides into lead sulfate. The finished product contains a series of tubes filled with lead sulfate with a centre core of lead to carry the current (Figure 8).

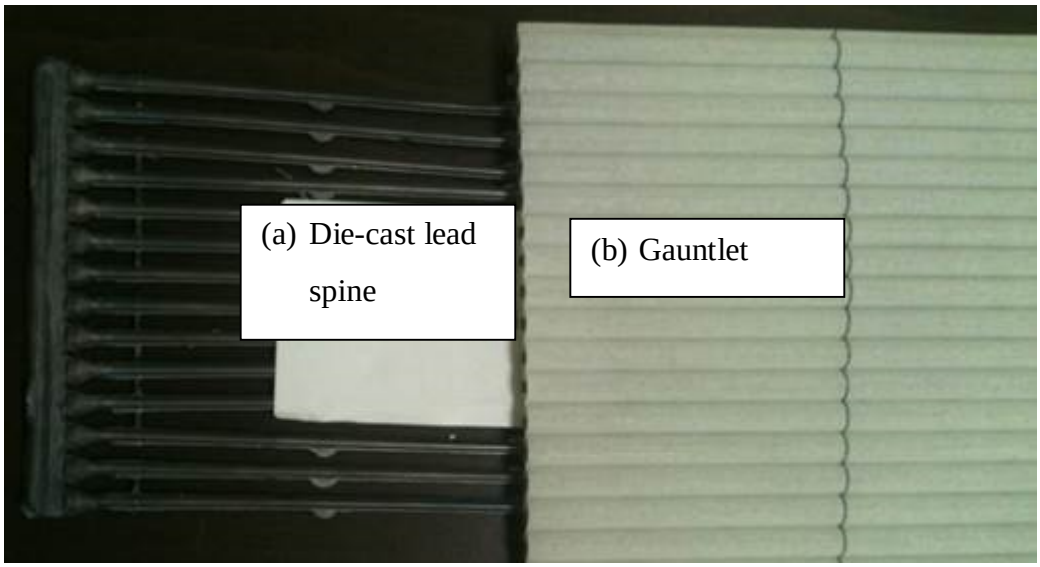

Figure 7 - Die-cast lead spine. (b) Gauntlet 'woven retainer tube'. (Pacific Marine Batteries)

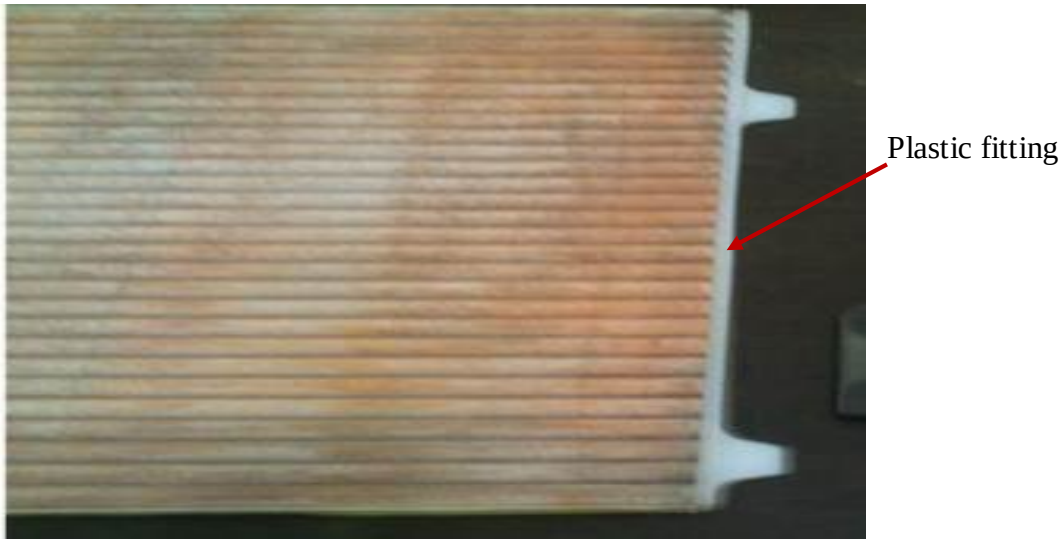

Figure 8 - Un-formed positive tubular-plate (Pacific Marine Batteries)

2.4 Chemistry of a lead-acid battery

The basic electrochemical process occurring at the positive and negative electrodes involves a dissolution-precipitation mechanism. The discharge-charge mechanism, known as double-sulfate reaction theory was first elucidated by Gladstone and Tribs in 1880 and may be summarised by equation (2-1). As the sulfuric acid (H_2SO_4) in the electrolyte is consumed during discharge, water is produced. The electrolyte is an ''active'' mass and may be designed as the capacity-limiting factor. When the cell approaches full charge, the majority of the lead sulfate ($PbSO_4$) is converted into a spongy lead (Pb) in the negative plate and to lead dioxide (PbO_2) in the positive plate. The cell's gassing voltage is approximately 2.39V per cell and any

overcharge voltage exceeding this limit results in a loss of water (H_2O) due to production of hydrogen (H_2) and oxygen (O_2).

The overall reaction summarizing the 'double sulfated theory' is summarised by:

Overall Equation	$Pb + PbO_2 + 2H_2SO_4 \leftrightarrow 2PbSO_4 + 2H_2O$	(2-1)
Cell Voltage	2.11V at 25°C	
12 Volt Battery	12.66V at 25°C	

2.5 Cycle life and the uses of traction lead-acid batteries

Traction lead-acid batteries are normally used for propulsion of battery electric vehicles (BEVs), forklifts, electric golf carts, ride-on floor scrubbers, electric motorcycles, full-size electric cars, trucks, and vans, and other electric vehicles. Traction batteries must be designed with a high ampere-hour capacity and be capable of tolerating sustained deep-discharge cycling.

The cycle life of a traction lead-acid battery depends on the depth-of-discharge and the number of cycles. Their capacity is normally rated at 5-hours. However, this rate may vary from 1 to 100-hours. A cycle life test rate of 20-hours is normally recommended. Lifetimes ranging from 500 to 1200 cycles are typical for a traction lead-acid battery at 80% depth-of-discharge (DOD). The principal failure mode for traction lead-acid batteries is caused by grid corrosion. However, in certain applications where low-antimony lead-alloy grids are employed as opposed to high-antimony lead-alloy grids, the battery's cycle life is reduced. The impact of low-antimony lead-alloy is discussed in the following literature review.

3 Literature review

In this chapter, the current state of literature of research is considered on:

- The influence of lead antimony alloy grids/spines employed in deep-cycle batteries.
- Stress in the positive plate.
- The effect of the active mass thickness on the cycle life of the positive grids/spines containing low-antimony lead-alloy employed in deep-discharge cycling.
- The measurement techniques of grid corrosion.

The aim of the review is to provide insights into, and an understanding of the implication of low-antimony lead-alloy grids/spines employed in traction lead-acid batteries under deep-discharge cycling.

3.1 Influence of antimony lead alloy grids employed in deep-cycle batteries

This chapter examines the influence of antimony on the cycle life of deep-cycle lead-acid batteries. The antimony content in the grids was kept constant, but it is necessary to understand its importance and its impact on the battery cycle life especially under deep-discharge cycling condition.

Low-antimony lead-alloy grids containing 1-2 wt.% Sb as opposed to higher 2-6 wt.% Sb grids are primarily employed in automotive batteries for starting-lighting-ignition (SLI) (Prengaman 2009). The low levels reduce potential migration of antimony to the negative plate. As well, this choice leads to reduced water loss and lower maintenance (topping up or refilling the battery's cells with water). By contrast, low-antimony lead-alloy grids are seldom employed for deep-discharge cycling. Unfortunately, this need for low maintenance introduces a design trade-off in which the cycle life is reduced (Barrett et al. 1981).

High antimony lead alloy composed of 9-12 wt.% Sb are used in cast long spine grids for tubular traction lead-acid batteries. These alloys have a low freezing range thereby allowing the liquid alloy to flow longer distances before solidification. These alloys

also exhibit excellent mechanical properties which enable easier handling of the cast long spine grids without deformation. In addition the presence of high levels of antimony in the corrosion layer permits the grid to recover from deep-discharge (Prengaman 2009). Other benefit of presence of antimony in the lead alloys is a slight restriction of the intensity of stress to minimise cracking in the corrosion layer. As well during cycling, the antimony leached from the lead alloys provides increased space for expansion volume created from the lead to lead dioxide change (Mahato 1979).

Numerous studies have confirmed that low-antimony lead-alloy is not recommended for application in traction lead-acid batteries undergoing deep-discharge cycling. Barrett et al. (1981) constructed lead-acid batteries with conventional design SLI from low-antimony lead-alloy grids ~2 wt.% Sb use for a traction duty. Their tests were performed with a duty cycle (extremely deep-cycle), based on a 20h rate down to a cut-off voltage of 1.58V. The researchers found that the capacity had fallen to 30% of the initial value after 70 cycles. They established the presence of a rich layer of lead sulfate in the corrosion layers surrounding the grid was the cause for the capacity to decline at a rapid rate. In addition, antimony was widely distributed throughout the plate mass but could not confirm if antimony paid a role in the formation of this sulfate layer.

Likewise, Chang and Valeriote (1985) experiments using book-mold cast lead-antimony alloys grids containing 3 wt.% Sb and these were cycled under deep-discharge cycle at 5-h rate to a potential of 900 mV against Hg/Hg_2SO_4 reference electrode. According to the authors, a 100% depth of discharge of discharge was achieved. The calculated discharge capacity dropped from 56% to 35% after 120 cycles. Clearly, the testing conditions and the capacity assessment were slightly different. Nevertheless, the results all indicated that the battery's cycle life performance was poor. Examination of the cycled plates using quantitative electron microprobe analysis found that lead sulfate surrounded the grid due to cracks in the corrosion layer around the grid.

Numerous research studies have confirmed that low lead-antimony alloy grids (1-2 wt.% Sb) batteries use for SLI duty repeatedly exhibited reduced capacity at a rapid rate under repetitive deep-discharge cycling (Constantia et al. 1995; Berndt & Nijhawan 1976; Hollenkamp et al. 1994). Figure 9 presents the discharge capacity plot of a low-antimony and antimony-free lead-acid battery that have been subjected to repetitive discharge. The discharge capacity has dropped to 50% of initial capacity after cycle number 65. These studies support the research of Barrette et al. (1981) and Chang and

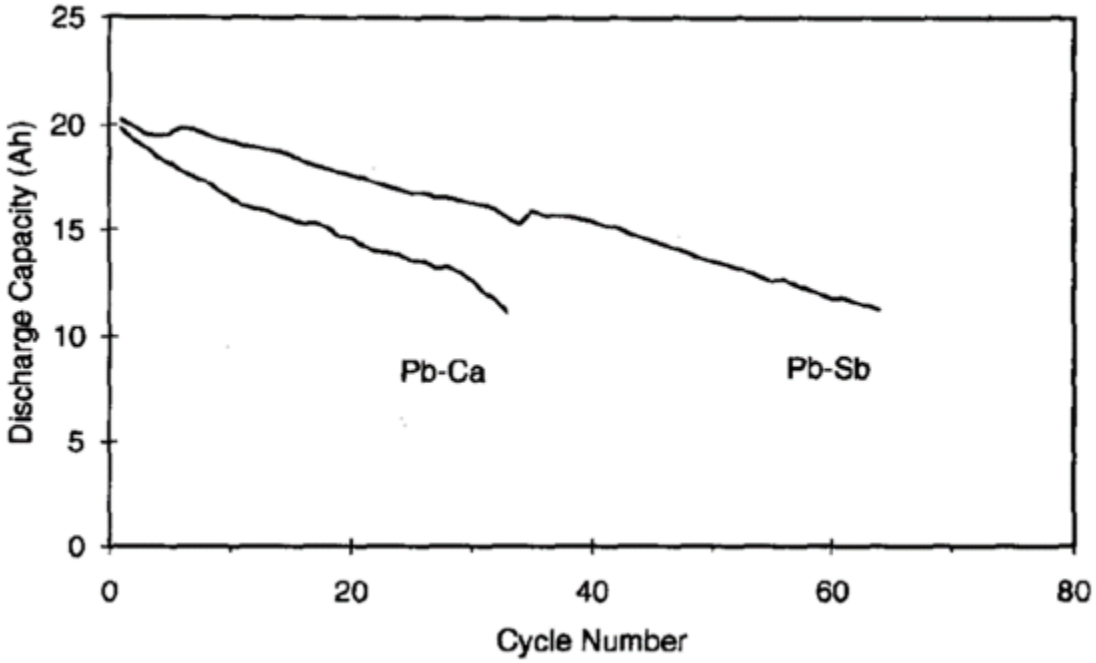

Figure 9 - Discharge capacity of low-antimony and antimony-free lead-acid battery under repetitive discharge (Hollenkamp et al. 1994)

Valeriote (1985) that the rich layer of lead sulfate surrounding the grid was the primary cause of poor cycle life for low-antimony lead-alloy SLI grids under repetitive deep-discharge cycling. Chang and Valeriote (1985) recommended that low-antimony lead-alloy grids may be more suitable to be used in the design of tubular grids for deep-discharge cycling. They believed the easy pathway for the acid to reach the grid surface was the main cause for the rich layer of lead sulfate to form. Furthermore, high concentration of H_2SO_4 around the β-PbO_2 corrosion layer was found to accelerate the formation of this passivation layer (Shiomi, Okada, Tsuboi, Ssumi & Tsubota 2003), and by eliminating this easy pathway, the rich lead sulfate layer surrounding the grid may be reduced or eliminated.

Figure 10 illustrates the concept of acid short cuts in a flat plate design. This plate was pasted using a conventional one-sided pasting machine and side (A) of the plate faced upwards on the pasting belt. The active mass has entirely covered the grid surface showing no exposed wires. Whereas, side (B) was facing down showing exposed wires which allowed easy pathways for acid to reach the grid surface.

In contrast, the spine is completely encapsulated by the active mass in a tubular-plate design (Figure 11) and there are no pathways for the acid to reach the grid surface. According to Pavlov (1995), this property may reduce the rate of reaction at the corrosion layer/electrolyte interface. Unfortunately, no follow up research was conducted by Chang and Valeriote (1985), or anyone else, in regard to tubular-plate

with low-antimony lead-alloy grids employed in deep-cycle applications. Clearly a gap exists to be further explored.

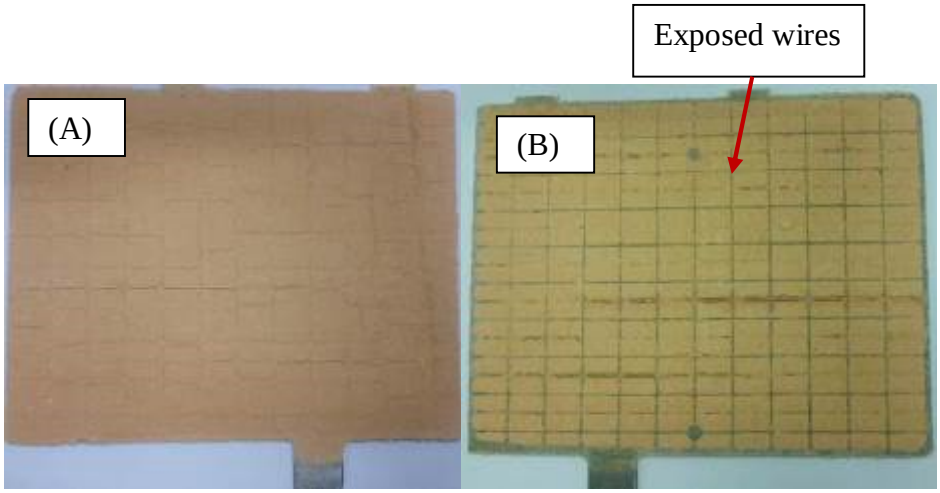

Figure 10 - Lead oxide pasted onto expanded and cast grids. (a) Dry unformed expanded negative flat plate (Pacific Marine Batteries) (b) Dry unformed flat positive plate (Exide Technologies)

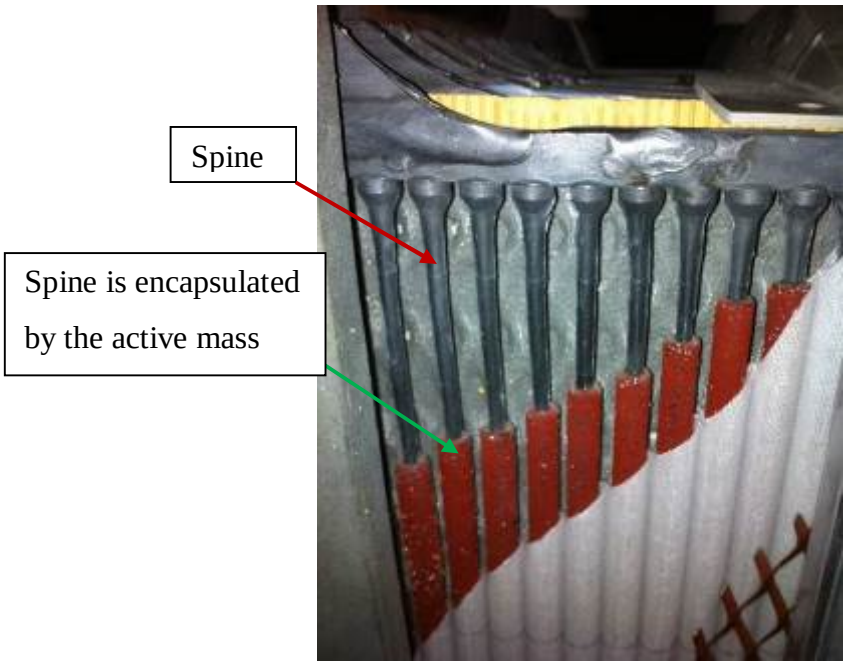

Figure 11 – Tubular-plate with central spines encapsulated by the active mass (PMB)

3.2 Stress in the positive electrode

As outlined in Section 1.0, the forensic analysis of low-antimony lead-alloy tubular-plate traction lead-acid cell at Pacific Marine Batteries (PMB) indicated that stress created by the increase in the volume of the corrosion product produced during cycling may have contributed to reduced cycle life. Therefore, concepts of how stress is formed and under what conditions will be explored in this section.

3.2.1 Lead spines corrosion

Metallic lead (Pb) in the spine of the positive plate is thermodynamically unstable and consequently it is readily oxidised from metallic lead to lead oxide/dioxide. Corrosion of the lead spines will lead to an increased resistance to current flow. The corrosion of the lead spines is influenced by stress. Stress occurs when lead is oxidised to PbO_2 generating a volume change, as will be explained in the following section.

3.2.2 Oxidation of lead and volume change and the relation to stress in the positive electrode

Stress is introduced into the corrosion layer by the greater volume of the corrosion product when lead is oxidised to PbO_2. Stress might lead to accelerated grid corrosion and may influence the cycle life of traction lead-acid batteries. Consequently it will be useful to understand the effect of stress and where it occurs.

The two key mechanisms of corrosion are:

(1) Oxidation via solid state diffusion (Rogatchev et al. 1983)

$$Pb + O_2 \rightarrow PbO_2 \qquad (3\text{-}1)$$

(2) Electrolyte corrosion

$$Pb + 2H_2O \rightarrow \alpha PbO_2 + 4H^+ \qquad (3\text{-}2)$$

$$2H_2O \rightarrow O_2 + 4H^+ \qquad (3\text{-}3)$$

Mechanism (1) is initiated by the penetration of oxygen into the PAM during charging. Oxygen then diffuses through the highly porous positive active mass (PAM) layer and oxygen evolution occurs at the interface of the lead spine and the PAM. The spine is oxidized to form a corrosion layer of lead dioxide (PbO_2), illustrated in equation (3-1).

Rogatchev et al. (1983) and Hollenkamp et al. (1994) supported the view that corrosion is caused by oxygen diffusing through the active mass during charging. As a result the grid is oxidised from Pb to PbO, PbO_n and PbO_2. However, Ruetschi (2004) suggests that an ion transport mechanism (2) across the corrosion layer is more likely to be involved. During cycling (charge-discharge) of a battery, water is adsorbed at the electrolyte/PbO_2 interface and transported to the PbO_2/Pb interface as summarised in reactions (3-2) and (3-3). In this theory, the transport rate of water provides the dominant influence on the corrosion rate. During the oxidation of lead to PbO_2, the theoretical molar volume is increased by 38%, and this increased volume creates stress. As the plate is cycled, the corrosion layer thickens until a critical value is reached (Ball,

Kurian, Evans & Stevens 2002; Simon 1967). Once this occurs, the corrosion layer (CL) is cracked due to stresses is developed as illustrated in Figure 12.

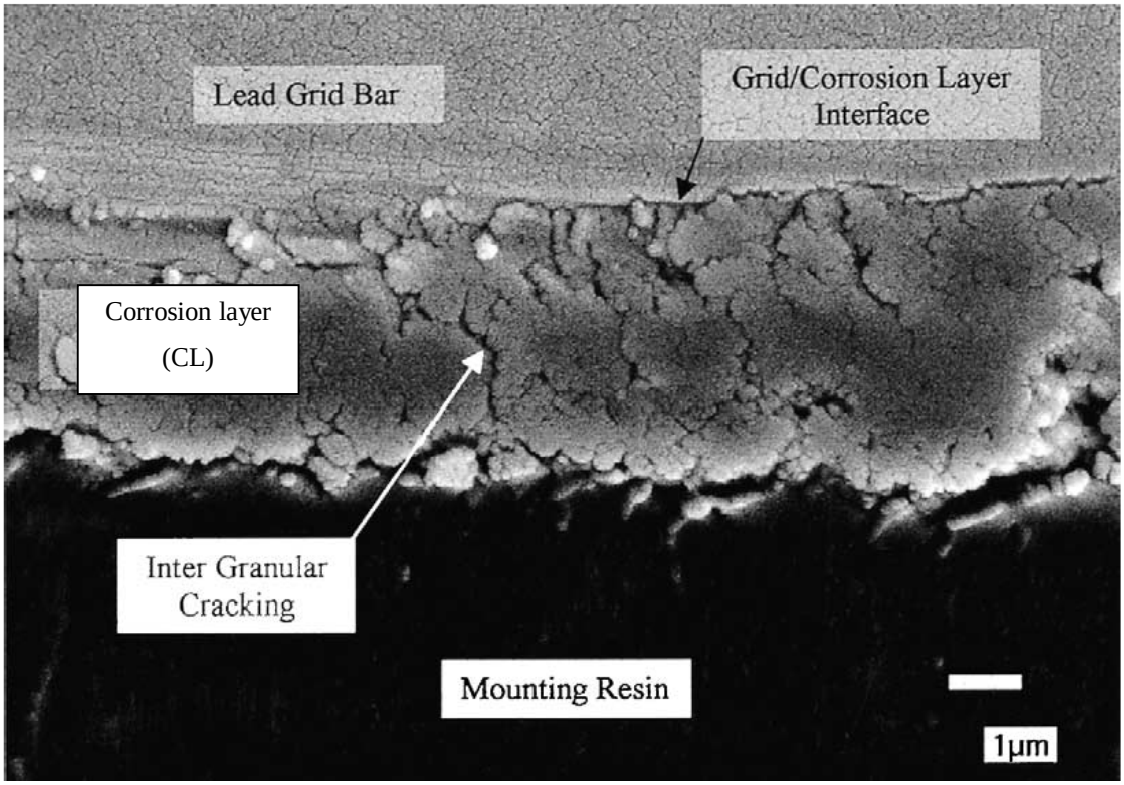

Figure 12 - SEM image of a grid corrosion layer interface for a cycled battery (Ball et al. 2002)

Pavlov (1994) and Mahato (1979) established that the corrosion layer consists of two distinct layers. The inner layer is dense, whilst the outer is porous, as illustrated in Figure 13. Microscopic studies confirm that the dense layer is closest to the spine (metal) surface. The dense layer is brownish and strongly adheres to the spine and it can only be chemically removed. The porous (or outer) layer lies between the dense layer and the active mass. This outer layer is porous, dark brown and loose. It has been described by Pavlov (1994) as a "*shapeless mass of small crystals bonded into porous aggregates with large pores in between*". The porous layer grows in thickness and sheds off. Consequently, the outer layer does not build up stress rather the stress build up in the denser layer (Simon 1967; Mohato 1979).

During oxidation, the dense layer forms first and it increases in size as the amount of current passed rises. The molar volume of PbO_2 38% larger than that for lead (Pb) and this volume change creates stresses in the dense corrosion layer (Ball et al. 2011). On the other hand, Alzieu and Robert (1986) and Constanti et al. (1995) suggested stress is influenced by an even greater molar volume change of 51% when $PbSO_4$ is formed

during deep-discharge. Furthermore Atlung and Christiansen (1990) established that the thickness of the plate increases from cycle to cycle due to expansion in volume of the corrosion product. Conversely, according to Simon (1967) the active mass does not causes stress despite the large volume change during charge-discharge cycling. Under microscopic examination of the corrosion product, he confirmed that only a portion of a very thin layer (roughly 10μm) of the corrosion product adjacent to the metal surface (inner corrosion layer) is creating stress. This hypothesis is also confirmed by Willihnganz (1988).

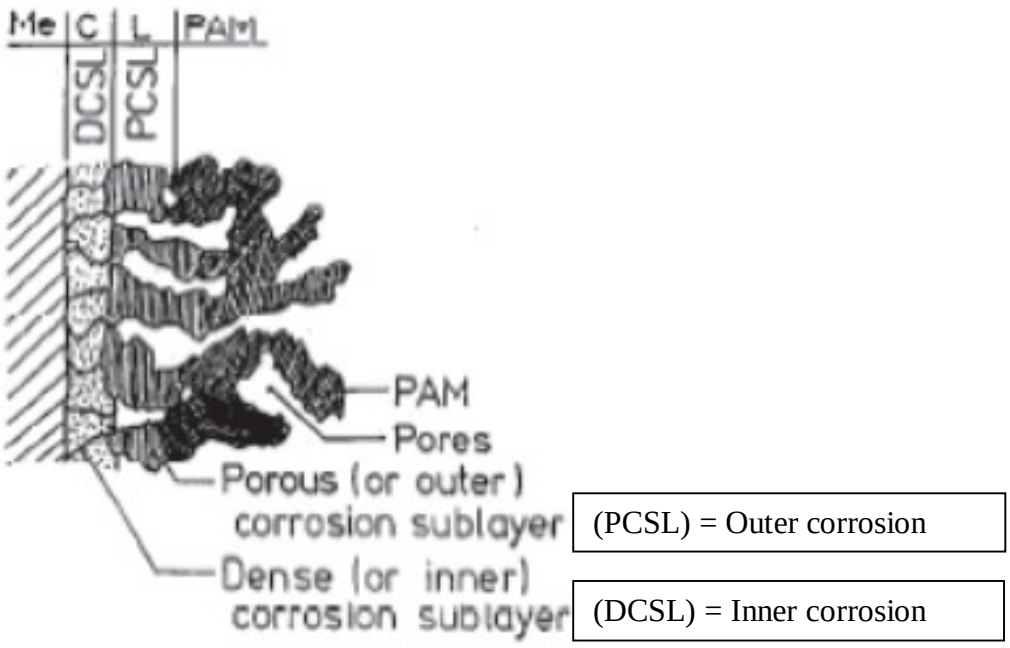

Figure 13 - Schematic representation of structure of corrosion layer (Pavlov 1994)

3.3 The effect of active mass thickness on cycle life of low-antimony lead-alloy spine employed in traction deep-cycle

Currently, there is no information available in the literature on the effect of the thickness of the active mass upon the cycle life of low-antimony lead-alloy employed in tubular-plate traction deep-cycle batteries. However, it has been established that an increase in thickness of active mass in a tubular-plate reduced grid/spine corrosion under continuous charge with current of 6 mA/cm^2 (Rogatchev et al. 1983; Garche 1995). The corrosion of the spines covered with 1 mm active mass thickness was half the corrosion of the bare spines, and grid corrosion was only affected by thicknesses up to 3 mm. Beyond 3 mm grid corrosion was only affected by the alloys. In addition, Rogatchev et al. (1983) has demonstrated that with an increased in thickness of the active mass in tubular-plate, the oxygen evolution decreases due to lower current

density. Another possibility for lower corrosion is the resistance of the electrolyte in the pores. As the thickness of the active mass increases, the pores become longer thereby reducing the concentration of the oxygen at the corrosion layer/electrolyte interface. This is consistent with the two mechanisms of stress as mentioned in Section 3.2. Alternatively, Garche (1995) suggested stress may be reduced by the partial compensation of the thickness of the active mass. Whilst, Simon (1967) revealed that the active mass has little effect on stress.

Nevertheless, the aim of Rogatchev et al. (1983) research was an examination of the effect of active mass thickness upon the tubular-plate on the corrosion rate under float charge conditions for batteries on standby applications. Therefore, the current was kept constant and the sole variable was the active mass thickness. In contrast, under discharge conditions the current is likely to be varied according to the surface area or the weight of the positive active mass (PAM). This effect of thickness active mass on the cycle life of low-antimony lead-alloy employed in tubular-plate traction deep-cycle is unknown and is addressed in this study.

3.4 Techniques for corrosion measurement

The degree of corrosion may be measured by a variety techniques, typically involving grid growth, cross-sectional area, or weight loss. The preferred technique varies, for example, grid growth was normally preferred over weight or cross-sectional area loss data by Giess (1985). He claimed this, "*because it appears to be more directly related to discharge performance and to eventually secondary damage of the cell container*". Lehockey, Limoges, Palumbo, Sklarchuk, Tomantschger & Vincze (1999) however used both weight and growth to study corrosion and growth resistance, while Ball et al. (2002) preferred cross-sectional area to examine the characteristics of the corrosion layer.

Some of the techniques are well documented in research papers. For instance Lander, Simon and Jones (1958); Rogatchev et al. (1981) and Garche (1995), used weight loss to investigate the corrosion rate of the spine under continuous polarization conditions. However, each research group used a different solvent to remove the corrosion layer. Another example is measurement of the cross-sectional area. Ball et al. (2002) determined corrosion layer thickness measurement using Optimas image analysis software, whereas Simon (1967) used cross-sectional area under SEM to establish the type of cracks occur in the corrosion layer. Finally, Barrette et al. (1981) also used

cross-sectional area to investigate elemental distributions in the grid, corrosion layer and the active mass.

Another important piece of information that can be deduced from the cross-sectional area measurement technique is the capability to forecast the service life of a tubular - plate lead-acid battery. This technique was briefly mentioned in Battrien (2002) with an illustration example as illustrated in Figure 14. It shows the theoretical residual cross-sectional area of the low-antimony lead-alloy spine after 15 years of service life under float charge condition. Thus the corrosion of the spine and the service life can be readily determined. Despite a lack information provided on how to obtain the cross-sectional area of the spine, this measurement technique is found very useful. The technique has been used effectively in circumstances where the spine is too brittle to be extracted, and the corrosion layer is detached making it difficult to measure its thickness. Given the current improvement in technologies using available image analysis software such as ImageJ (developed by Fuji) and iTEM5 (by Olympus), the technique was further developed to assist in attaining the residual cross-sectional area of a cycled spine tubular grid with precision and is simple to use.

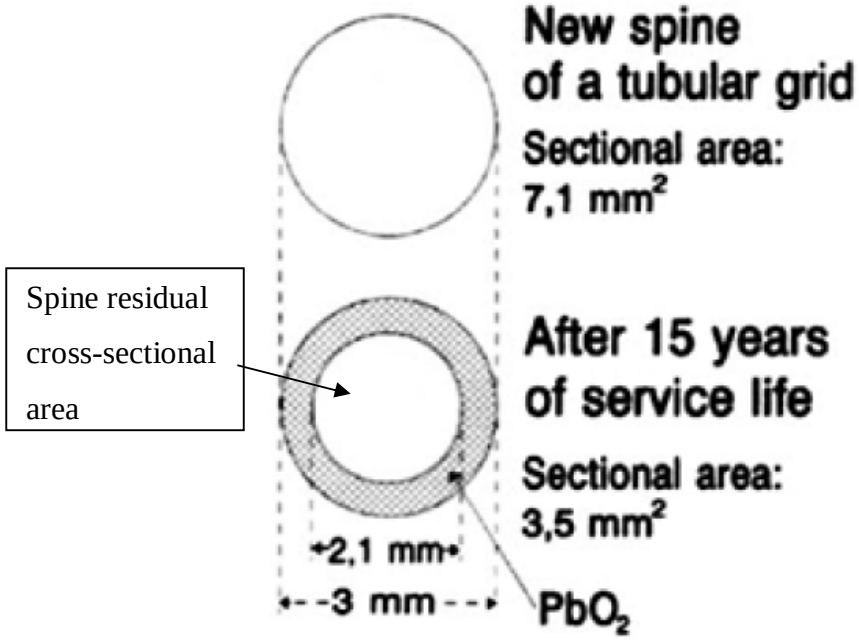

Figure 14 – Drawing illustrate a residual cross sectional area of the spine after 15 years of service under float charge condition (Battrien 2002)

3.5 Research gap

As outlined in Section 3.1, low-antimony lead-alloy grids containing 1-2 wt.% Sb opposed to 2-6 wt.% Sb are widely employed in conventional SLI batteries typically used in traction applications that are subjected to repetitive deep-discharge cycling. Unfortunately these grids exhibit reduced capacity at a rapid rate. A rich layer of lead sulfate which surrounds the grid has been confirmed to be the cause for this reduced capacity and cycle life. The easy pathways between the active mass and the grid mean that the acid quickly diffuses to the grid surface and is the primary cause for the rich layer of lead sulfate to form. In contrast to the conventional SLI grids, the tubular-plate with the spine is encapsulated by a thick layer of active mass which provides a significant barrier for acid to reach and attack the grid.

It has been well established that the corrosion rate of the spines covered with active mass of 1 mm thickness is half the corrosion rate of the bare spines and an increase thickness of the active mass reduces the corrosion rate. Unfortunately, reported tests were conducted under continuous charge conditions. This scenario is not relevant for traction lead-acid battery operating conditions. As a consequence the goal of this study will be to construct and test tubular electrode test cells to examine the influence of the active mass thickness on corrosion of the positive spines and cycle life under deep-discharge cycling.

Three common techniques are used to measure the degree of corrosion of the grids. However, using cross-section area to determine the residue of the spine in a tubular-plate is not documented. In addition, with image analysis software development such as ImageJ and iTEM5, this technique can be very useful as outlined in Section 3.4 above. This technique was developed to incorporate with the software which allowed the residue of cycled spine to be measured and the cycle life is postulated based on the corrosion of the spine.

3.6 Research objectives

The main objective of the current study is to improve understanding the cycle life of the positive spines containing low-antimony lead-alloy in tubular-plate lead-acid battery cells employed under repetitive deep-discharge cycling. Particular focus is on the characteristics of the grid corrosion layer and how it affects grid life and cell performance. The research will examine the effect of the active mass thickness on the cycle life of low-antimony lead-alloy spine employed in traction deep-cycle. This will

advance the understanding of low-antimony lead-alloy grids in traction lead-acid battery chemistry, structure and cycle life implications under deep-discharge cycling regimes.

4 Materials and methods

This section presents key aspects of the experimental design and methodology to be used to conduct the proposed research.

4.1 Materials

The main material to be evaluated in this research was low-antimony lead-alloy spines ~ 2.0 wt.% Sb with a diameter of ~3.0 mm supplied by PMB. The independent variable studied was the effect of active mass thickness on the cycle life of low-antimony lead-alloy spine employed in deep-cycle batteries. Three different size gauntlets with internal diameter of 6.2 mm, 7.3 mm and 8.6 mm were used in the study. Other materials included lead powder (Pb_3O_4), dilute H_2SO_4 acid 1.170 sp.gr. and flat expanded negative plates. The round gauntlet was constructed from a non-woven polyester tube typical of those used in tubular positive plates in industrial lead-acid batteries. The material is known to provide high mechanical strength, elasticity and long life (Toniazzo 2006). Red lead powder (Pb_3O_4) is normally used to mix with grey leady oxide in positive tubular-plate for stationary and traction lead-acid batteries. Occasionally, 100 % red lead powder is used for fast formation and to achieve initial capacity. Red lead alone as the filling powder can be used in the absence of curing. Flat negative plates were produced at Exide using grey leady oxide. Wet oxide paste mix was applied onto low-calcium lead-alloy expanded grids by the pasting machine and diluted H_2SO_4 acid 1.170 sp. gr. was used for the electrolyte.

4.2 Preparation of the lead spines

The spines used in this study were pressure cast using a HADI die casting machine. They were cast as long spines as shown in Figure 15. The spines were then cut into the required length as illustrated in Figure 16. A spine length of 140 mm (less than half of the normal length) was used for ease of handling and quality consistency: bowing; eccentric within the tube to avoid localized corrosion; and minimize density gradient during oxide filling. A minor modification to the boss (beneath the top bar that enters the top of the gauntlet be inserted into the gauntlet) of the lead spine was made prior to oxide filling. The boss of the spine was designed to fit into the 8.6 mm internal diameter gauntlet tube. The boss had to be filed down for it to inserted firmly into the gauntlets of the smaller sizes: 6.2 mm and 7.3 mm as shown in Figure 17

Figure 15 - Cast spines from HADI die casting machine

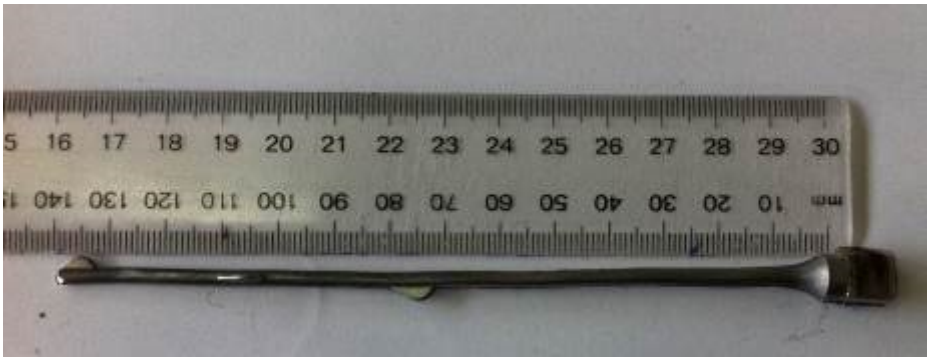

Figure 16 - Spine was cut to the required length from the long cast spines

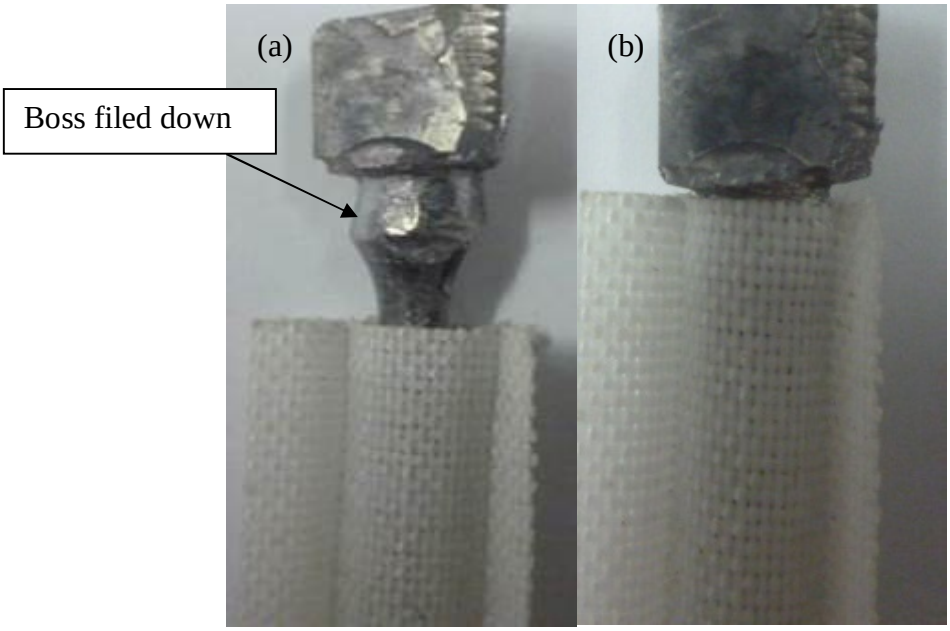

Figure 17 - (a) the boss was filed down to fit the 6.2 mm and 7.3 mm gauntlets. (b) Shows end results where the gauntlet was inserted firmly into the boss.

4.3 Oxide filling and pickling process

The three basic filling methods are in common use: (i) dry power; (ii) pelletized powder and (iii) extruded paste. Of these, dry powder is the most widely used and was adopted for the oxide filling process. The filling process is normally performed with a number of multiple tubes held together on a vibration jig. Unfortunately, this process could not be applied to individual tubes because of the available jig's size. Hence, the red lead powder had to be hand fed into the tubes with a spatula. First, the spine was firmly inserted into the gauntlet as shown above in Figure 16 (b). The gauntlet was then held upside down and red lead powder was carefully fed through the open end. After each gauntlet was filled with a spoonful of red lead powder, it was then given a gentle tap to ensure that the powder is evenly distributed. The tube was filled until the weight was achieved (calculated weigh +/- 0.05g) as shown in Table 1. Once the gauntlet was filled, it was sealed by knocking a plastic cap onto the end of the lead spine. Then a few drops of glue were applied to the bottom end of the gauntlet to hold the cap in place, as shown in Figure 18. Once the tubes had been filled and assembled, they are then "pickled" by soaking in dilute sulfuric acid (H_2SO_4) for approximately thirty seconds. This pickling process converted the lead oxide (PbO) to lead dioxide (PbO_2) and lead sulfate ($PbSO_4$) shown in Figure 19. A curing process was not required since there was no free lead in the red oxide.

Table 1 - Provide design information to build the tubular positive electrode and negative plates

Tubular Design	Gauntlet 6.2 mm Diameter	Gauntlet 7.3 mm Diameter	Gauntlet 8.6 mm Diameter
Gauntlet size (inside diameter - mm)	6.2	7.3	8.6
Paste volume (mm^3)	3388	5041.5	7458
PAM thickness (mm)	1.60	2.15	2.80
PAM weight (g)	9.4	14.0	20.7
Negative paste density (g/cm^3)	4.2	4.2	4.2
Negative plate size (LxHxT) (mm)	3.57x10.6 x 1.2	5.36x10.6x 1.2	7.89x10.6x1.2
NAM Weight (g)	18.8	28.0	41.5
Acid Density (g/ml)	1.170	1.170	1.170
Acid Volume (ml)	170	170	170

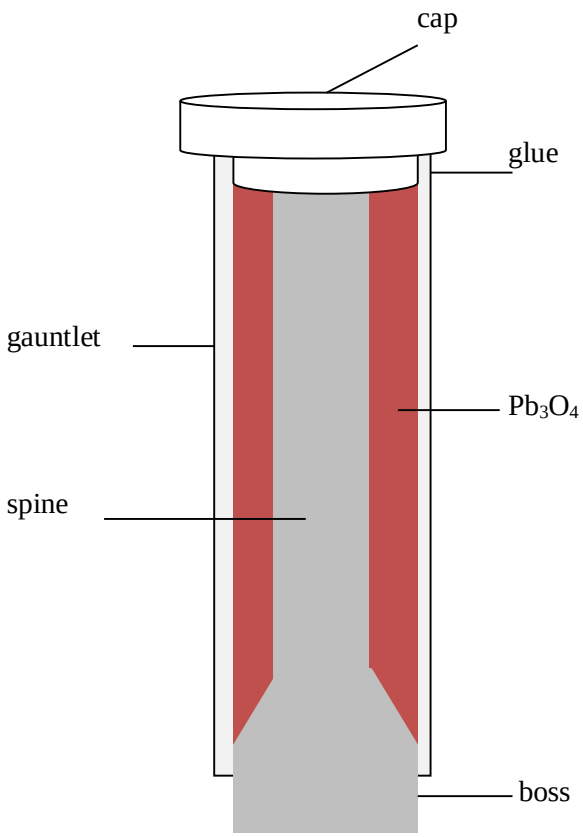

Figure 18 - Illustrates how oxide was fed and held inside the gauntlet by knocking in the cap and applied the glue to hold it together.

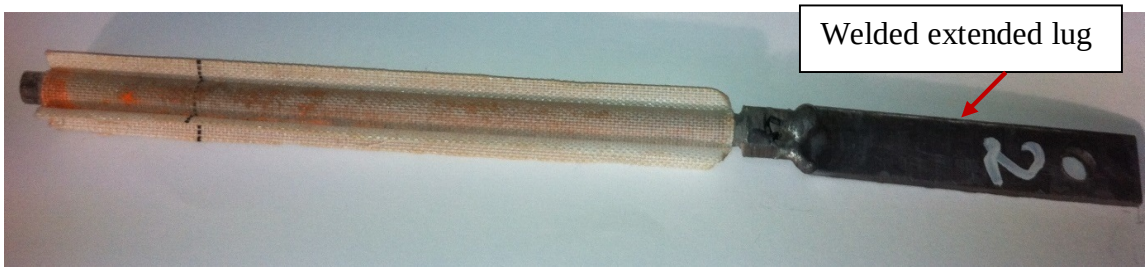

Figure 19 – Example of an assembled single tubular positive electrode with welded extended lug (terminal), was pickled in diluted H_2SO_4 prior to formation.

4.4 Preparation of the PVC block prior to cell assembly

The acid resistance block was fabricated from high density polyethylene vinyl chloride (PVC) material with dimensions HxWxT (135 mm x 154 mm x 30 mm). The block was used for supporting the electrode to freely stand in the upright position and to reduce acid volume. A vertical hole which was 2 mm wider than the electrode was drilled through the centre of the block to allow free acid movement and to form a compression surround for the electrode. Six other 5 mm holes were drilled on the side right though to meet up with the vertical hole as illustrated in Figure 20. This enabled acid to migrate between the positive electrode and the negative plate. The block also used to separate the positive and the negative plate from shorting out.

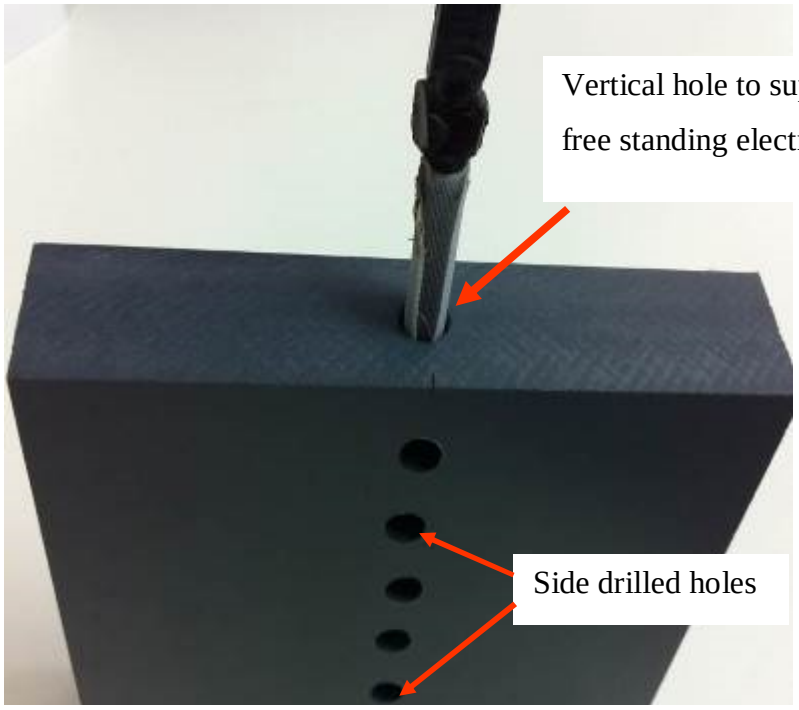

Figure 20 - The PVC block showing vertical drilled hole to support the free standing electrode and side holes to allow acid to move freely between plates.

4.5 Assembling cells for testing

Cells were assembled as illustrated in Figure 21 with a tubular positive electrode and one flat negative plate. First, the PVC block was slotted into a polypropylene container. Next, the electrode was inserted into a vertical hole in the center of the PVC block and then the negative plate was placed in between the PVC block and the container. No separator was used. Finally the container was filled with 170 ml of sulfuric acid with a specific gravity of 1.17. The final assembled cells are shown in Figure 22.

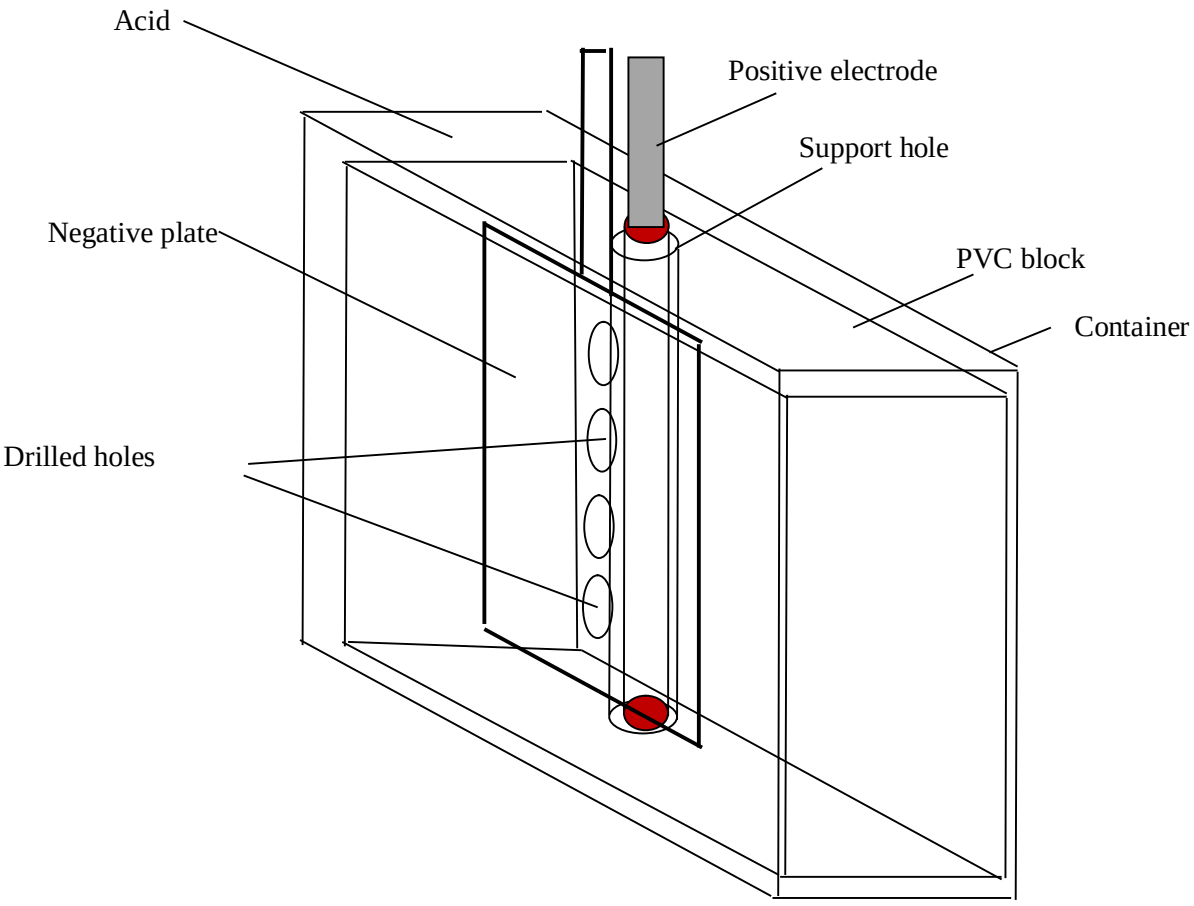

Figure 21 – Illustration of how a single cell was assembled with a tubular positive electrode and one flat negative plate.

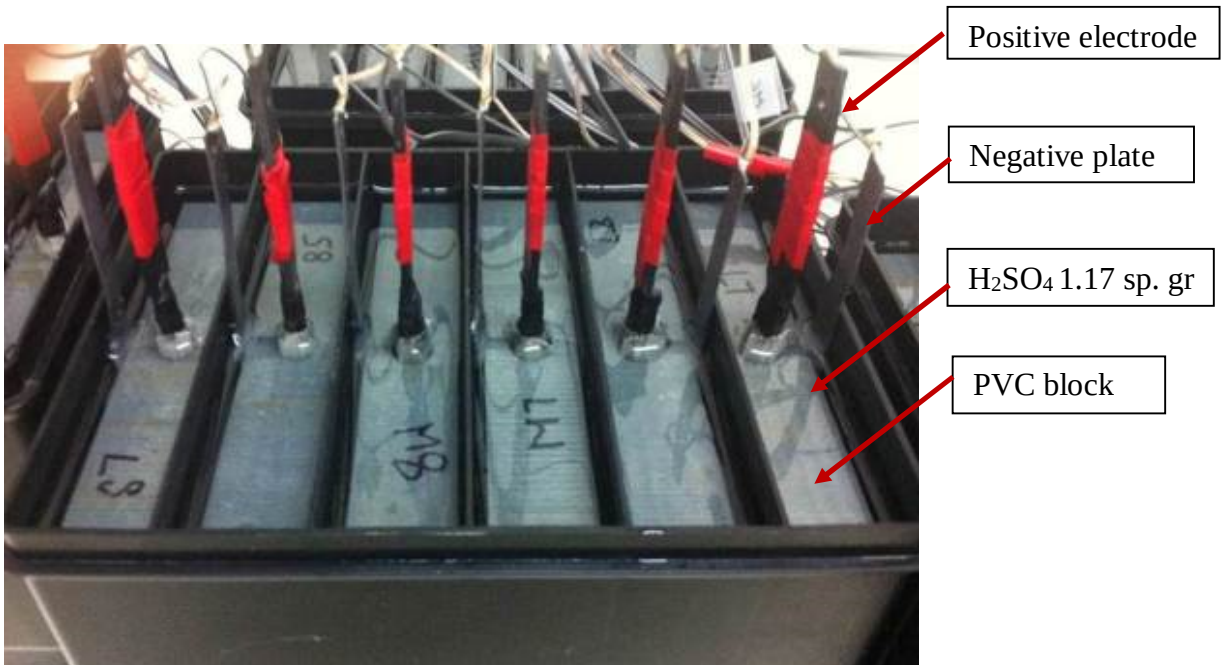

Figure 22 - Six individual cells were assembled in an automotive battery container. Each cell consisted of a tubular electrode and one flat negative plate. PVC block was used to support the electrode and separate the positive and the negative from shorting out.

4.6 Experimental set up

For each set of same size gauntlets, a string of eight cells was connected in series to a charge-discharge unit as illustrated in Figure 23. Individual cell voltage, string voltage and current were wired up to the charge-discharge units and the data logger (DataTaker DT80 series 3) to monitor and log data (see Figure 24). These units were specifically designed and built for this research by Pacific Marine Batteries (PMB).

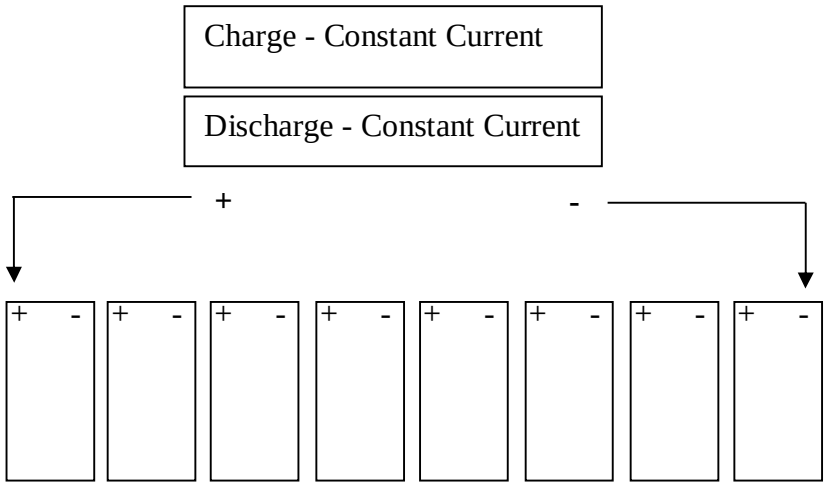

Figure 23 - Schematic of the multiple cells connected in series.to a charge-discharge unit.

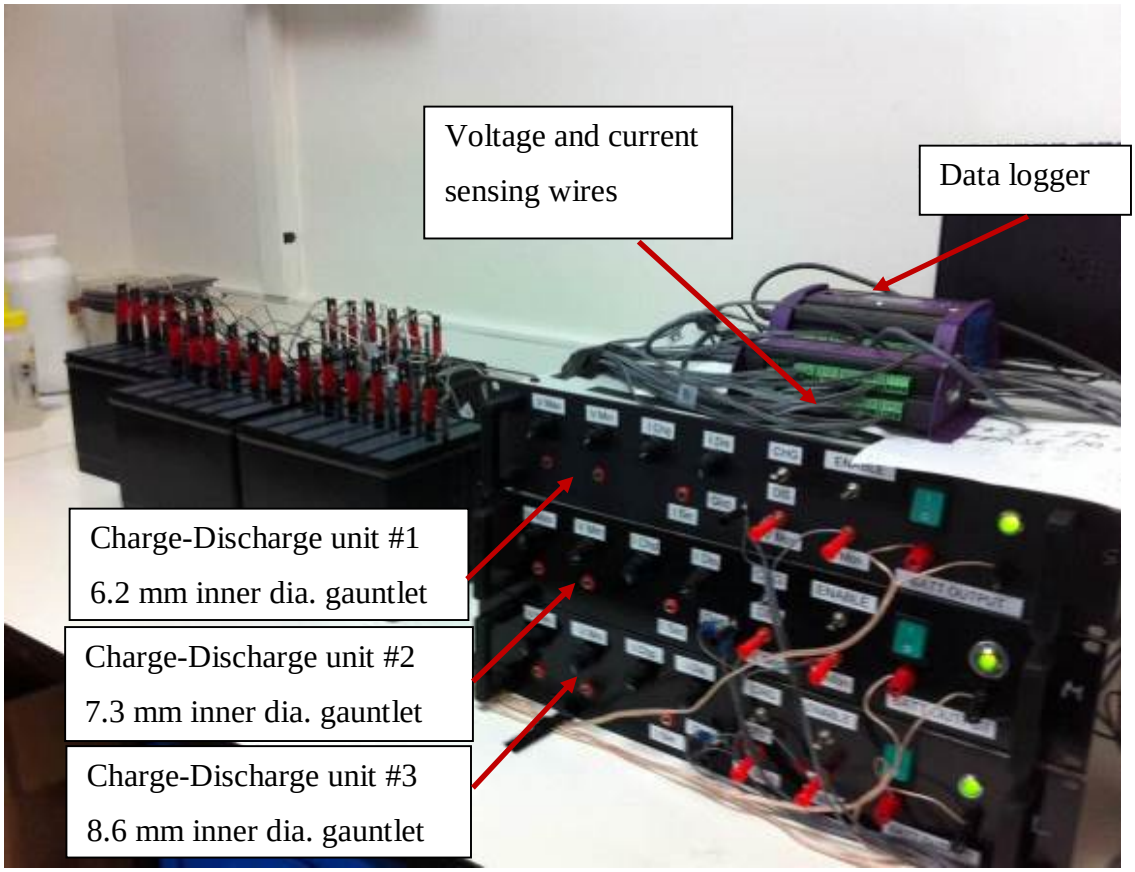

Figure 24 - Cells were wired up to the charge-discharge units and the data logger.

4.6.1 Charge/discharge unit calibration

Calibration of the charge-discharge units was performed to ensure the accuracy of the current and voltage during cycling. Calibration was carried out under various loads to cover the required range of charge/discharge currents. This was checked against a calibrated multi-meter and a 6 volt battery to apply loads on the charge/discharge unit shown in Figure 25.

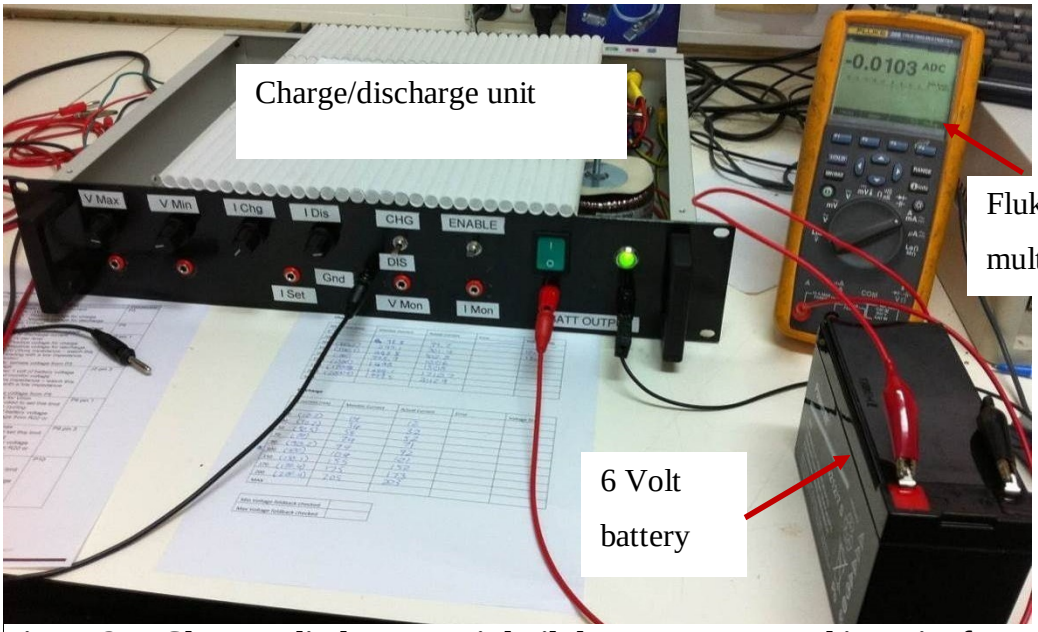

Figure 25 - Charger-discharger unit built by PMB connected in series for calibration

The R^2 value was obtained from the calibration plot (set current against actual current) shown in Figure 26. An R^2 value of 1was obtained for all three charge/discharge units. This indicates that the correlation between the set and actual current was perfect. Error % was also calculated using equation (4-1)

Error % = ((actual current – set current)/set current) x 100 (4-1)

An error % of less than 2% was recorded for all three charge/discharge units. The recorded error % is within acceptable tolerance considering the low operating current. (See Appendix A for calculations)

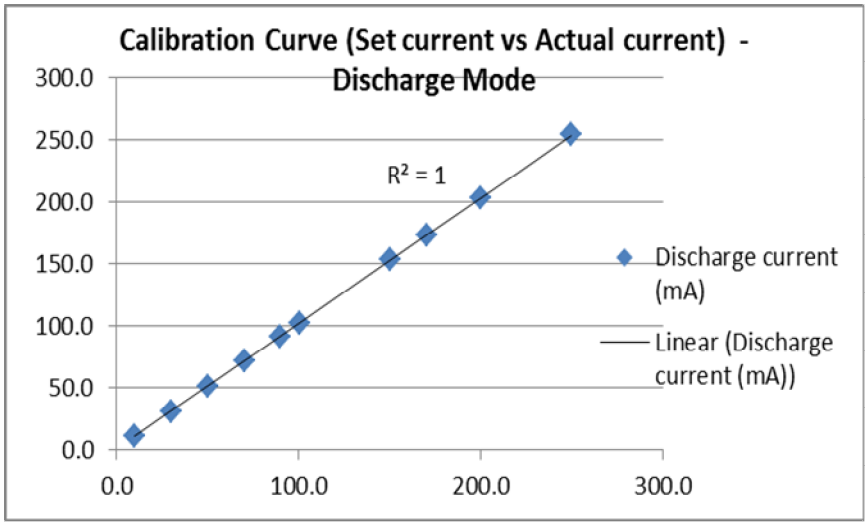

Figure 26 - Calibration plot of set current vs discharge current under discharge mode

4.6.2 Cells formation and cycling test

Formation of cells was carried out in 1.100 sp. gr. sulfuric acid solution at 25°C using constant current factor of 7.92 mA/gram of positive active mass (PAM) for 72 hours. Cells were formed until cell voltages remained constant. Formation acid was replaced with 1.170 sp. gr. acid, and then subjected to a further gas charge at 1mA/gram of PAM until the cell's voltage was stabilized. The cell electrolyte was adjusted to 1.170 sp. gr. and to correct height level before commencing the first discharge.

Cells were subjected to charge/discharge cycles at a constant temperature of 25°C. A completed cycle consisted of a 20 h discharge at constant current 46.6 mA, 70.1 mA and 103.0 mA for 6.2 mm (1.60 mm PAM thickness), 7.3 mm (2.15mm PAM thickness) and 8.6 mm (2.80 mm PAM thickness) internal diameter gauntlets (PAM thickness) respectively, followed by a charge at a constant current and constant voltage with 30% overcharge. A graph of a completed discharge-charge cycle is shown in Figure 27. The

end-of-discharge cut-off was offset at 20 hours rather than cutting-off voltage at 1.58V for the following reasons:

- Constant Ah/kg of positive active mass (PAM) was used to examine the effect of active mass thickness on cycle life under deep-discharge cycling condition.
- Cells were designed with twice the amount of negative active mass (NAM) to PAM by weight ratio and excess acid. Excess NAM and acid were chosen so that during discharge both NAM and acid remained constant while PAM was the study variable.
- Premature capacity loss (PCL) may occur as a result of over discharge if cut-off voltage is set too low.

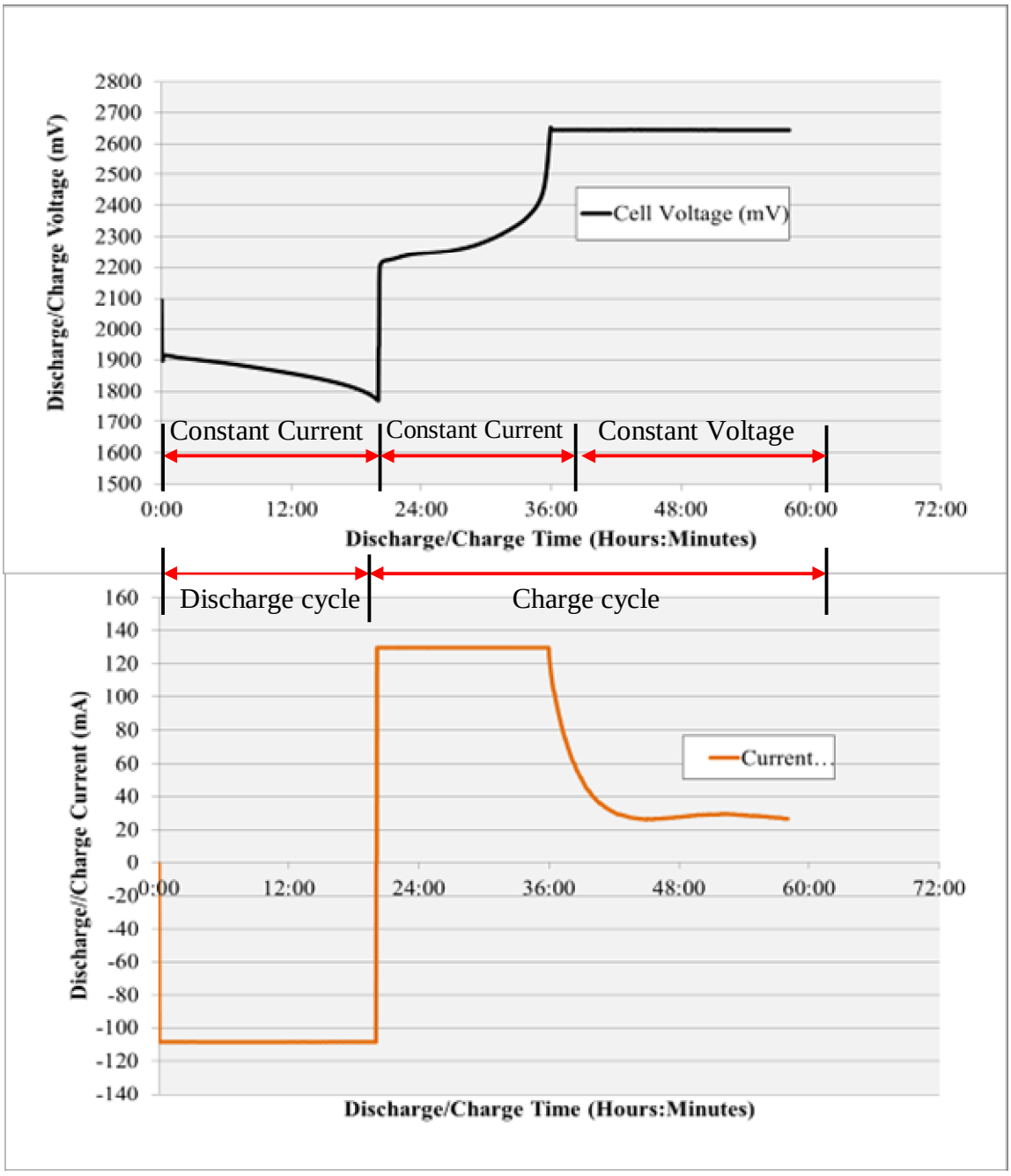

Figure 27 – An example of a typical completed discharge/charge cycle.

4.6.3 Positive active mass (PAM) utilization

For a tubular-plate with an internal diameter of 8.6 mm thick, its real thickness in terms of utilization is the internal diameter (the distance between the outside of the active mass surface and the surface of the spine) which is 2.80 mm. Normally the surface area of the gauntlet is used to calculate PAM utilization. However, under certain conditions where the battery was regularly operated at low rate discharge, then the PAM weight is preferentially used to calculate the utilization. The rate of discharge is dependent on the type of batteries.

According to Bagshaw (1997), a high rate is defined as 1 h, a medium rate is 5-10 h and a low rate is 60-100 h for a traction lead-acid battery operating under a deep-discharge cycling regime. However, for automotive SLI battery, a discharge rate of 5-10 h is considered to be very low. In addition, the utilization of the positive active mass for a traction lead -acid battery is about 35% at the 3-5 h rate. Therefore, a 20 h discharge rate was chosen as a reasonable rate to be used in this study as it is not overly discharge with active mass utilization (approximately 47%). For the purpose of this research, discharge current was scaled down from a typical traction lead-acid battery to obtain the same depth-of-discharge and PAM utilization.

4.6.4 Reference electrode

Plate potentials against a standard reference electrode (Ag/AgCl/sat KCl) were used (Figure 28) to ensure that end of discharge was limited by the amount of PAM. This was confirmed by the steep curve of the positive potential at end-of-discharge as shown in Figure 29.

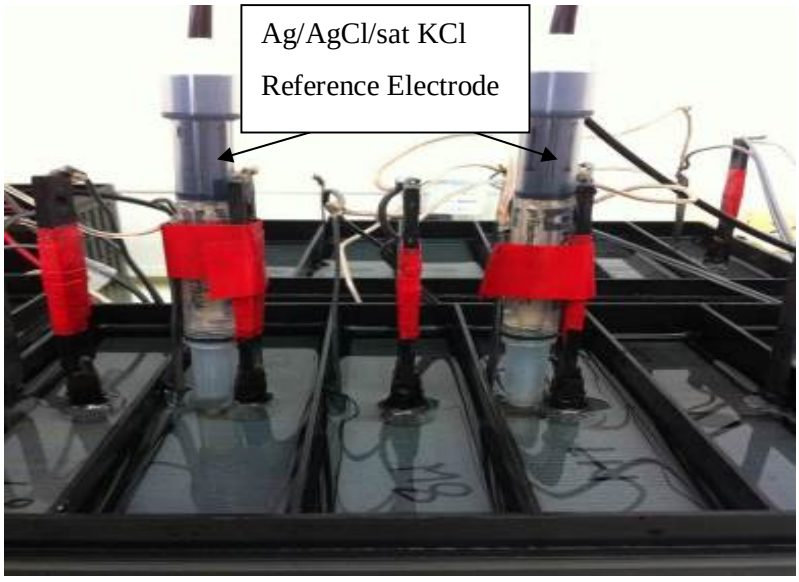

Figure 28 – Standard reference electrode (Ag/AgCl/Sat KCl) to measure positive and negative potentials

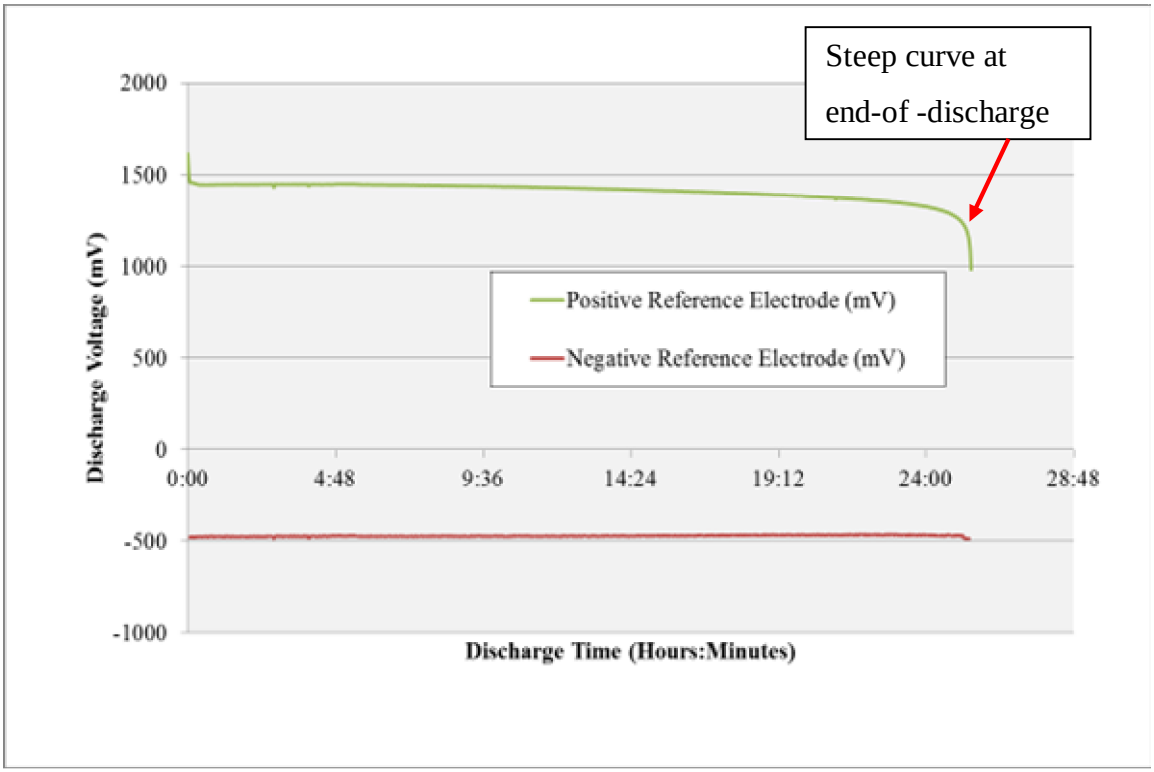

Figure 29 – The limited amount of PAM causes a steep positive potential curve at the end-of-discharge

4.6.5 Recharge

Charging was conducted under constant current (6.96mA/g of PAM) which was maintained until the cell-terminal voltage reached 2.65V. The terminal voltage was held constant at 2.65V. Charging stopped once the overcharge factor (= ratio of input charge to charge removed in previous discharge, or C/D) reached a predetermined value of 1.3. An overcharge factor of 1.2 – 1.3 has been used by many researchers; but, according to the lead -acid industries, a 1.3 overcharge factor is more commonly selected to ensure the cell is fully charged after a deep-discharge.

Overall multiple cells voltage connected in series, current and individual cell voltage were automatically logged at two minute intervals by the data logger during the cycling. The temperature and specific gravity were manually logged before and after each discharge. The cell's capacity was then calculated.

4.6.6 Sample preparation for microscopy

Two sample cells from each test group were terminated after 26, 46 and 72 charge-discharge cycles. Cells were fully charged before the positive electrodes were removed, washed with deionised water until they were largely free of sulfuric acid, then dried for 24 hours at 70^{o}C (Figure 30). Once dried, the thicknesses of the electrodes were measured at three different spots (top, middle and bottom sections) using a micrometer. Samples were then taken to Adelaide Petrographic Laboratories to prepare for microscopy examination.

Figure 30 - Electrodes were dried in the oven after washed

Sample preparation for microscopy involved the mounting of electrodes in epoxy resin. Samples were dissected across the spine as shown in Figure 31. Samples were then mounted in hot epoxy resin and air vacuumed to remove trapped air bubbles. After setting, it is then dissected through the middle as illustrated Figure 32 and polished by abrasion with successively finer grades of carborundum paper. Final polishing was carried out on a lapping wheel with diamond paste of 6, 3 and finally 1 um. End results are shown in Figure 33.

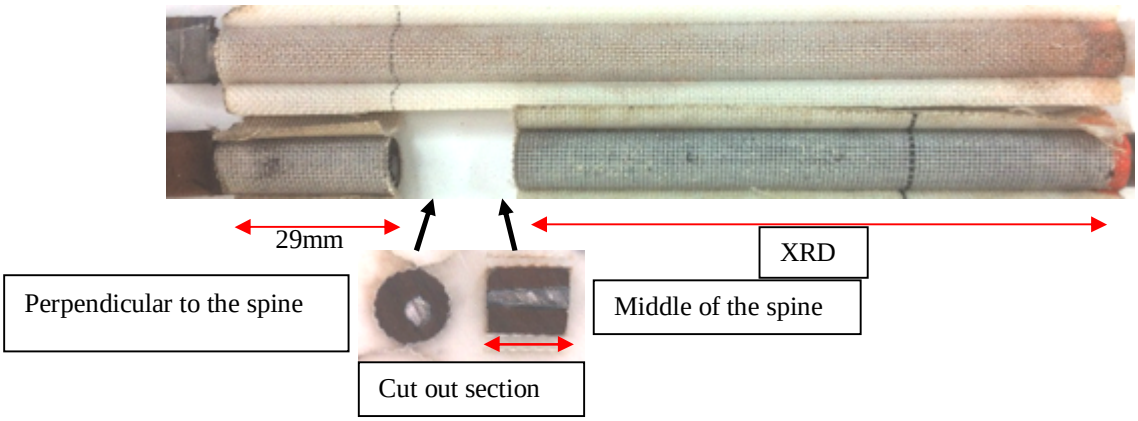

Figure 31- Prepared sections of the electrode for mounting in epoxy resin

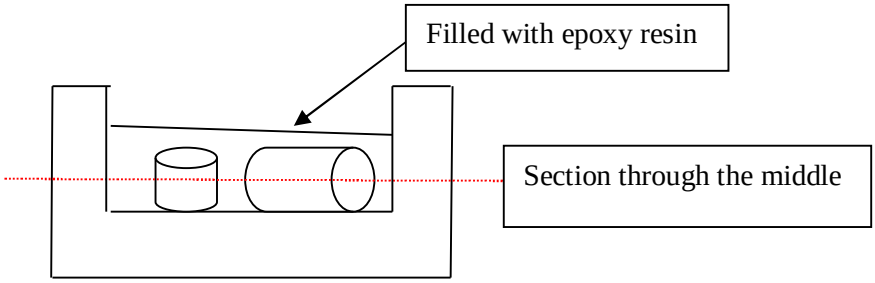

Figure 32 - Drawing to illustrate the mounting of dissected electrode in epoxy resin

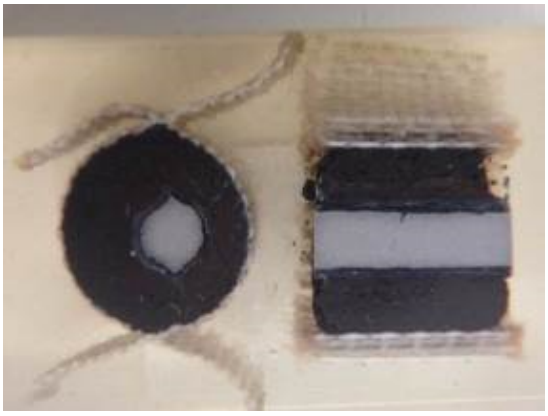

Figure 33 - Sample of mounted sections electrode after final polishing

4.6.7 Scanning electron microscopy (SEM)

Scanning electron microscopy (SEM) was carried out on a Philips XL40 scanning electron microscope. Samples were coated in a thin layer of carbon (~15nm). Imaging with backscattered electron (BSE) was operated at an accelerating voltage of 15 kV spot 6. Images were then montaged for each sample using Microsoft ICE as shown in Figure 34. From these images the following information were examined and obtained:

- corrosion (residual cross-sectional area of a grid/spine);
- corrosion layer area;
- cracks patterns;
- rich layer of lead sulfate.

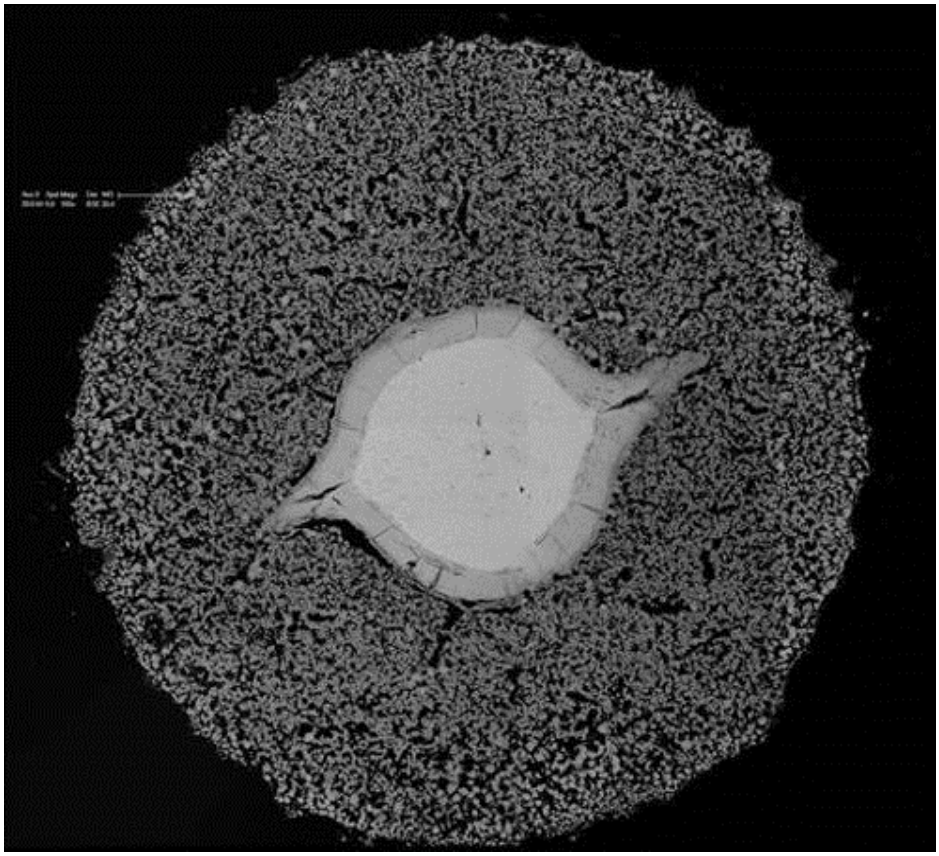

Figure 34 – BSC SEM image of a prepared cross section electrode captured on a Philips XL40 scanning electron microscope at an accelerating voltage of 15 kV

4.6.8 Spot and elements distribution mapping with electron probe micro analysis (EPMA)

Electron probe micro analysis (EPMA) was carried out on a Cameca SXFive electron microprobe (Figure 35). Samples were both analysed via X-ray mapping and spot analysis. The results were compared against Chang and Valeriote (1985) and Barrett et al.'s (1981) findings regarding the use of low-antimony lead-alloy grids in deep-cycle applications as mentioned in Section 3.1. Where Chang and Valeriote found that lead sulfate surrounded the grid due to cracks in the corrosion layer around the grid, Barrett et al. noted that antimony was widely distributed throughout the plate active mass.

4.6.8.1 Spot analysis

Samples were quantitatively analysed using a Cameca SXFive Electron Microprobe running the PeakSite software, and equipped with five wavelength-

dispersive spectroscopy (WDS) X-Ray detectors. Beam conditions were set at an accelerating voltage of 15 kV and 20 nA, utilising a focused beam. Calibration and data reduction was carried out in Probe for EPMA, distributed by Probe Software Inc. Detailed wavelength scans over standards and battery cathodes were carried out prior to analysis in order to choose both peak and background positions that were devoid of any interfering peaks from other elements present in the standards and samples. Calibration was performed on certified metallic standards from Astimex Ltd and P&H Associates. Total acquisition time of five elements on a single point was 132 seconds.

4.6.8.2 Elements distribution mapping

Samples were mapped using the same peak position and calibrated standard intensities as that of spot analysis. The beam condition used for mapping was 15 kV and 100 nA, in which the focused beam was rastered over a set area divided into a specified X by Y pixels. The time taken for one map is governed by the pixel dwell time (measured in milliseconds), multiplied by the amount of pixels in the given area. For this study, five elements (Pb, O, Sb, Sn and S) were mapped over a selected area of 676 x 130 pixels (1350 x 258 μm), with a dwell time of 50 ms, giving a mapping time of approximately 3.5 hours as shown in Figure 37. Historically quantitative mapping is carried out by rastering the beam over the set area with the diffracting crystals on the elemental peak positions, then remapping the same area after offsetting the crystals to a "background" position. This method doubles the acquisition time. The Probe for EPMA software allows fully quantitative pixel by pixel calculation by using the Mean Atomic Number (MAN) background correction (Donovan & Tingle 1996). This negates the need for remapping to acquire the background intensity. The MAN background correction, elemental pixel quantification, and false colourisation are performed in CalcImage, a module of Probe for EPMA.

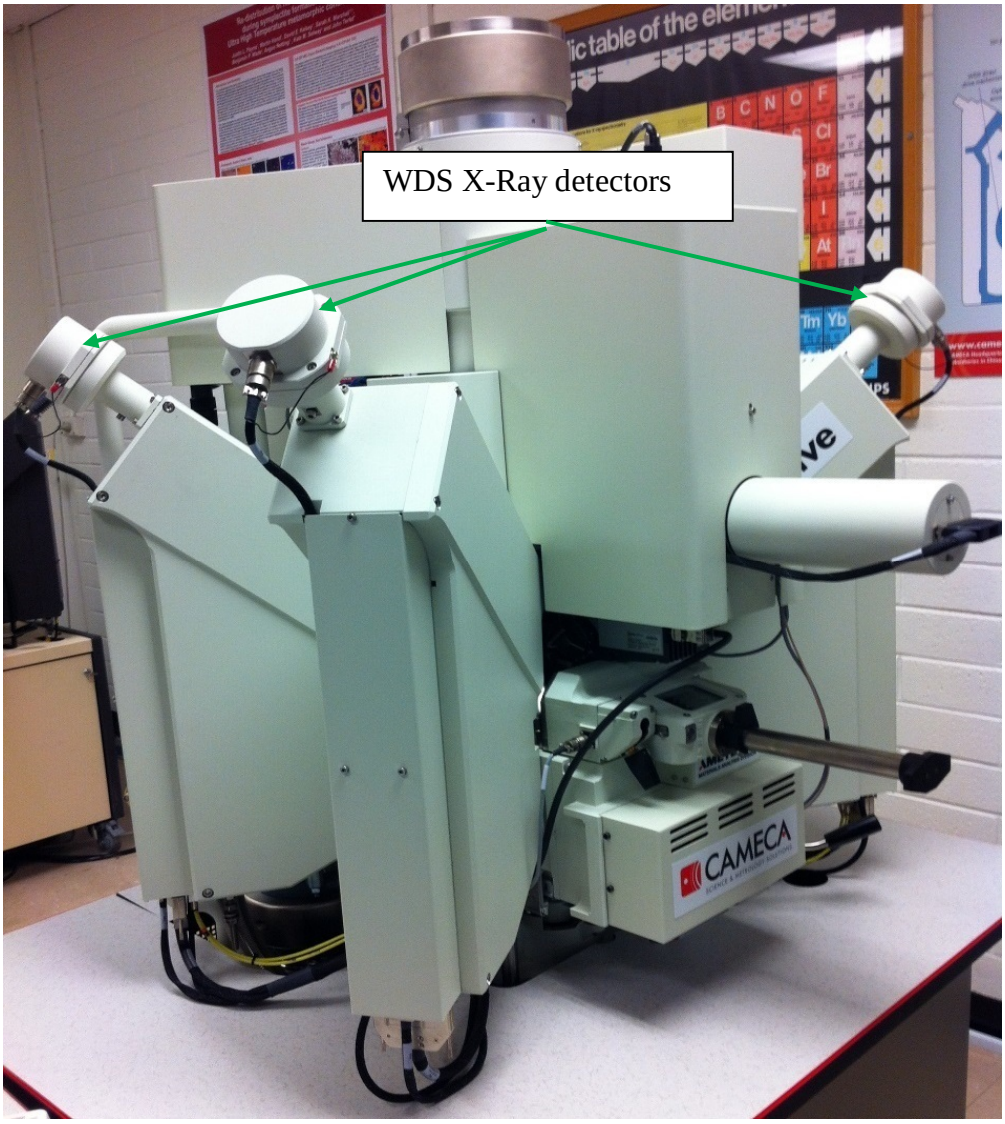

Figure 35 - Cameca SXFive Electron Microprobe equipped with five WDS X-Ray detectors

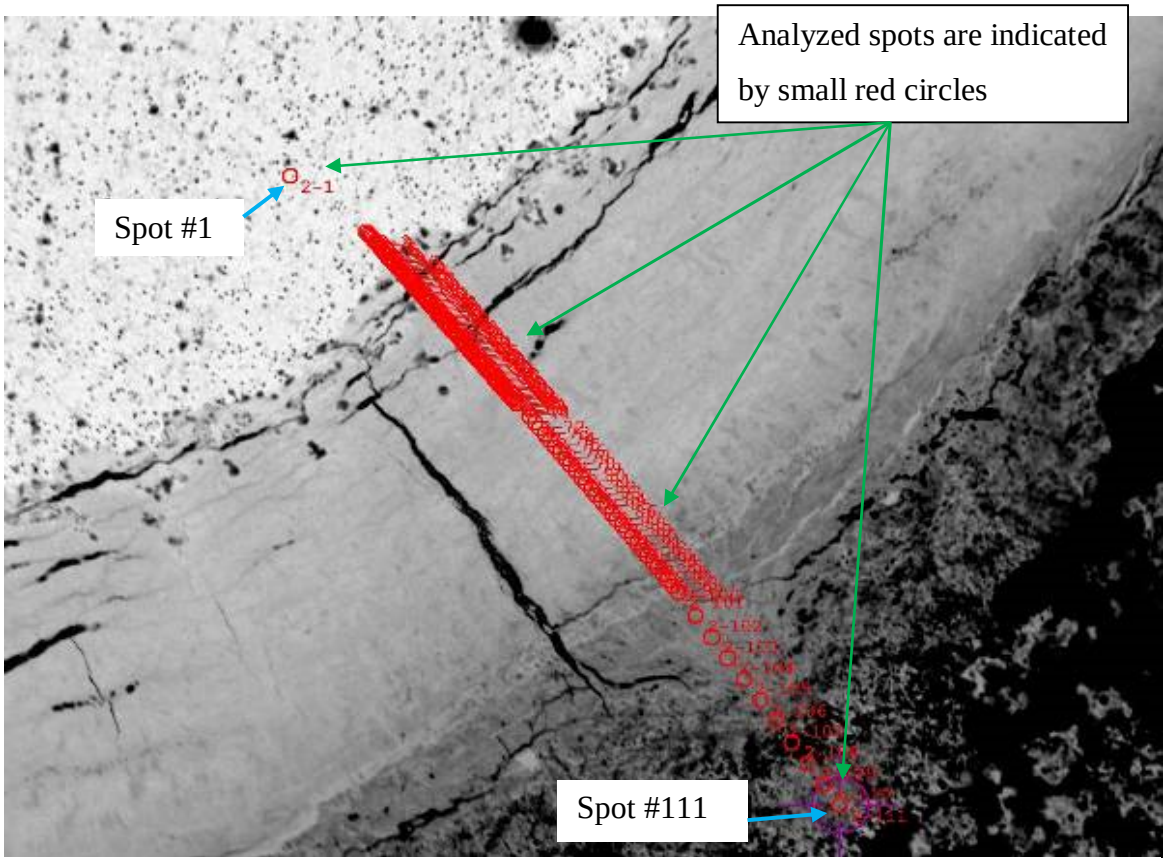

Figure 36 – A numerous of spots were quantitatively analyzed across the corrosion layer for Pb, O, Sb, Sn and S elements using a Cameca SXFive Electron Microprobe

Table 2 – Summarized of element analyzed, peak/background position, count times and standards.

Element/line	Diffracting Crystal	Peak count time (sec)	Background type/fit	Background points (Lo/Hi)	Background count time (Lo/Hi) (sec)	Standard
Pb Mb	LPET	30	Multipoint - linear	4/0	40/0	Astimex Lead
O Ka	PC0	60	Multipoint - exp	2/2	20/20	P&H block - Periclase
S Ka	LPET	30	Multipoint - exp	0/4	0/40	Astimex marcasite
Sn La	LPET	60	Multipoint - exp	1/3	10/30	Astimex tin
Sb La	LPET	70	Multipoint - exp	0/3	0/30	Astimex antimony

Table 3 – Summarized of elemental overlap corrections

Element/line	Diffracting crystal	Overlapping line/order	Overlap standard
Pb Mb	LPET	-	-
O Ka	PC0	Sb La1 VII; Sn Lb1 VII; Pb Mg V	Astimex antimony, Astimex tin, Astimex lead
S Ka	LPET	Sb Lg3 II; Pb Ma2 IV	Astimex antimony, Astimex lead
Sn La	LPET	Pb La2 III	Astimex lead
Sb La	LPET	-	-

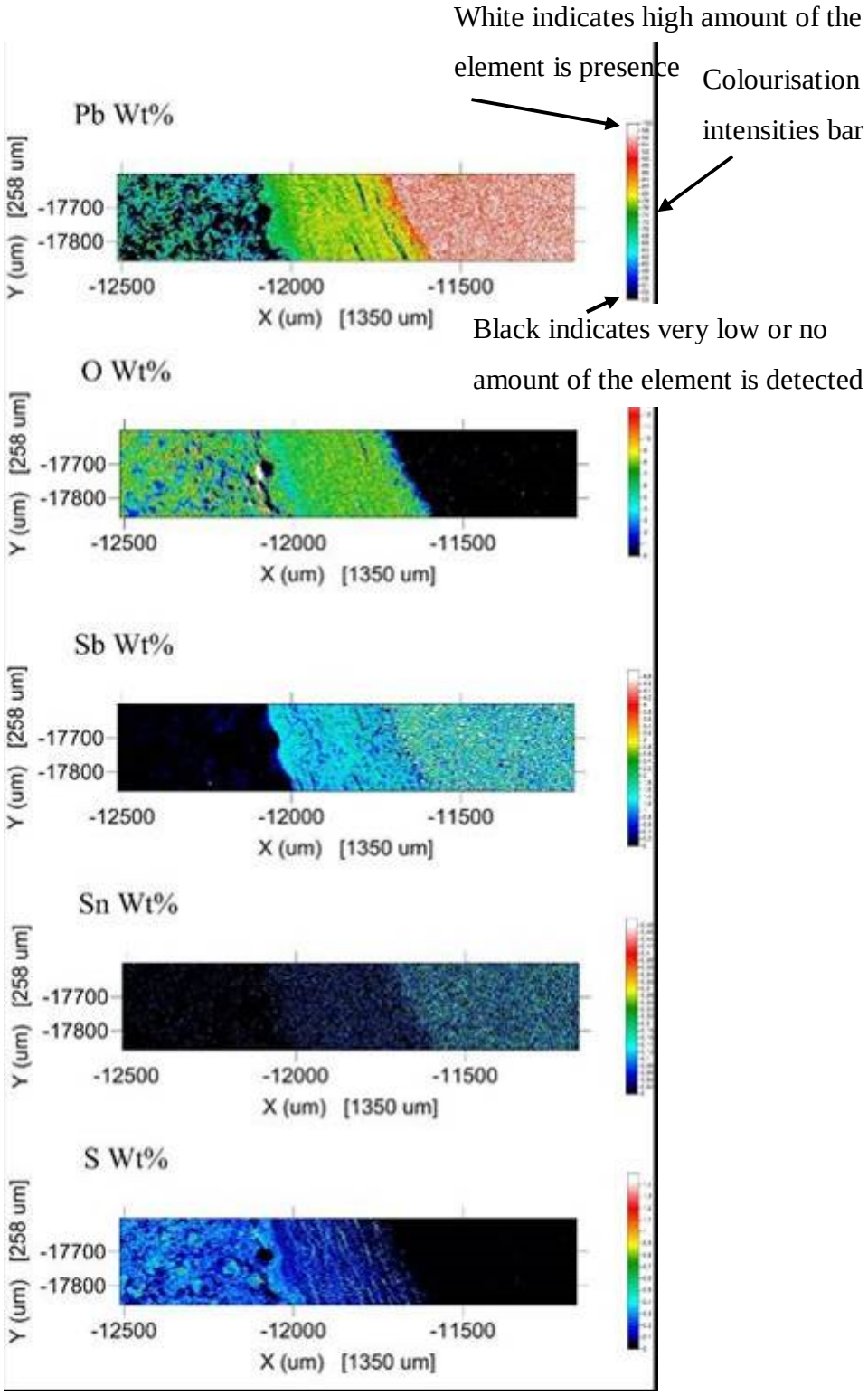

Figure 37 – Elemental distribution mapped part of the selected corrosion layer area showing the colourisation intensities of five different elements analyzed by a Cameca SXFive Electron Microprobe

4.6.9 Measurement of corrosion layer

From the SEM images, the corrosion layer was assessed by measuring the geometric residual cross-sectional area of the spine and the corrosion layer area (Figure 38). Residual cross–sectional area of the spine and the corrosion layer were measured using either ImageJ or iTEM5 image analysis software.

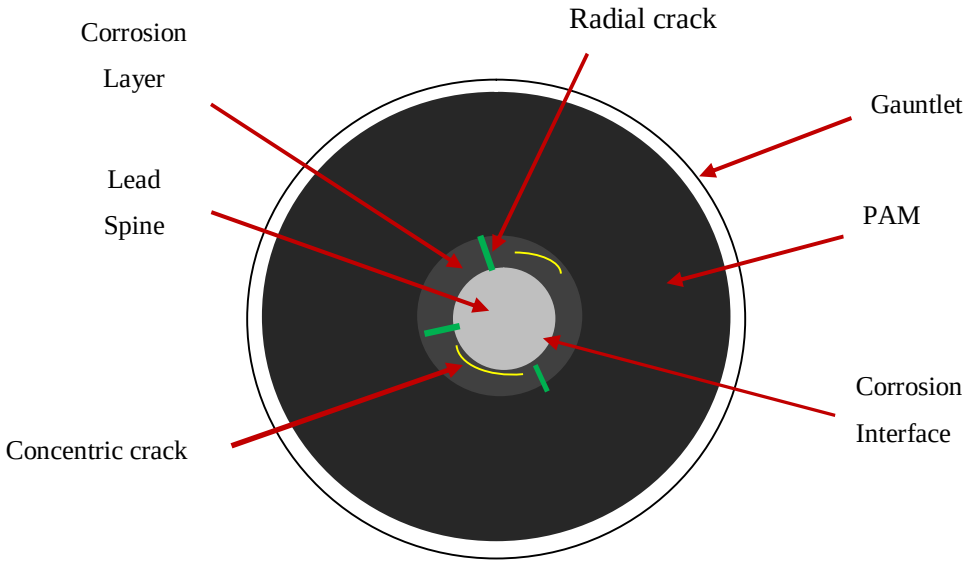

Figure 38 – Illustration of a SEM image showing the cross-sectional area of the corrosion layer, corroded spine and different type of cracks

5 Experimental results and discussions

This section presents the results obtained from the forensic analysis of a decommissioned cell at PMB and the conducted experiment. The results are discussed to provide an understanding implication of low-antimony lead-alloy grids in traction lead-acid battery under deep-discharge cycling and the effect of the active mass thickness upon cycle life.

5.1 A forensic analysis of a decommissioned low-antimony lead-alloy tubular-plate traction lead-acid cell at Pacific Marine Batteries (PMB)

In industry, the corrosion in positive tubular-plates has been observed. Figures 39, 40 and 41 present results of a forensic analysis study at Pacific Marine Batteries (PMB) Pty. Ltd. of a traction LAB cell used for deep-discharge cycling after 5 years of service. Stress appears to be the most likely cause of the damage to the plates. The result shown in this series of photos is typical of damage caused by stress in the positive plates that was also noted by Lander et al. (1958). The following consequences have been observed in the positive plates:

- growth in the length of the spines;
- deformation and bending/buckling of the lead spines;
- swelling of the gauntlet tubes;
- distortion of the bottom support bar – Some shedded active mass that leaked out through the gap between the gauntlet and the bottom bar.

The growth and deformation of the spines indicate that very large stresses have been applied to the spine during deep-discharge cycling. The above observed consequences appear to be as a result of increased in volume, where the lead (Pb) grid is oxidised to lead dioxide (PbO_2). Further forensic analysis of the above plate determined that barely any spine remained (Figure 43) in comparison to a grid prior to service (Figure 42). The service life of the cell was likely limited by grid corrosion caused by stress created by the volume expansion of the corrosion product during deep-discharge cycling.

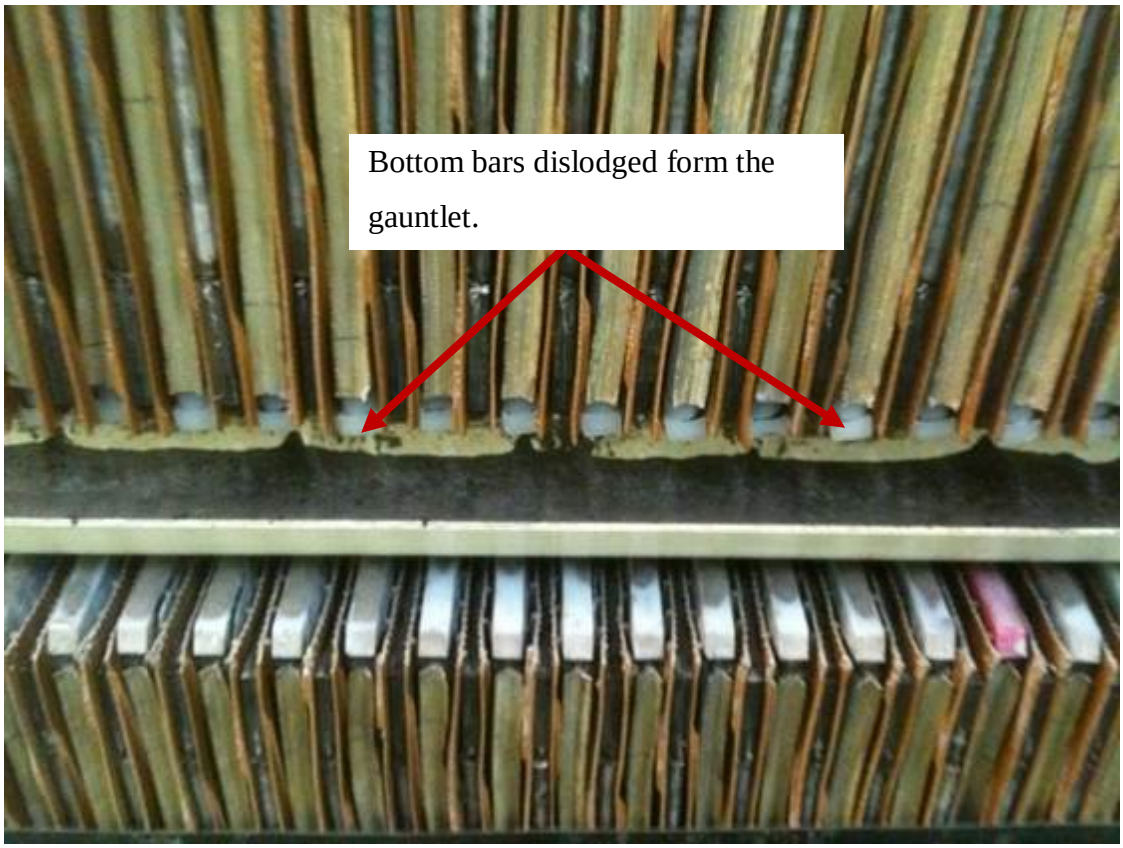

Figure 39 - Photograph of a cell after 5 years in service. The bottom plastic bar that supported the plate and prevented the active mass from falling out has been pushed out from the gauntlet (PMB)

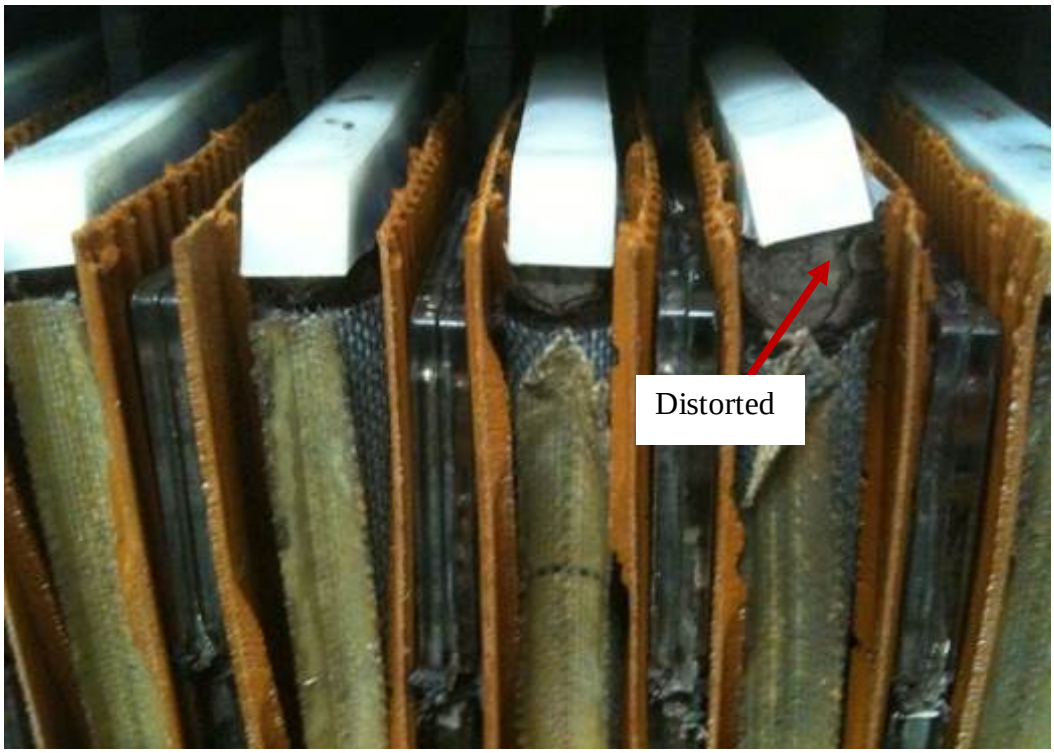

Figure 40 – The identical cell showing the top of the plate has been distorted as a result of expansion of the corroded spines (Courtesy of PMB Pty. Ltd.)

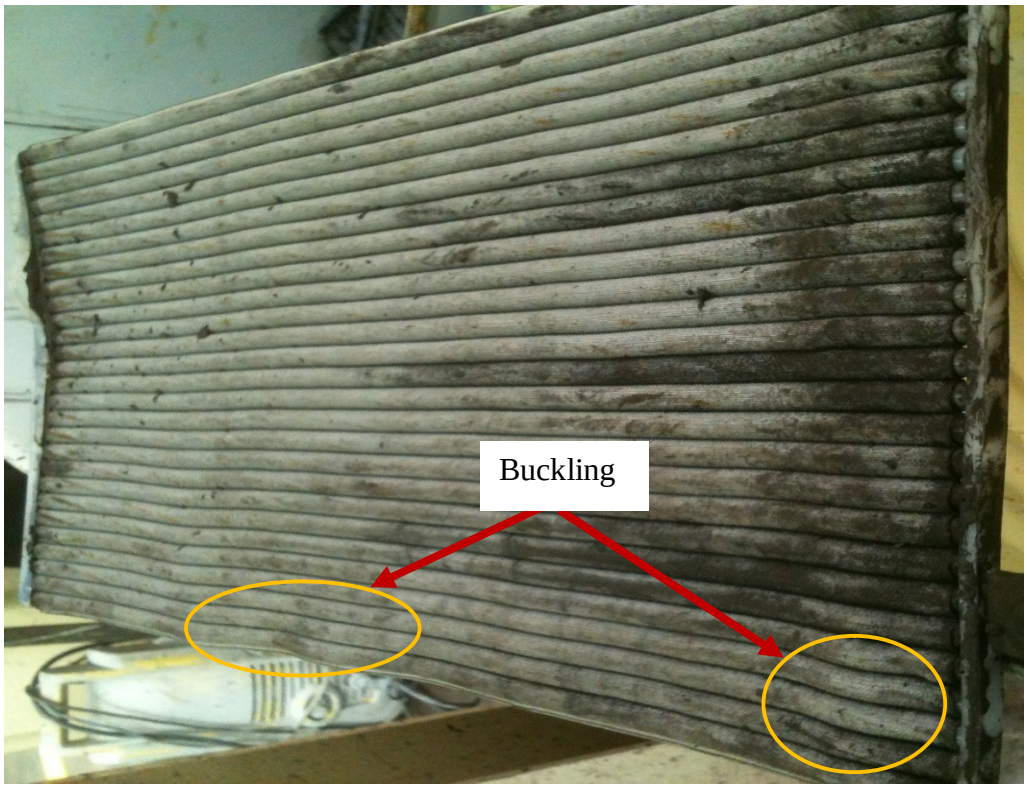

Figure 41 – A plate removed from the cell showing buckling due to stress caused by volume expansion of the corrosion product (Courtesy of PMB Pty. Ltd.)

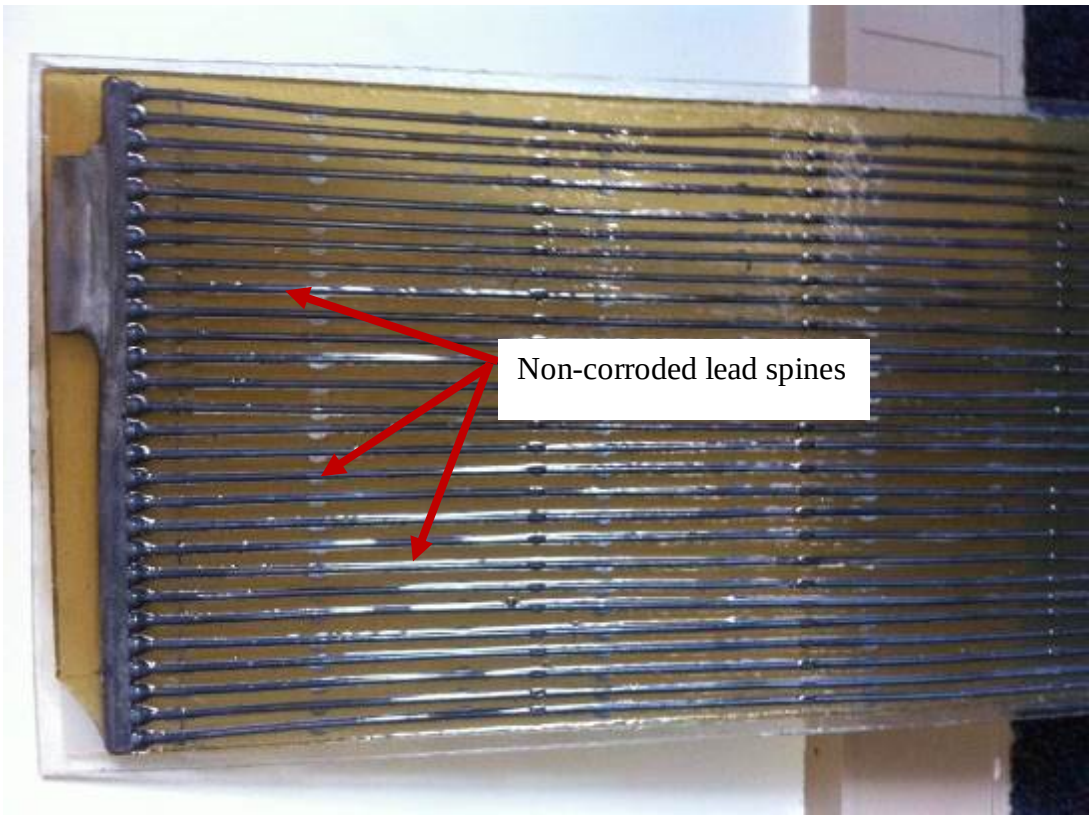

Figure 42 - Photo of lead spines prior to service (Courtesy of PMB Pty. Ltd.)

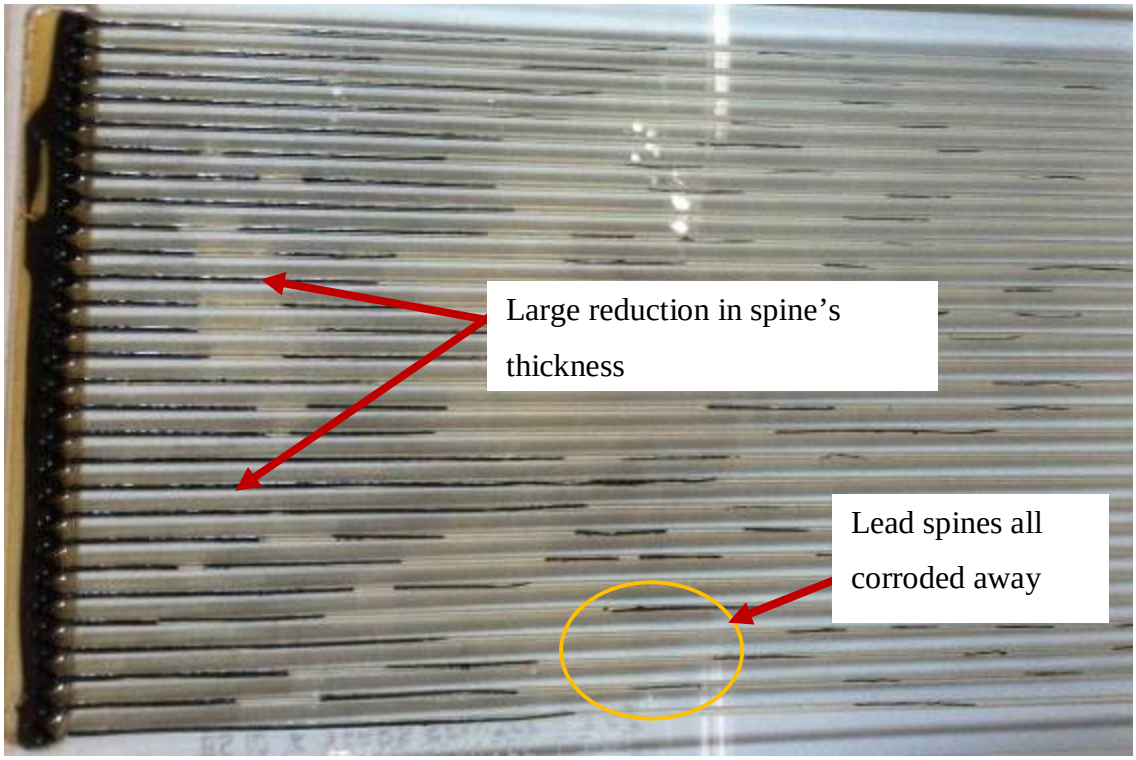

Figure 43 - Photo of corroded lead spines after 5 years of service (Courtesy of PMB)

5.2 The effect of active mass thickness on cycle life of low-antimony lead-alloy spine employed under deep-discharge cycling

This section provides results and critical discussion of the effect of active mass thickness on cycle life of the positive spine employed under a deep-discharge cycling regime. Cell performance and corrosion were examined under capacity test followed by corrosion of the lead spine and rich layer of lead sulfate in the corrosion layer interface.

5.2.1 The effect of active mass thickness on cycle life

A summary of the average cell performance of cycled tubular electrodes under 20 h discharge rates for various active mass thickness of 1.60 mm, 2.15 mm and 2.80 mm is presented in Figure 44. The difference in discharge voltage between different active mass thicknesses was due to discharge current density as outlined in Section 4.6.2. The capacity of the cell is the amount of charge removed from the cell until the cell reaches a practical voltage after 20 h discharge. The plot indicates that the capacity increased with increasing cycle number. This increase in capacity was caused by increased conversion of PbO_2 during cycling (Figure 45) and an increase in β-PbO_2 conversion (Table 4). This phenomenon was also observed by Barrett et al. (1981) as shown in

Figure 46, where the capacity increased and reached its maximum capacity after cycle number 15 and then started to decline during further cycling.

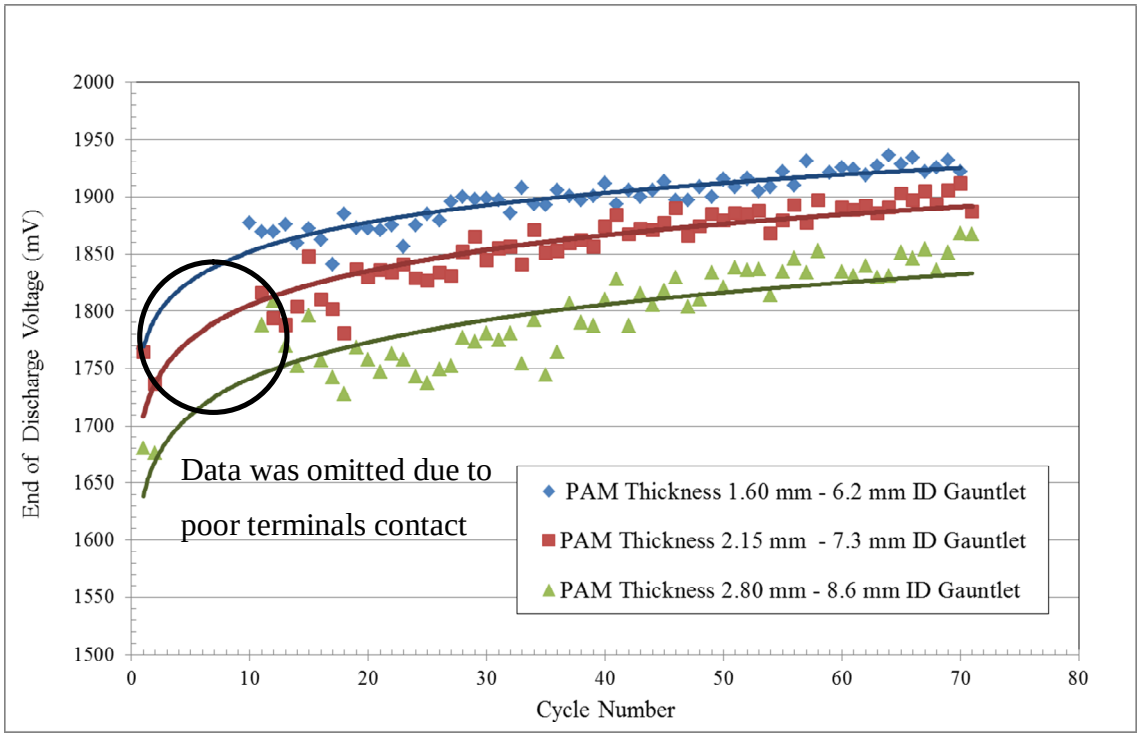

Figure 44 – Capacity test showing end of discharge voltage of the tubular-plate with different active mass thickness

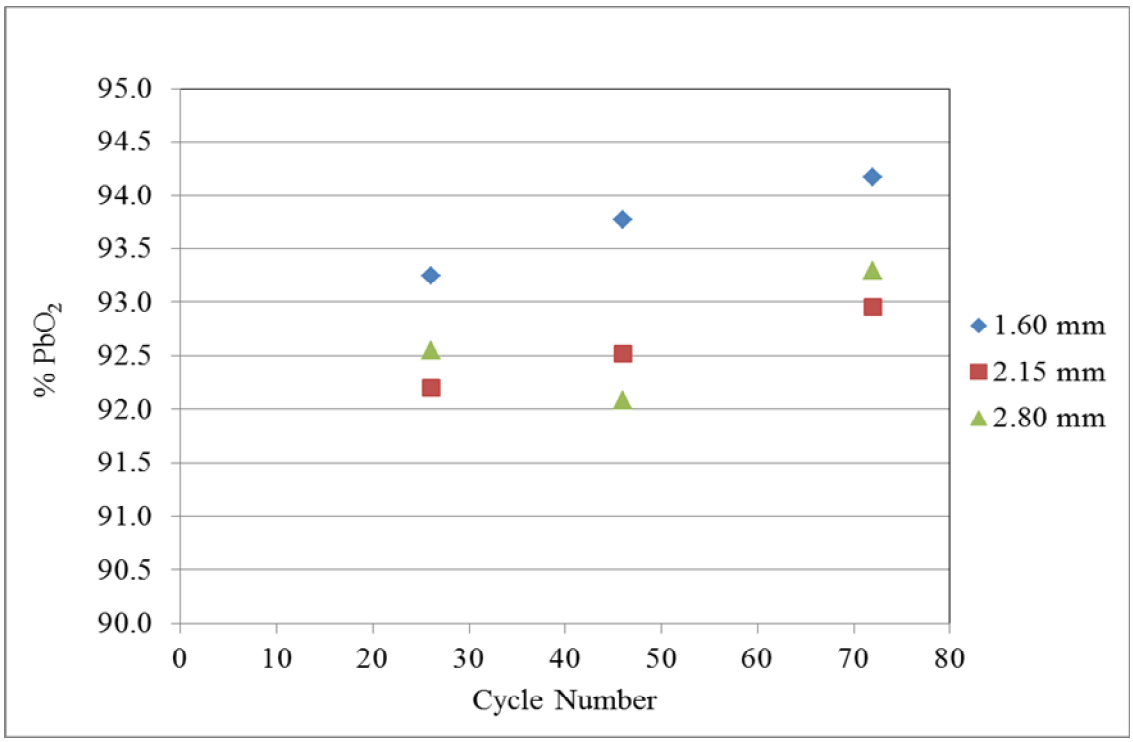

Figure 45 – Increased PbO_2 content with increasing cycle number for various active material thicknesses

Table 4 – XRD result showing increased in β-PbO_2 content during cycling

d = diffraction line	d = 3.49 A	d = 3.12 A		
XRD Result	β-PbO2	α-PbO_2	$PbSO_4$	
Inner Corrosion Layer (ICL)	70.2	22.8	6.9	Cycled with PAM
Outer Corrosion Layer (OCL)	86.2	11.1	2.7	Cycled with PAM
Positive Active Material (PAM)	97.7	1.0	1.4	Cycled with PAM
Positive Active Material (PAM)	87.9	12.1	0.0	Formed, Not Cycled

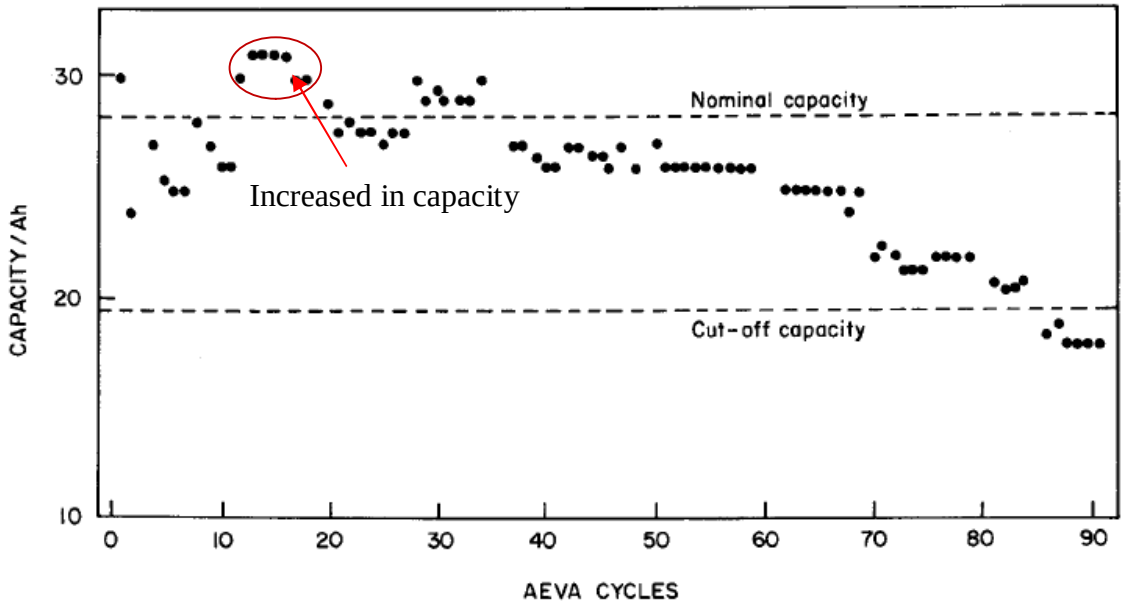

Figure 46 – Capacity of low-antimony lead-acid battery subjected to deep-discharge cycling (Barrett et al. 1981)

Capacity performance tests were terminated after cycle number 72 to allow further examination of the corrosion layer morphology using scanning-electron microscopy (SEM). Long term trend-performance would have been useful to provide a more conclusive outcome but due to limited available resources for maintaining the cycling tests, this was not possible. As recommendation for future research, testing should be conducted using automated charge-discharge cycling units so less time resource is required. Nevertheless, seventy-two cycles should have provided an adequate number of cycles for comparison to literature.

The capacity performance-plot of the tubular-plate for various active mass thicknesses at the end of discharge voltage was still trending upwards after seventy two cycles. This indicates the capacity was still increasing and no sign of rapid reduced capacity was observed in contrast to the work of Barrett et al. (1981); Constantia et al. (1995); Berndt and Nijhawan (1976) and Hollenkamp et al. (1994) in Section 3.1, where the capacity performance declined at a rapid rate after cycle 15 using conventional SLI batteries with low-antimony lead-alloy grids (~2 wt.% Sb) were used for traction duty.

Hence, it may be concluded that tubular-plate with low-antimony lead-alloy spine with various active mass thicknesses of 1.60 mm, 2.15 mm and 2.80 mm have not suffered from rapid capacity loss under a repetitive 20 h discharge cycling regime.

5.2.2 The effect of active mass thickness on spine corrosion

Despite the fact that the capacity was still steadily increasing, corrosion on the lead spine occurred concurrently. Figure 47 illustrates the reduction of the cross-sectional area of the spine after 72 cycles subjected to deep-discharge cycling. The cross-sectional area of the spine was reduced to 47% of the original area. This deep-discharge cycling, approximately 6 months of service, is equivalent to a theoretical 15 year old life for a stationary battery containing similar lead-alloy grid which operated under float charge condition (Battrien, 2002). According to Prout (1994) a thicker lead spine is required for regular deep-discharge cycling due to an increased corrosion rate. Cycle life of a traction lead-acid battery is dependent on the operating conditions, such as deep-discharge cycling, or float charge, due to corrosion.

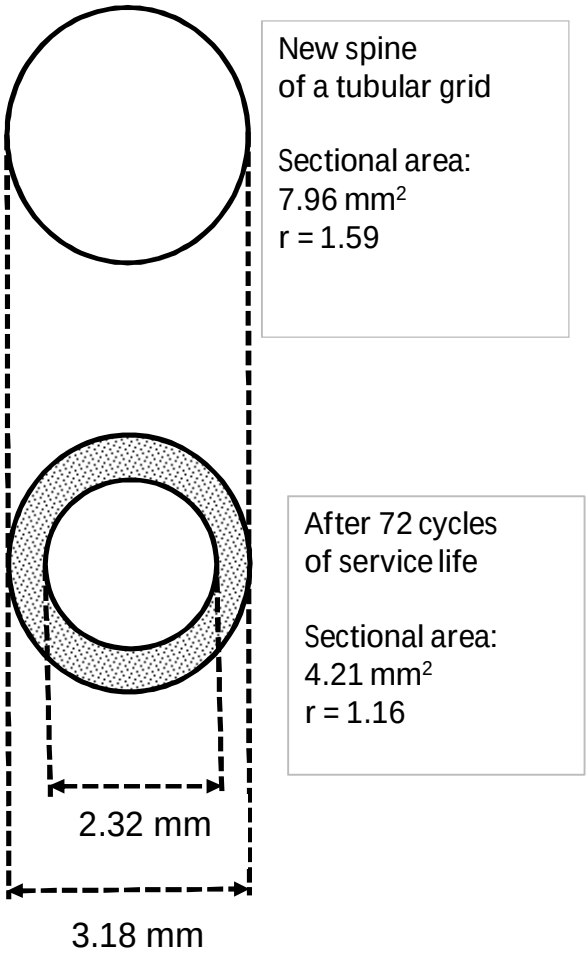

Figure 47 – Measurement of remaining spine radius

In this study, the cross-sections of the charged cycled electrodes at different stages during cycling were measured. The corrosion of the spine was determined by measuring the residual cross-sectional area of the spine as illustrated in Figure 47. The plot's trend (Figure 48) showed that corrosion occurred at a rapid rate upon commencing but this rate reduced with further cycling. The lowest amount of corrosion was observed with an active mass thickness of 2.80 mm. Whereas with active mass thicknesses of 2.15 mm and 1.60 mm, the corrosion difference was insignificance after cycle number 72. A similar inconsistency in results between corrosion and the active mass thickness, especially with active mass thicknesses above 2.0 mm, was also noted in the plot of Rogatchev et al. (1983) (Figure 49). In Rogatchev et al.'s plot, more active mass thicknesses were used, and included the bare spine grid. Therefore, a more definite trend was obtained to indicate that corrosion decreased with increased in active mass thickness. In contrast, bare spine was not included in this study because it was not possible to conduct deep-discharge cycling using a bare spine grid. As outlined in Section 3.3, the corrosion of the spines covered with active mass thickness of 1 mm was half the corrosion of the bare spines, and grid corrosion was only affected by thicknesses up to 3 mm. Hence, without the bare spine as a data point for the plot, it is harder for the relationship of corrosion and active mass thickness to be established. For future research, more various active mass thicknesses between 0 and 3.0 mm are recommended. Some measurements of bare grids (separate to the grids used in the cycling) were added to the plot. The results from the residual cross-sectional areas after cycle number 72 indicated that out of the three active mass thicknesses, the lowest grid corrosion occurred with the 2.80 mm. Again, it could not be established with certainty that corrosion is reduced with increases in active mass thickness due to inconsistent corrosion results obtained from the active mass thicknesses of 1.60 mm and 2.15 mm.

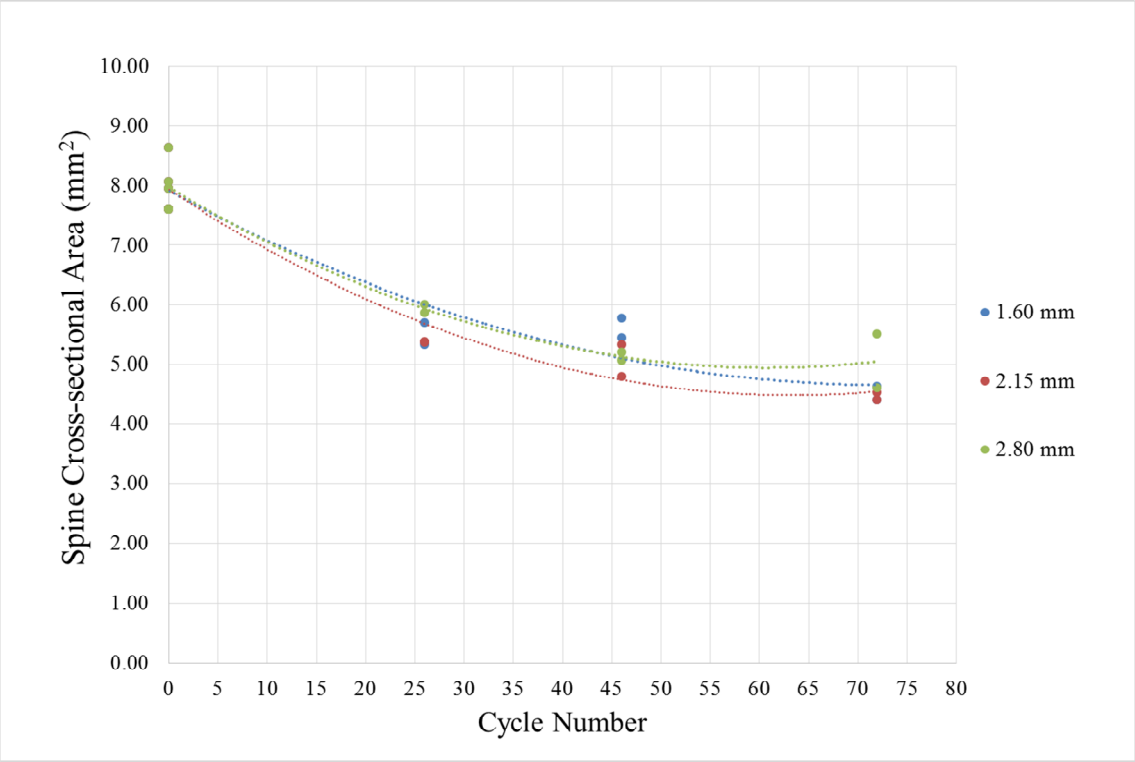

Figure 48 – Reduction in spine cross-sectional area with increasing cycle number for various active material thicknesses

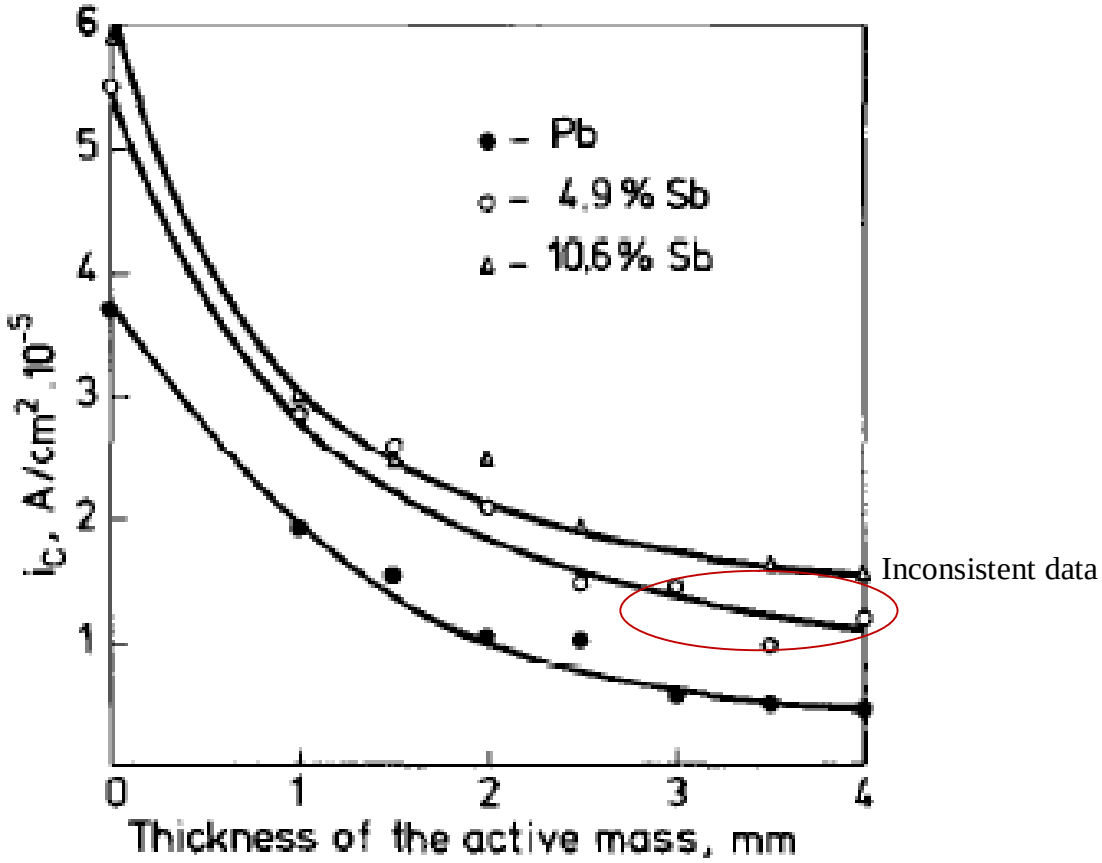

Figure 49 – The relationship between corrosion rate and the active mass thickness (Rogatchev et al. 1983)

5.2.2.1 Corrosion measurement

This section describes of how the cross-sectional area (A) of the spine was calculated using image analysis software such as ImageJ or Olympus iTEM5 as outlined in Section 3.4.

Examples of the cross-sectional area in SEM images are presented in Figure 50 of an un-cycled spine and in Figure 51 of a cycled spine. The scale bar on the SEM image was used as a set scale that enabled ImageJ to calculate the cross-sectional area of the spine. Using formula (5-1) the radius of the spine r can be calculated:

$$r = \sqrt{A/\pi} \qquad (5\text{-}1)$$

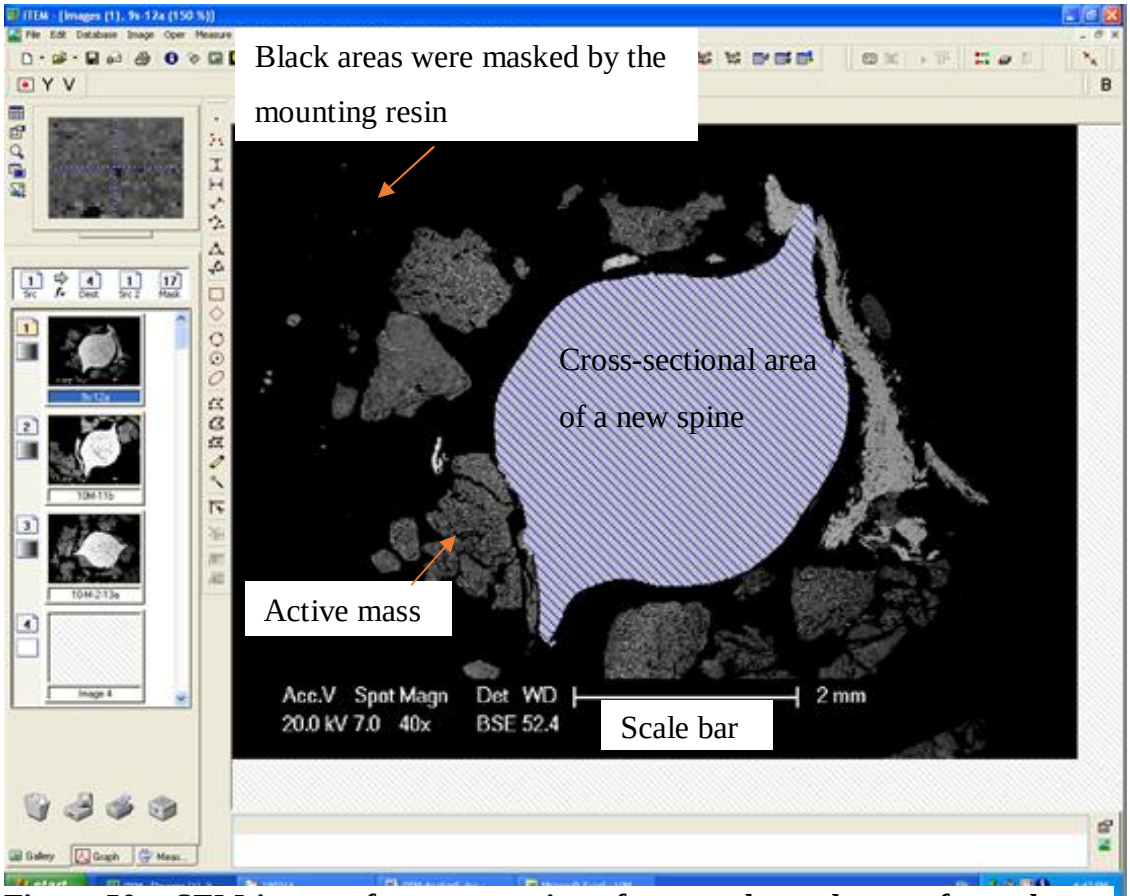

Figure 50 – SEM image of a cross section of a new electrode at unformed state with 40x magnification

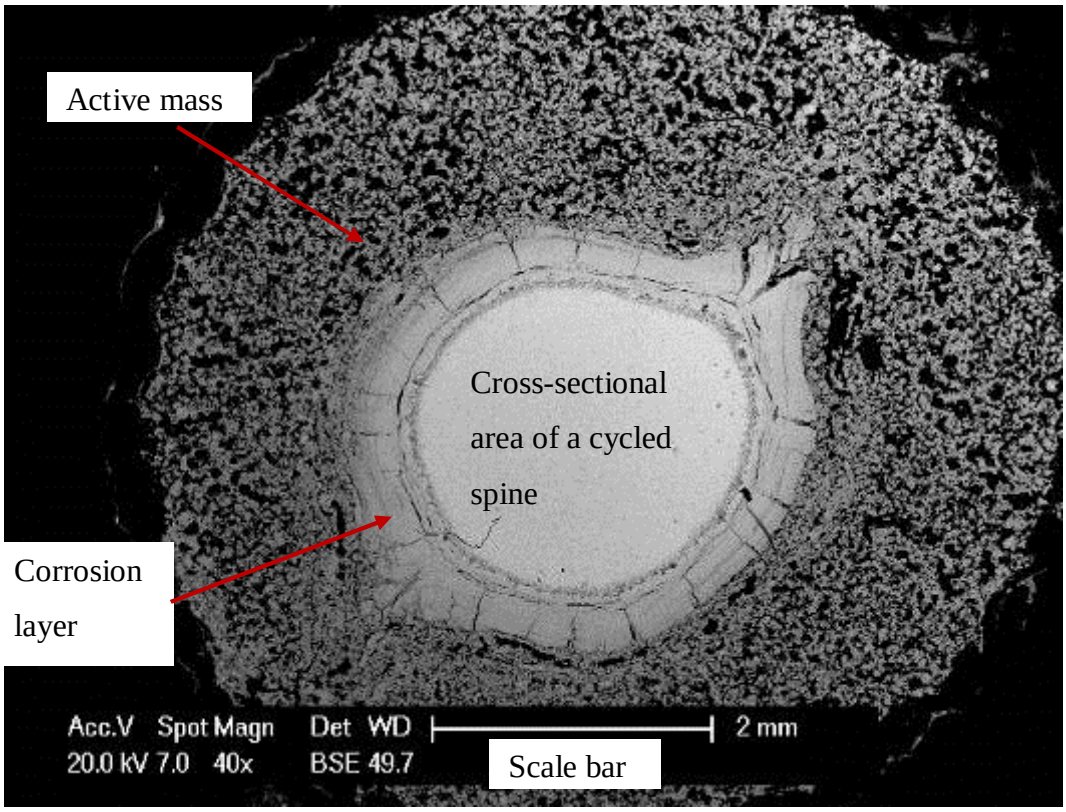

Figure 51 - SEM image of a cross section of a cycled electrode after 72 cycles at 40x magnification

5.2.3 Lead sufate layer in the corrosion layer interface

Back-scattered electron imaging, quantitative electron microprobe spot analysis and X-ray mapping were conducted on a Cameca SXFive to investigate the elemental distribution of lead (Pb), oxygen (O), sulfur (S present as sulfate) and antimony (Sb) in the corrosion layer. Examination of the back-scattered electron images of the corrosion layers as shown in Figure 52 (cycle number 72), found that the corrosion layers were thick, dense and homogeneous. However, under very close examination of the back-scattered electron images it was found that the corrosion layer consists of two sub-layers (Figure 53). Back-scattered images suggested that the inner corrosion layer was slightly lighter than that of the outer corrosion layer areas but was darker in comparison to the lead spine. Variations in intensity and contrast of back-scattered electron are dependent on atomic number. The lighter regions correspond to higher average atomic mass areas and likely to be metallic lead, while darker regions are due to lower atomic mass areas and are likely to be PbO_x and the black areas denote the mounting resin with the lowest average atomic mass.

Further examination of the back-scattered electron image (Figure 52) in conjunction with the quantitative spot analysis (Figure 55) found that an inner corrosion layer

existed adjacent to the metal and the outer corrosion layer. Almost identical composition of lead and oxygen were discovered in the inner and outer corrosion layers. Because of the similar composition with similar average atomic mass number, hence the layers appear to have a similar contrast and intensity. As a result of this, the internal boundary between the corrosion layers was not clearly delineated using the back-scattered electron images.

The inner corrosion layer was considerably thinner than the outer corrosion and its thickness was not uniform. The inconsistency of the depth of corrosion may be a consequence of corrosion at the metal grain boundaries. Furthermore, cracks seem to occur primarily in the outer corrosion layer. These were seen to run parallel and perpendicular to the spine. These cracks were reasonably large and could act as development sites to promote further corrosion. Formation of large cracks may be the consequence of low-antimony presence in the corrosion layers. Nevertheless, back-scattered electron images did not reveal any rich layers of lead sulfate in the corrosion layers as shown in Figure 54. Such layer were discovered by Barrett et al. (1981) and Chang and Valeriote (1985) and occurred in convention start-lighting-ignition (SLI) batteries containing low-antimony lead-alloy grids under deep-discharge cycling application as outlined in Section 3.1.

The quantitative spot analysis of the lead and oxygen plot (Figure 55) indicates a decreasing trend in the lead content with further distance away from the spine. High average lead content (about 95 wt.%) was seen in the lead spine areas, although the readings fluctuated. These fluctuations may be due the pitting variations and surface roughness shown in Figure 52 indicated by black dark spots. In comparison to the inner corrosion layer, a drop of roughly10 wt.% Pb was noted and a further 5 wt.% was observed in the outer corrosion layer. An inverse trend was noted for oxygen. No oxygen found in the metal areas as expected and an increase in the oxygen content observed in the inner corrosion layer.

The quantitative spot analysis of the antimony and sulfur plot (Figure 56 – is Figure 55 with x scale changed to 0 – 20 wt.%) indicates antimony in the metal varied within a range of 1 – 6 wt.% with an average concentration of 3 wt.%. These fluctuations may be due the pitting and variations in surface roughness. The antimony in the corrosion layer and the active mas was also fluctuated ranging from 0 – 2 wt.% with an average

concentration of roughly 1 wt.%. No sulfur was found in the corrosion layer and trace amount were roughly 0.1 wt.% in the active mass.

Results from the X-ray mapping analysis for sulfur (S) and antimony (Sb) presented in Figure 57 also confirmed that there was no rich layer of lead sulfate present in the corrosion layer. Furthermore, the antimony concentration was higher in the spine than in the corrosion layer and only small traces of antimony was present in the active mass at various spots. If the corrosion layer had a much lower antimony level compared to the spine this means the antimony has migrated elsewhere. It is not in the active mass because the antimony level is low; it is likely that the antimony had dissolved and some migrated to the negative plate (Bagshaw 1991).

In contrast, antimony was found to be widely distributed in the active mass throughout the plate material by Barrett et al. (1981) but he has questioned if the presence or absence of sulfate had any influence on the presence of antimony. By contrast, Lander et al. (1958) observed that low-antimony levels may lead to cracking in the corrosion layer as a consequence of stress. Clearly, acid may diffuse into these cracks and form a lead sulfate barrier. In the results of Figure 56, there is a low antimony level present in the corrosion layer. There are also cracks in the corrosion layer for any sulfuric acid to migrate to the grid and the corrosion layer interface. However, no sulfur was detected in this interface, therefore, no sulfate barrier was formed. This does not support either the work of Barrett et al. (1981) or Lander et al. (1958).

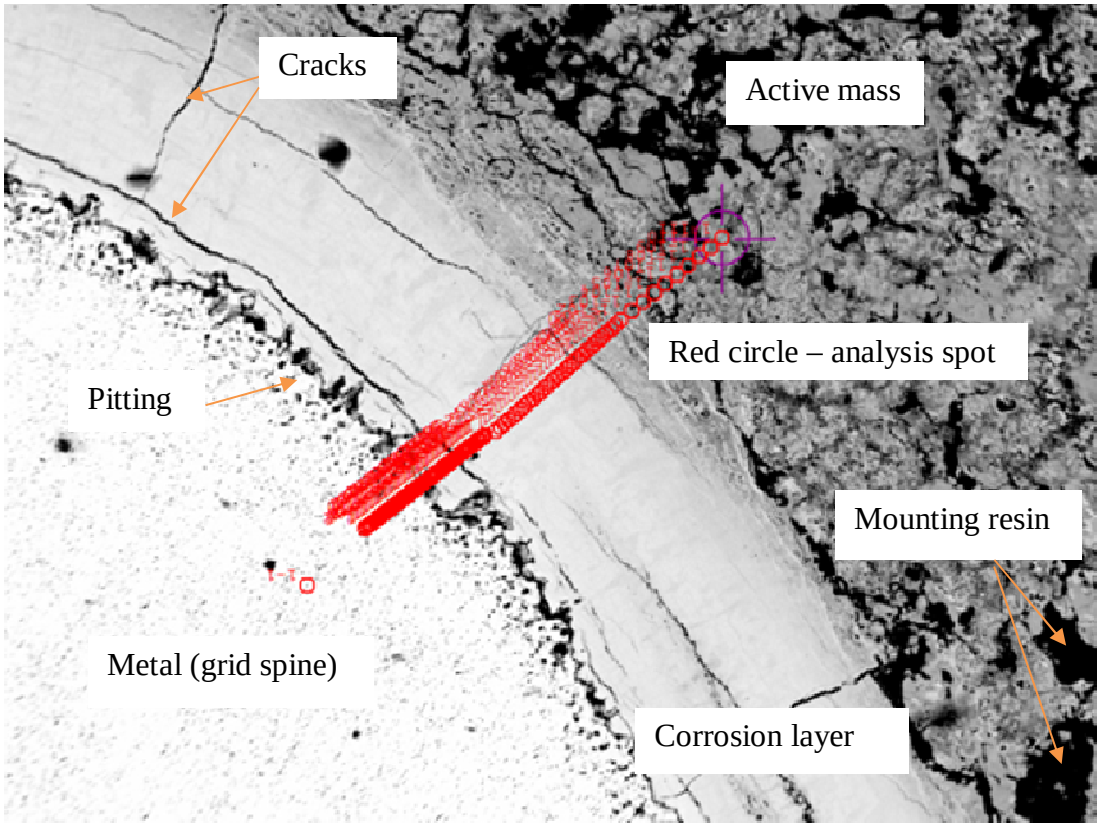

Figure 52 - SEM of cross section of a cycled electrode at cycle number 72 showing the quantitative electron probe analysis positions

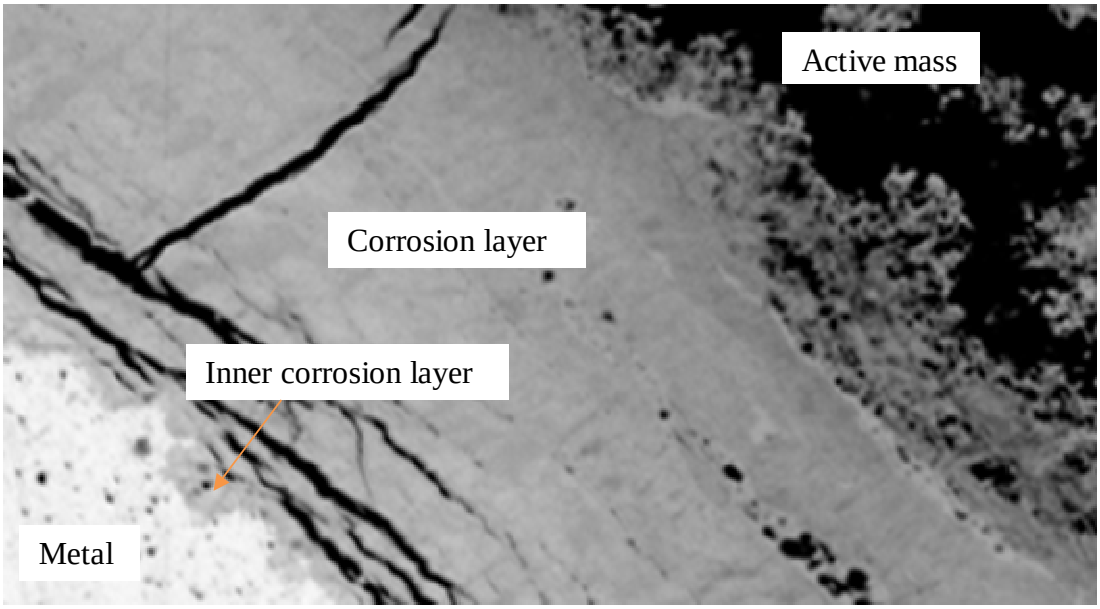

Figure 53 - SEM of cross section of cycled electrode at cycle number 72 showing the inner corrosion layer

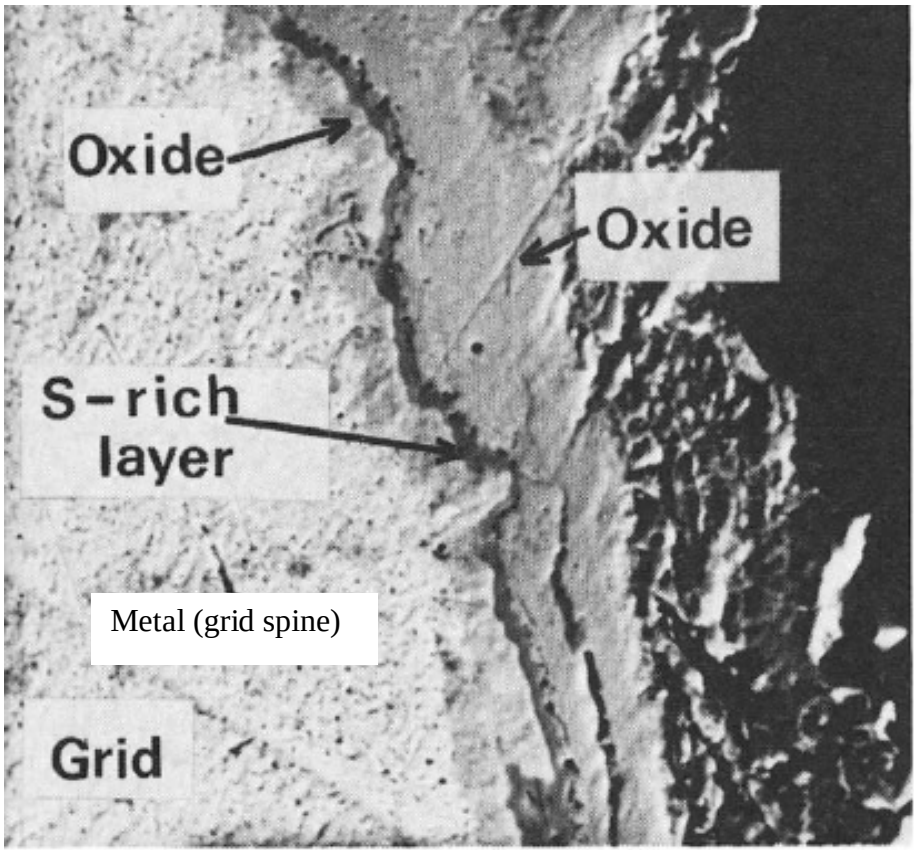

Figure 54 – Electron micrograph of a positive plate showing sulfate rich layer (Barrett et al. 1981)

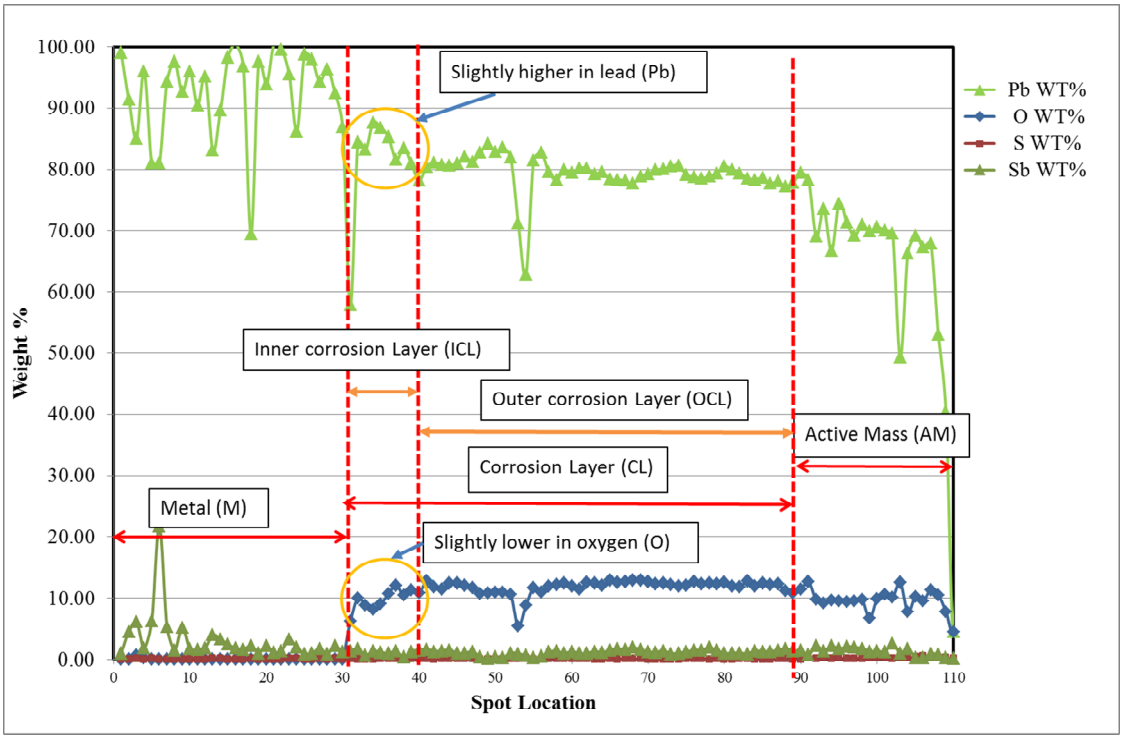

Figure 55 – Quantitative spot analysis of the lead (Pb), oxygen (O), antimony (Sb) and sulfur (S) composition

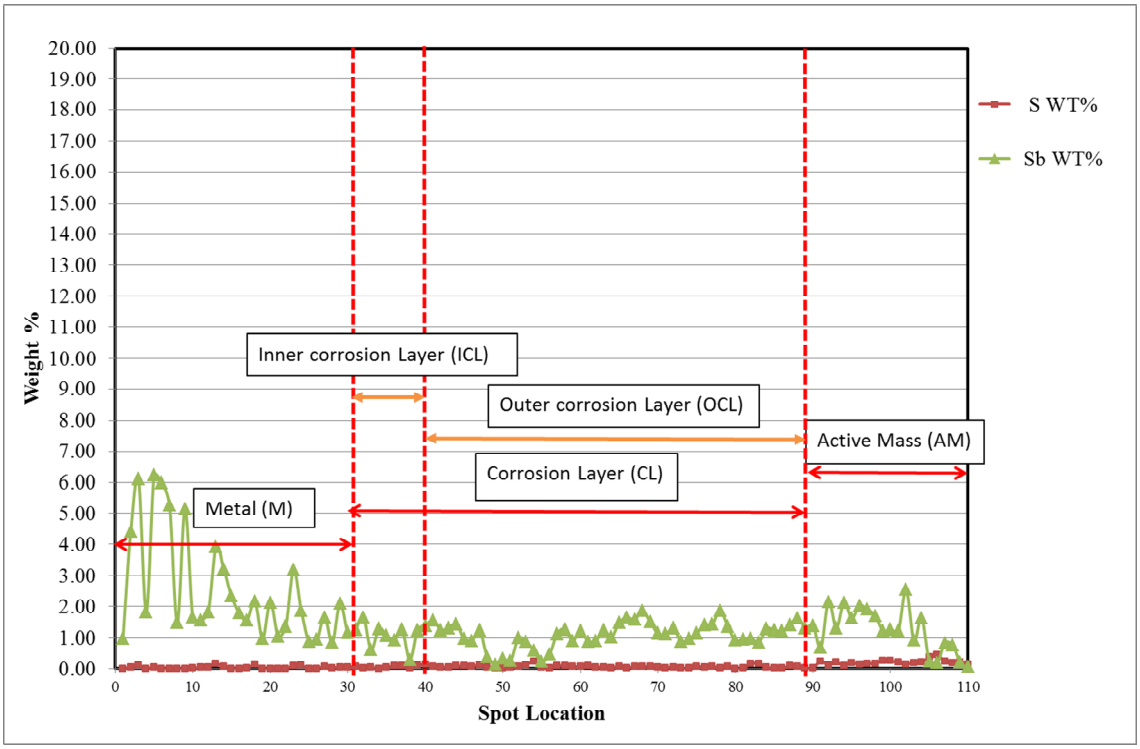

Figure 56 - Quantitative spot analysis of the antimony (Sb) and sulfur (S) composition from Figure 54 with smaller scale

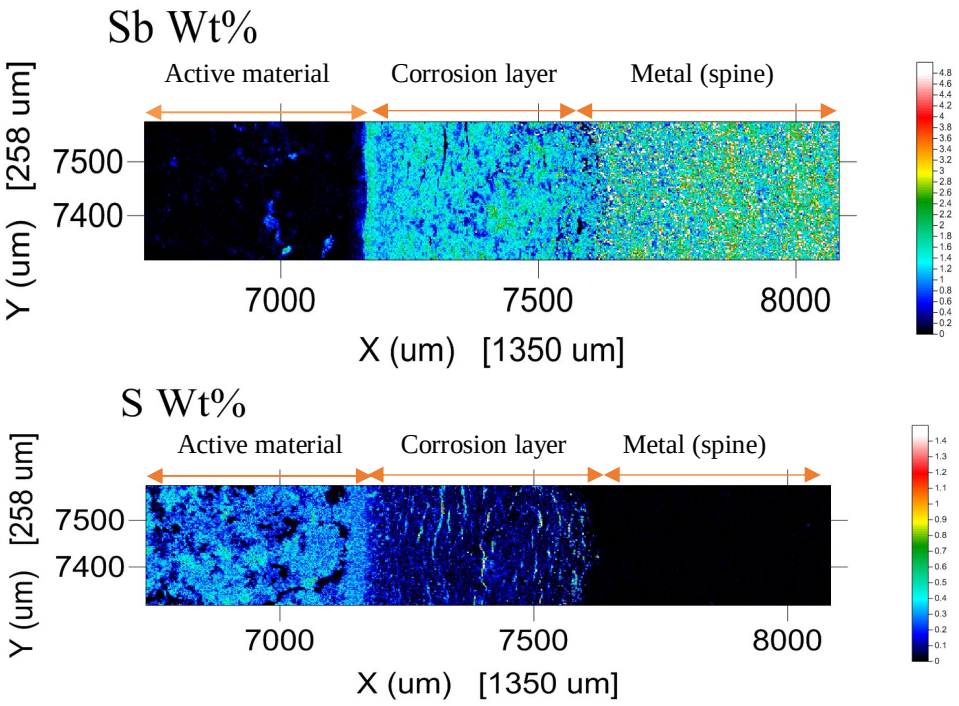

Figure 57 – Area maps for antimony and sulfur

Further cross examinations were conducted to verify Lander's claims. This work was performed on a cross section of a cycled tubular electrode that had a large crack running across the corrosion layer which might be caused by a large defect on the surface of the spine (Figure 58). Under close visual examination, no rich lead sulfate layer could be seen in either the large open crack that cut across the corrosion layer propagation into the spine or anywhere along the path of the large defect corrosion attack area. Results from the quantitative electron microprobe analysis in

Table 5 showed that only a low trace of sulfur (less than 0.2 wt%) was present. The reasons for the absence of this rich lead sulfate layer in the corrosion layer is likely to be the tubular-plate configuration design, where the spine is encapsulated by the active mass thus limiting access of acid to the surface of the spine and the corrosion layer as suggested by Chang & Valeriote (1985). This retardation of acid to the corrosion layer by prevents a lead sulfate barrier from forming in the corrosion layer. In addition, Table 6 results confirmed that significant lead sulfate was present in the corrosion layer of the spine without the active mass when compared to a spine encapsulated with active mass.

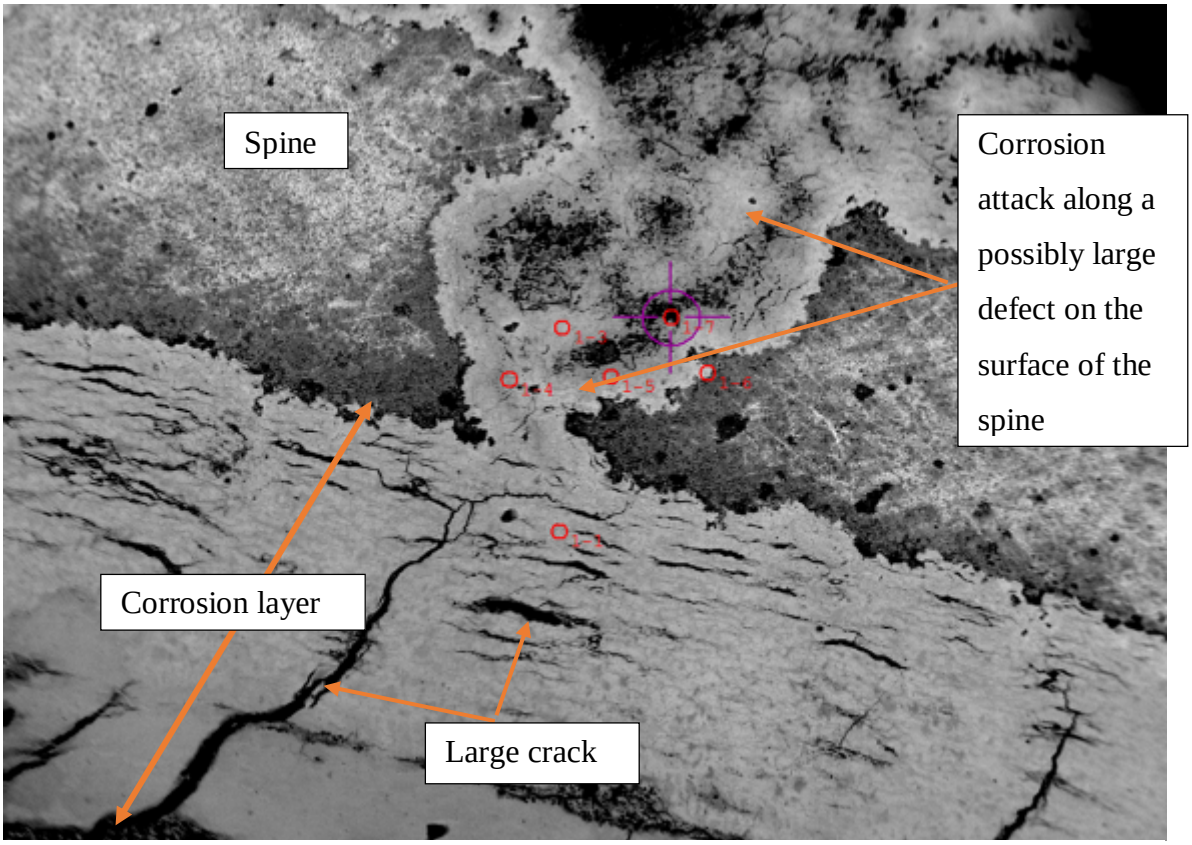

Figure 58 – SEM of a large corrosion defect showing the positions of quantitative electron probe analysis

Table 5 - Quantitative electron probe analysis results at various spots on the areas of Figure 58

SAMPLE	Spot ID	Pb WT%	O WT%	S WT%	Sn WT%	Sb WT%	
S1-6	1	82.4	7.6	0.1	0.0	0.9	Corrosion Layer
S1-6	2	89.4	0.0	0.0	0.0	0.4	Metal
S1-6	3	82.8	2.7	0.1	0.0	0.4	CL entered into metal area
S1-6	4	79.6	2.8	0.1	0.0	2.1	CL entered into metal area
S1-6	5	78.6	0.0	0.1	0.0	1.9	CL entered into metal area
S1-6	6	87.5	4.3	0.0	0.0	0.3	CL entered into metal area (brighter spot)
S1-6	7	72.8	0.5	0.2	0.0	0.5	Black spot

Table 6 – X-ray diffraction (XRD) showing lead sulfate content in the corrosion layer

d = diffraction line	d = 3.49 A	d = 3.12 A		
XRD Result	β-PbO2	α-PbO_2	$PbSO_4$	
Inner Corrosion Layer (ICL)	70.2	22.8	6.9	Cycled with PAM
Outer Corrosion Layer (OCL)	86.2	11.1	2.7	Cycled with PAM
Positive Active Material (PAM)	97.7	1.0	1.4	Cycled with PAM
Positive Active Material (PAM)	87.9	12.1	0.0	Formed, Not Cycled
Corrosion Layer (CL) Spine	9.5	16.6	74.1	Bare spine was subjected to continuous polarization by maintaining constant voltage at 3.0 V for 720 hours

From these results, it may be concluded that a tubular-plate containing low-antimony lead- alloy spines is less likely to develop a rich sulfate passivation layer that other researchers have observed to exist between the metal and the corrosion layer interface under deep-discharge cycling. This rich sulfate passivation layer is known to cause reduced capacity at a rapid rate in conventional SLI plate designs subjected to identical cycling conditions.

5.3 The effect of active mass thickness on stress

Stress is influenced by larger molar volume change of 51% than that of PbO_2 during deep-discharge cycling as suggested by Alzieu and Robert (1987) and Constanti et al. (1995) in Section 3.2. This increase in volume is associated with formation of lead sulfate ($PbSO_4$). However, Simon (1967) has confirmed that the active mass does not exert stresses on the grid despite the large volume change during charge-discharge cycling. It was postulated the thickness of the active mass might affect the corrosion layer: more thickness, more mass; the more ability to resist the volume increase. Hence, the following factors were examined to determine if the thickness of the active mass have any effects on stress.

5.3.1 The effect of active mass thickness on electrode thickness

Atlung and Christiansen (1990) established that an increase in thickness of the plate accumulates from cycle to cycle due to an expansion in volume of the corrosion product. In these circumstances, there may be some correlation between the thickness of the active mass and the electrode thickness. Consequently, thickness of the electrode was measured to determine the amount of volume expansion occurring during deep-discharge cycling. Thicknesses were obtained at three different spots (top, middle and bottom sections) of the electrode. This analysis was performed at cycle numbers 0, 26, 46 and 72. The average thickness of the electrode was plotted against the cycle number as presented in Figure 59. The plot shows the thickness of the electrode has increased with increasing cycle numbers in a linear trend. However, the slope of the curve for active mass thickness for active mass thickness of 2.15 mm (7.3 mm ID) was slightly steeper than that for the 1.60 mm (6.2 mm ID) and 2.80 mm (8.6 mm ID).

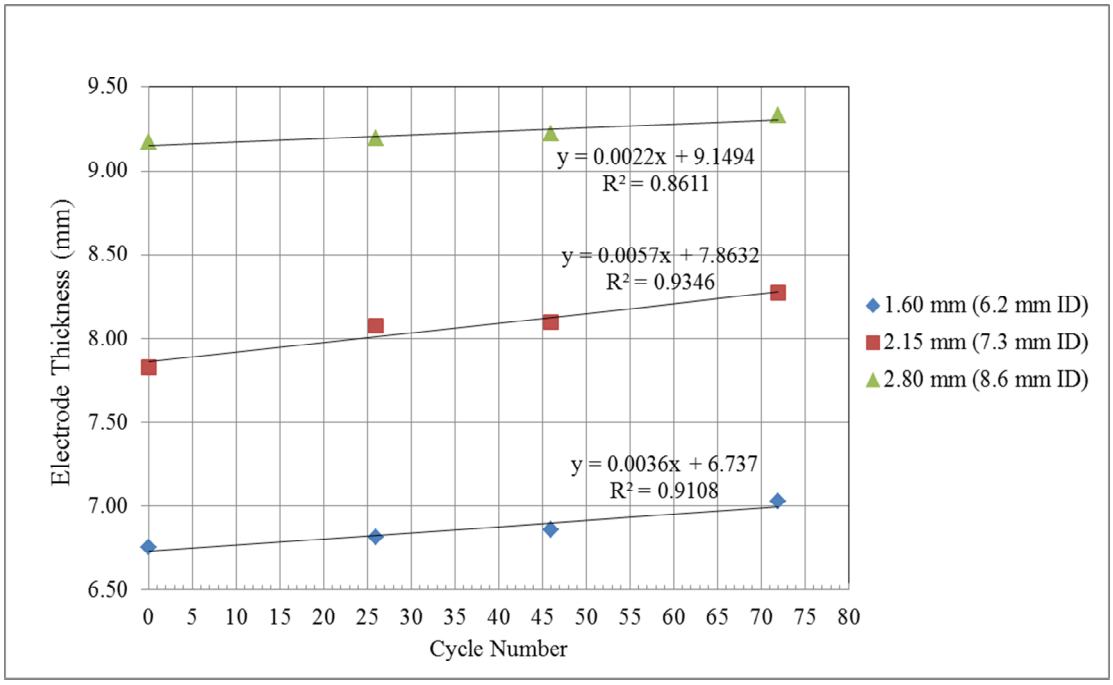

Figure 59 - Electrode thickness increased with increasing cycle number for various active mass thicknesses

In addition, the electrode thickness was also determined at the end a 20 h discharge cycle in comparison to the electrode in a charged state. Figure 60 displays a column chart showing the thickness of the electrode at end of 20 h of discharge and after a full charge. The electrode thickness has increased by 0.06 mm to 0.08 mm at end of the 20 h discharge, which was approximately 1% more than for the charged state. As suggested by Alzieu and Robert. (1986) and Constanti et al. (1995) greater molar volume change of 51% than that of PbO_2 during deep-discharge may be associated with

the formation of lead sulfate ($PbSO_4$). This increase in volume shown in Figure 60 was negligible in comparison to an increased molar volume of 51% that occur in conventional flat plate. The increase in thickness of the electrode may be primarily attributed to the increase in the volume of the corrosion product mainly during polarization (charging) as proposed by Atlung and Christiansen (1990) and possibly some swelling of the active mass during cycling (Pavlov & Bashtavelova 1986). The use of gauntlets in the study shows that regardless of active mass thickness, the active mass is restrained from expanding like the mass in flat plate electrodes, and any expansion observed is very minor.

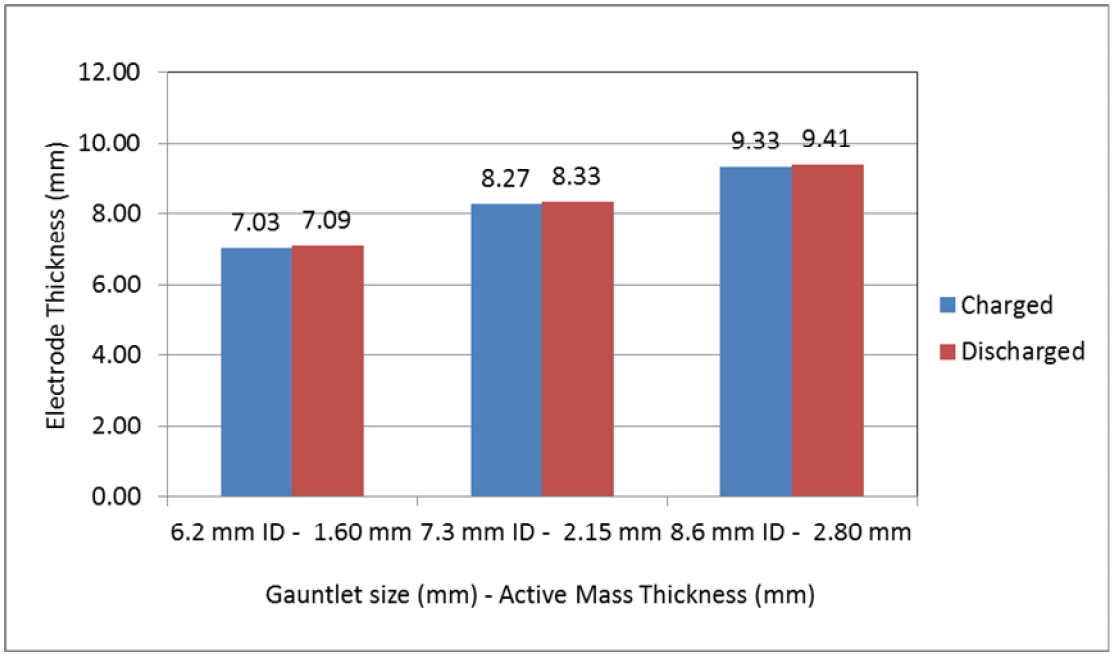

Figure 60 – Thickness of the electrode fully charged and in a discharged state for different active mass thicknesses (Gauntlet diameter)

5.3.2 The effect of active mass thickness on the corrosion layer morphology

The effect of the active mass thickness on the corrosion layer was studied. The morphology of the corrosion product including corrosion layer thickness, cracks and defects can provide valuable information on the potential cycle life of a battery.

5.3.2.1 The effect of active mass thickness on corrosion layer cross-sectional area

Figure 61 is a plot of the active mass thickness against the corrosion layer cross-sectional area. The slopes of the data initially indicate that corrosion layer area increased at a faster rate at commencement of cycling and was slowing down with further cycling. The corrosion layer area plot also showed that the effect of the active mass thicknesses between 1.60 mm, 2.15 mm and 2.80 mm were insignificant. Data points were quite scattered indicating there was inconsistence in the measurements

which may be due defects found during cycling and this will be addressed in Section 5.4. Nevertheless, the trend of the active mass thickness against the corrosion layer area indicated that the corrosion layer area is increased with increasing cycle number. This increase in the corrosion layer during cycling is caused by the increased in volume of the corrosion product (Pavlov 1994; Mahato 1979)

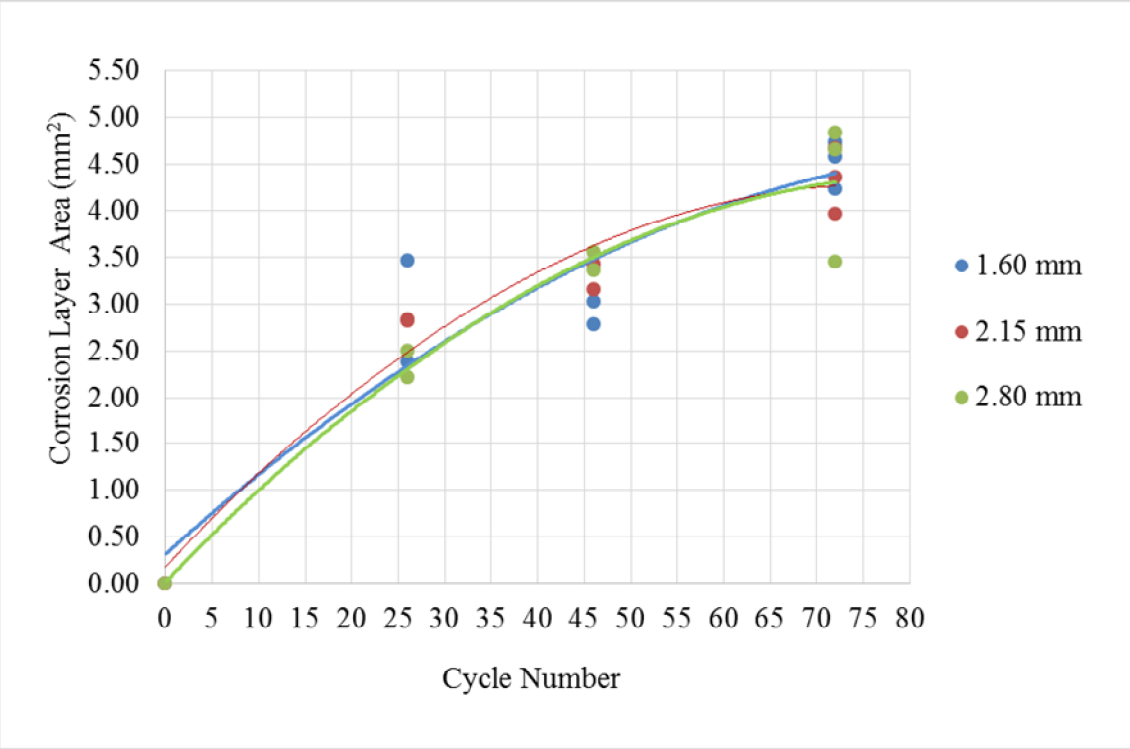

Figure 61 – Increased in corrosion layer area with increasing cycle number for various thickness of the active mass at different cycle stage.

5.3.2.2 The effect of active mass thickness on the number of cracks found in the corrosion layer

The crack pattern of the corrosion layer was closely examined to discover any trend that may be linked to the active mass thickness. As previously mentioned in Section 3.2.2, during the oxidation of lead to PbO_2, the theoretical molar volume is increased by 38%. This increased volume creates stresses and the corrosion layer (CL) is detached and cracked due to stresses developed (Ball et al. 2002; Simon1967). Figure 62 presents a secondary electron back scattered image of a cross section of a cycled electrode. An examination of the corrosion layer confirmed that cracks were formed perpendicular (radial) and parallel (concentric) to the spine. Some cracks were longer and larger than others. The two most obvious large open cracks were those found at

both sides of the spine. These two large cracks were formed as a result of the spine defect which will be explained in Section 5.4.

The cracks occurring within the corrosion layer perpendicular to the spine were counted to determine if there was a relationship between cracks and the active mass thickness. Unfortunately, the cracks that could be quantified were those which were perpendicular to the spine and ran through the corrosion layer; whereas, those parallel to the spine were impossible to count. The number of cracks counted was plotted against the active mass thickness shown in Figure 63. The plot indicates that there were more cracks found in the corrosion layer with active thickness of 1.60 mm and 2.15 mm compared to 2.80 mm at end of cycle number 72. The upwards curve for active thickness 1.60 mm and 2.15 mm suggested that the number of cracks increased with increasing cycle number; whereas the trend for the 2.80 mm curve seemed horizontal suggesting no new cracks were developed during further cycling as far as up to cycle number 72. The plot's trend suggests that plates with thick active mass layers allow stresses to be relieved and assist in reducing the incidence of cracking under deep-discharge cycling. Garche (1995) conducted research on the influence of the active mass thickness on corrosion rate. He found corrosion was reduced with thicker active mass and suggested that stress created from corrosion product formation may be reduced by the partial compensation of the thickness of the active mass. Unfortunately, counting cracks was highly subjective and would have impacted on the accuracy of the numbers.

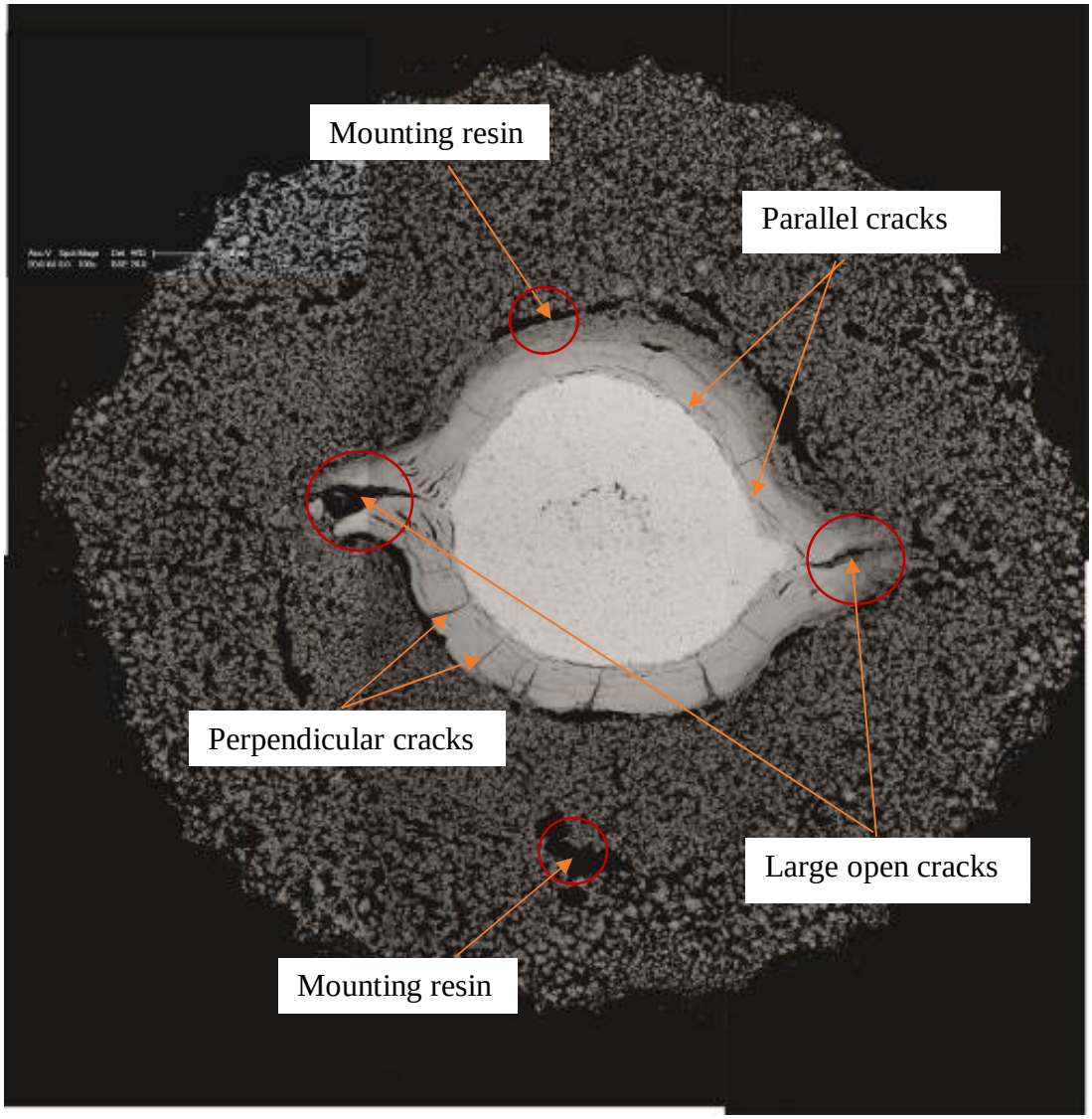

Figure 62 – SEM of cross-section showing cracks perpendicular to the spine

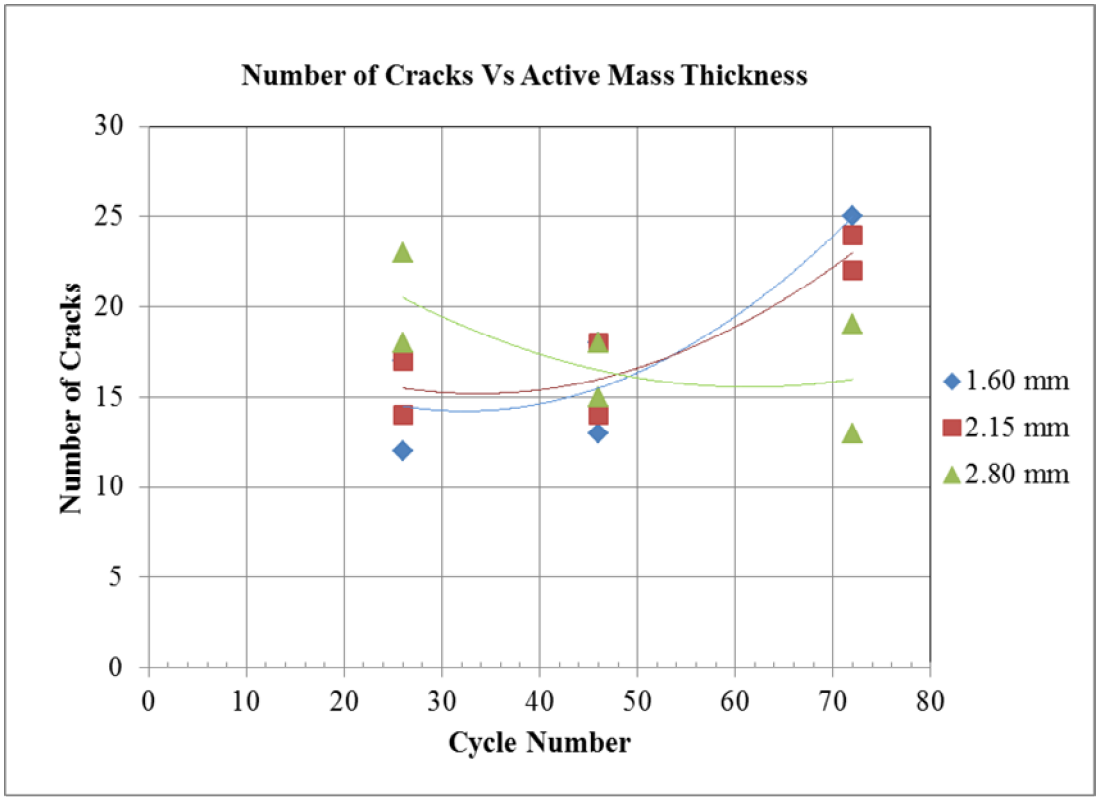

Figure 63 – Number of cracks for various active mass thickness at different cycle stages

5.3.2.3 Effect of the active mass thickness on the porosity of the active mass

A close examination of a cross section of the positive active mass of a charged electrode (Figure 64) was performed. The resulting SEM image revealed the active mass structure was quite porous. However, there was a thin layer of active mass adjacent to the corrosion layer that was noticeably denser than the rest of the surrounding active mass as indicated by the red arrow in Figure 64. This noticeably denser active mass layer possibly resulted from the expansion of the increase in volume of the corrosion product pushing upwards against the active mass and the gauntlet. A very small space can be seen in between the active mass and the corrosion layer; however, it may be an anomaly resulting from the damage occurring during the mounting and preparation of the electrode. Some areas in black may be attributed to presence of the mounting resin. The work of Simon (1967) revealed that the active mass has little effect on applying external stress to the corrosion layer or the spine given the overall volume of space present between the active mass and the corrosion layer. So, in a thicker active mass, there is a larger volume available in which the corrosion layer can expand into, and not much stress comes from the active mass as the stress is

relieved via densification of the active mass. In thinner active mass and there is less volume is available, it is likely that some stress might be exerted on the corrosion layer.

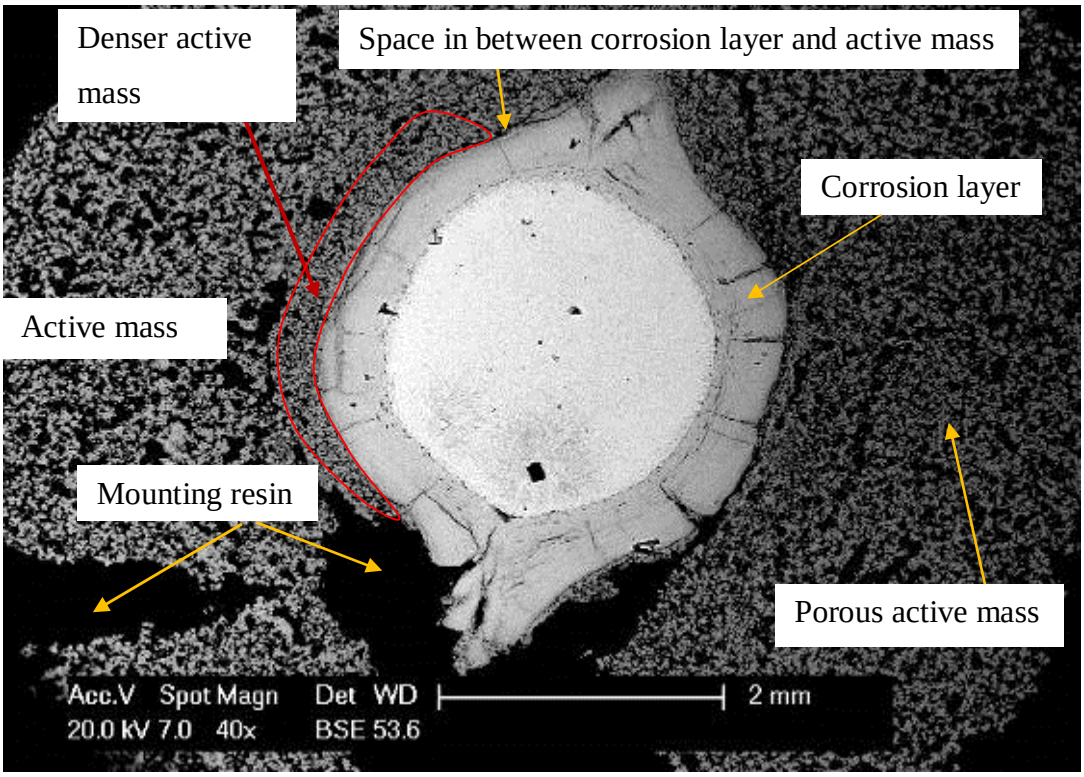

Figure 64 - SEM image of a charged cross section showing porous active mass structure

5.4 Defects that may have influenced the results

A number of defects were discovered and identified during examination of the cross sections. These defects may have contributed to inconsistency to the measurements of the corrosion layer thickness and the cross-sectional area of the spine as illustrated in the following examples:

Sharp corners occurred on all the spines suggesting because the casting die was worn and the two half moulds were not engaged closely during casting, leading to the formation of flashing. Figure 65 illustrates the spine prior to cycling compared to the spine after 46 cycles (Figure 66). Corrosion has clearly occurred at an accelerated rate at these sharp corners and large open cracks with increased corrosion product have formed. Greater in increases in the volume of the corrosion product consequently the greater stress that acted as wedge to force the crack to further open, hence more corrosion product formation. This defect can be reduced by taking measures such as

minimise sharp corners and re-designing the spine to be more even geometrical such as round shape instead of oval or eclipse shape without any sharp corners. Prout (1994) also suggests to avoid rough uneven surface. Corrosion at the rough surface is greater than with smooth surfaces, and rough surface tend to reduce grid life.

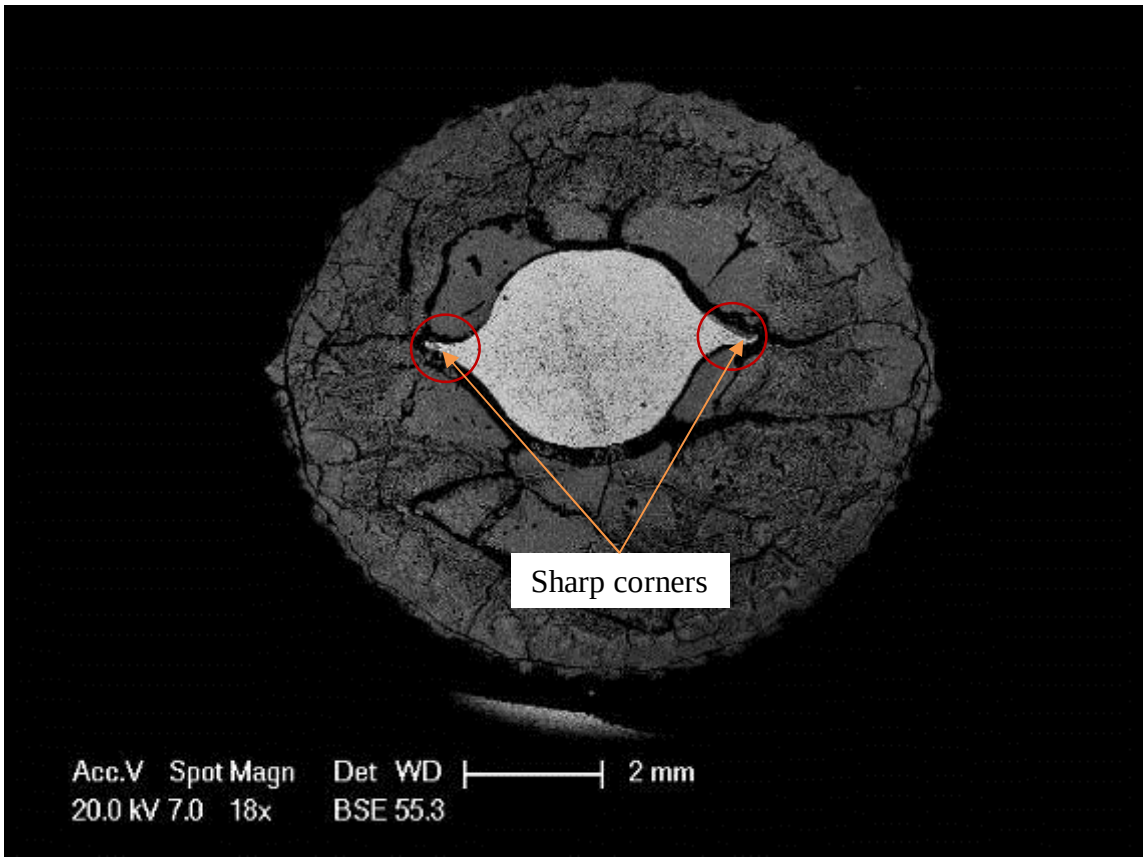

Figure 65 – SEM image of a cross section of an un-formed and un-cycled electrode showing lead spine with sharp corners

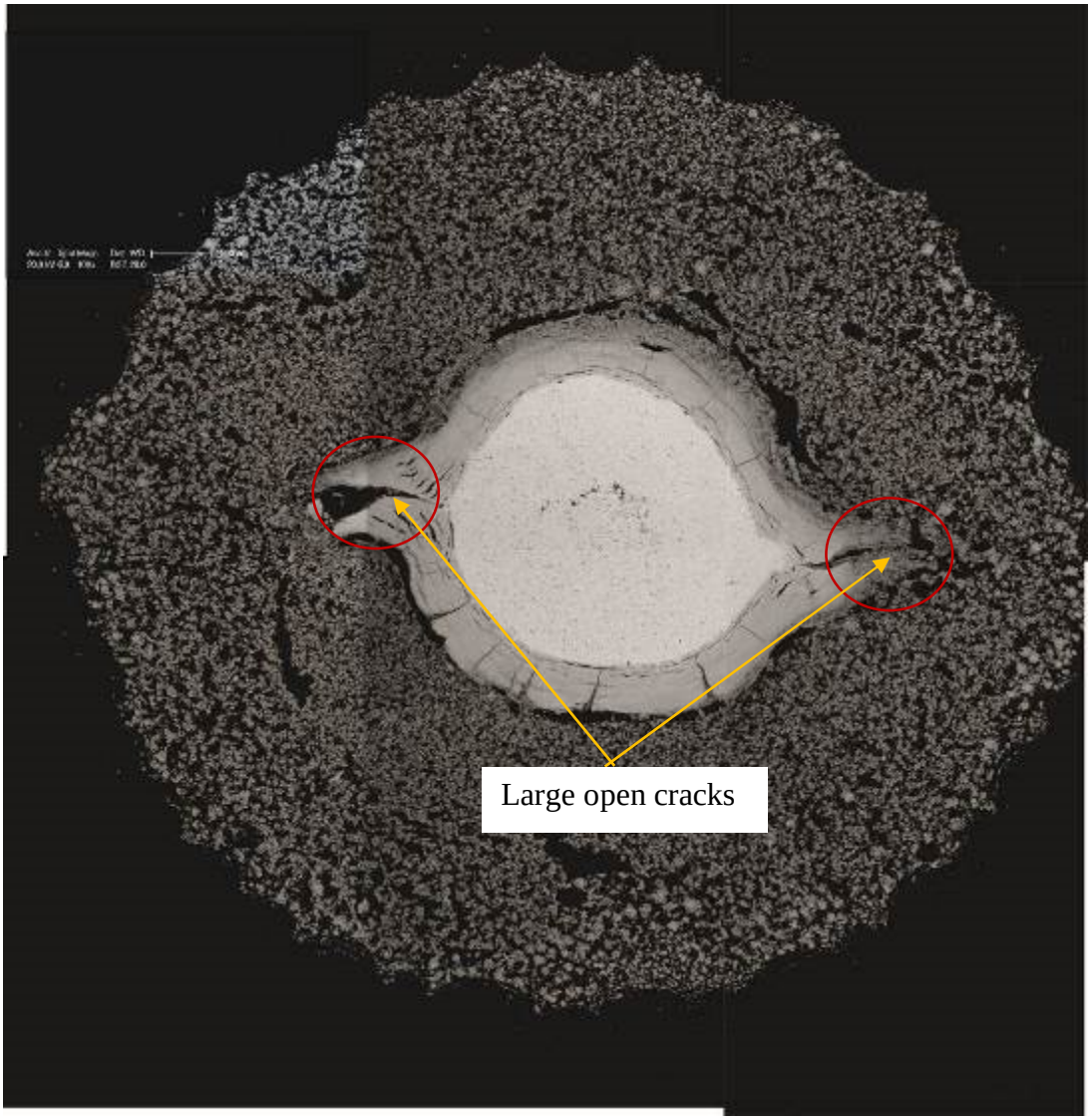

Figure 66 - SEM image of a cross section of the cycled electrode showing accelerated corrosion with large open cracks at sharp corners

Figure 67 illustrated the effect of corrosion when the lead spine was not located central to the gauntlet. Active mass did not uniformly cover the spine. The sharp corner side which was sitting close to the gauntlet with less active mass cover, developed a significant thicker corrosion layer than the opposite sharp corner with more active mass coverage. These effects are possibly due to the easy pathway for acid to reach the sharp sections and that crack initiation and growth always occur at discontinuities and sharp edges. The impact of this defect could be reduced by ensuring that the spine is centrally located in the gauntlet to provide uniform active mass cover.

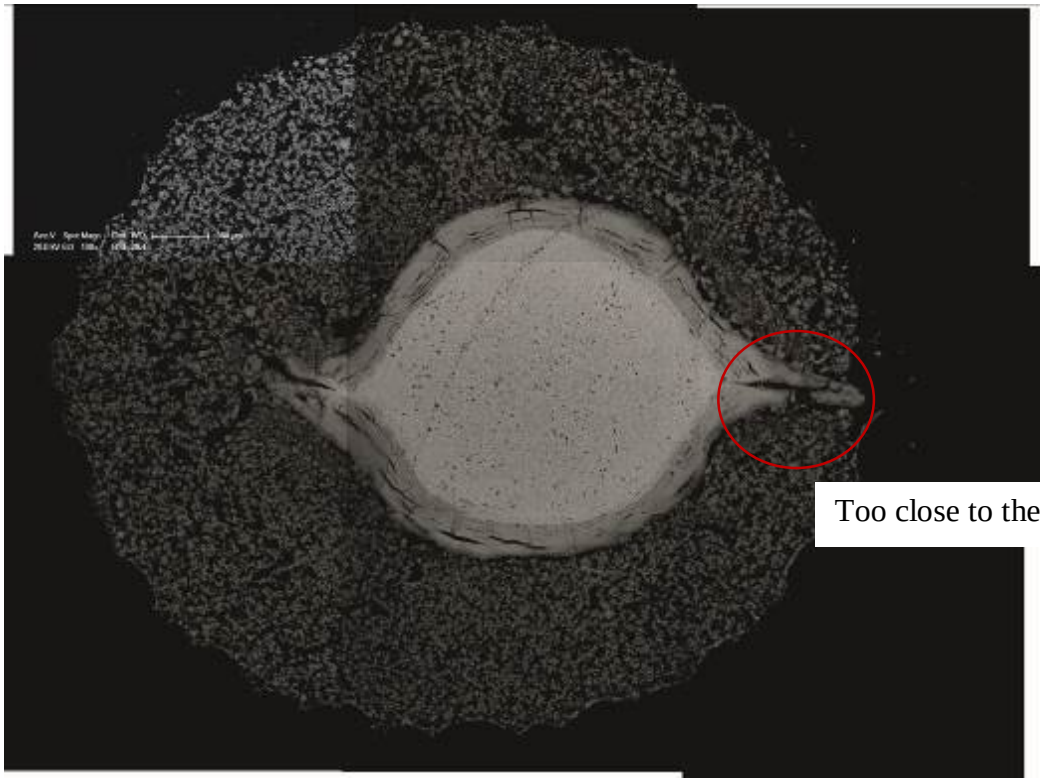

Figure 67 – SEM image of the spine was not sitting central to the gauntlet

Voids found on the surface of the spine are shown in Figure 68 and Figure 69. These voids are not visible to the naked eye. Although the voids may not be at the surface, gradual corrosion will expose them and may provide sites for further corrosion into the spines later in life.

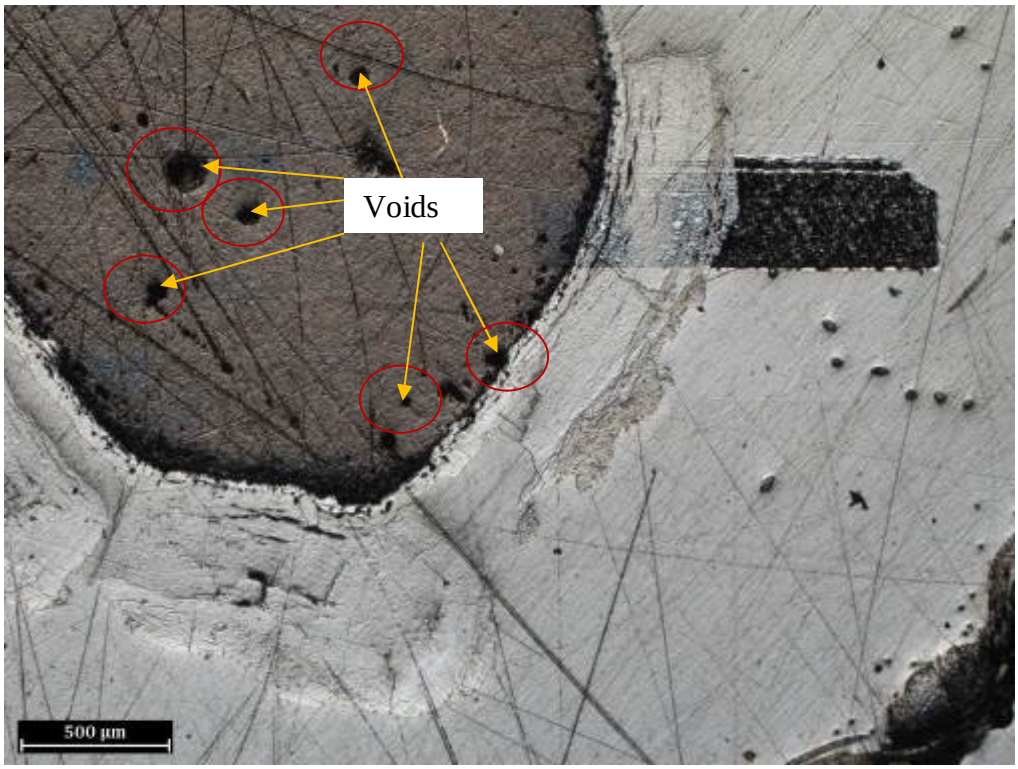

Figure 68 – Optical image showing a number of large voids in the lead spine

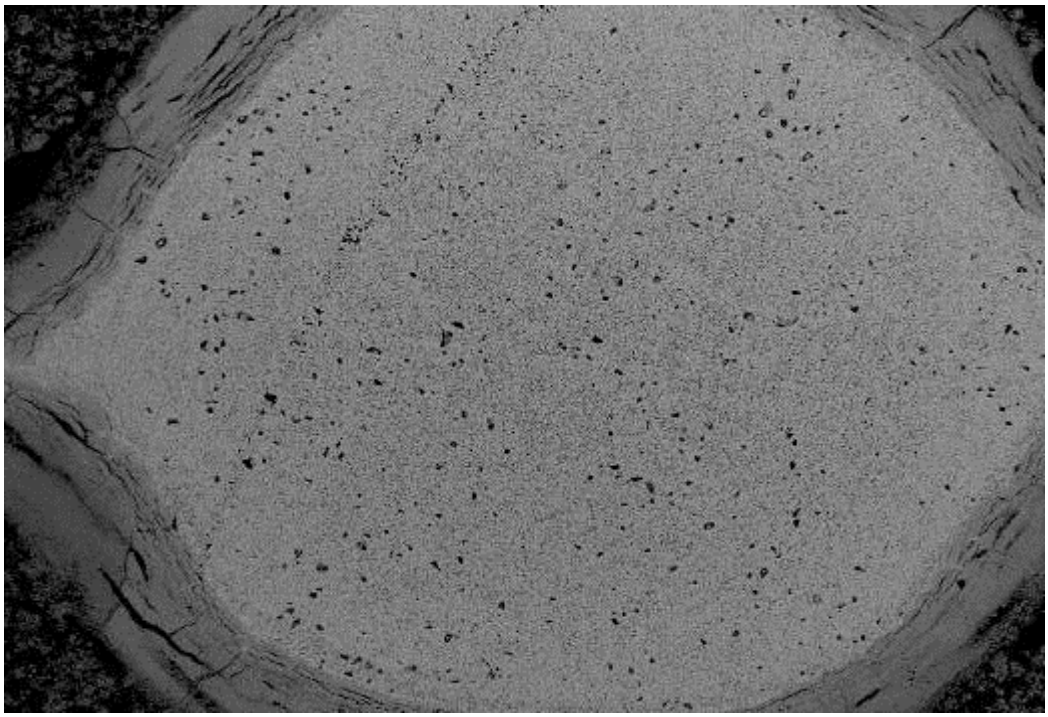

Figure 69 – Close up of the above SEM image showing porosity in the spine

Figure 70 and Figure 71 illustrated corrosion attack which may be due to defects in casting along the grain boundaries, voids or cracks. Corrosion product has penetrated at a rapid rate compared to the other parts along the spine. This creates a weak point for the spine to fracture which may limit the cycle life of the battery.

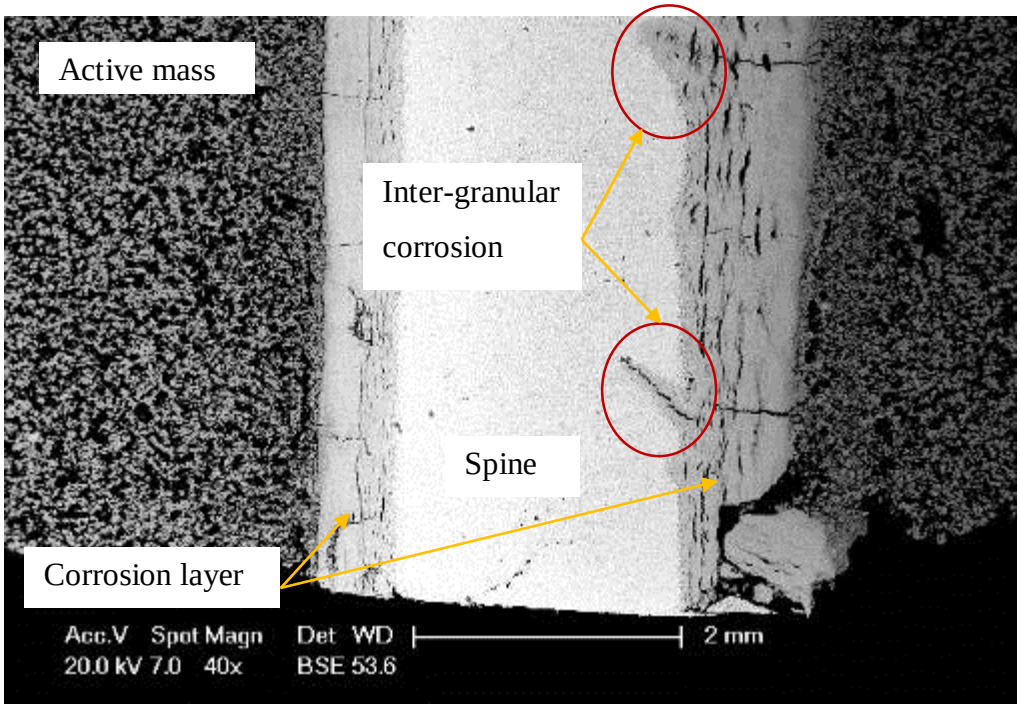

Figure 70 - SEM image of corrosion attack along the defect areas at 40x magnification

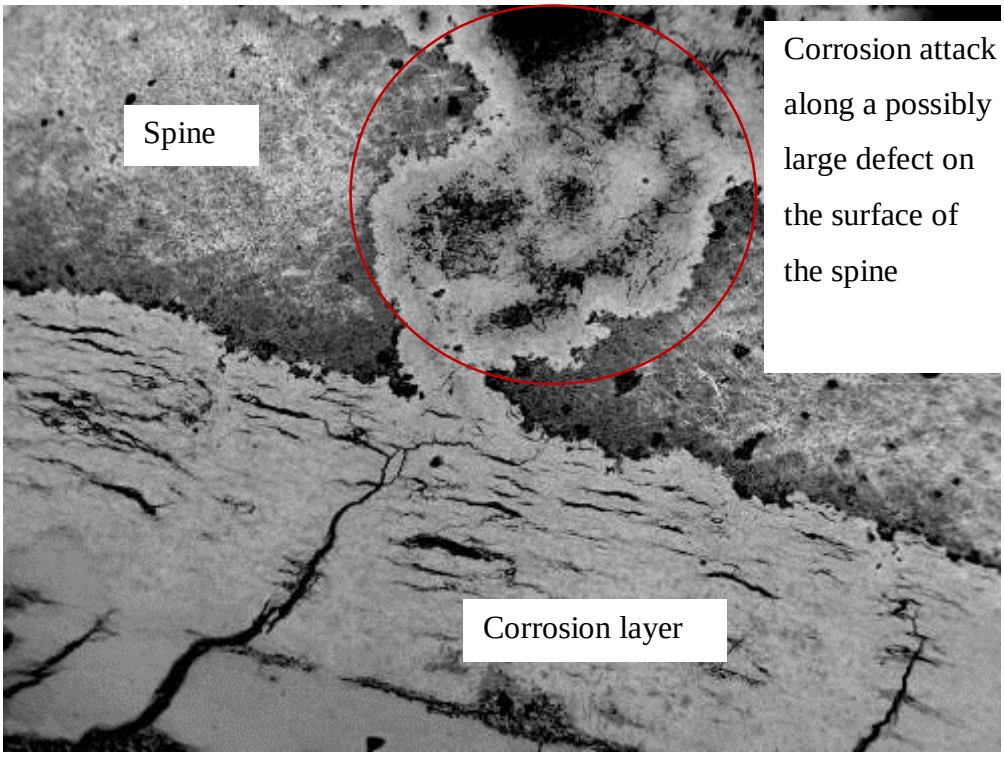

Figure 71 – Close up SEM image that may be due to corrosion attack along the a large casting defect at 400x magnification

Figure 72 illustrated a dislodged outer corrosion layers which may have been damaged during preparation of the cross section due to the very friable and brittle nature of the mass. The layer was broken and sections were missing, possibly dislodged out of place so there was no complete corrosion layer. Therefore, an estimate of the corrosion layer was originally sit, was marked out by line X (Figure 72). This enabled the approximation of the corrosion layer area to be calculated. However the inner corrosion layer still remained intact. This confirmed that the inner corrosion was adhered strongly to the spine. This behavior was also observed by Miraglio, Albert, El Ghachcham, Steinmetz & Hilger (1995), they noted that a thick outer corrosion layer composed of PbO_2 is formed on the inner corrosion layer of PbO. The outer corrosion layer is not as compact as the inner corrosion layer. The adhesion of the outer corrosion layer PbO_2 is much lower by comparison with that of the inner corrosion layer especially as the outer corrosion layer get thicker since it is easily break away during the preparation of the electrodes for SEM. Pavlov (1994) and Mahato (1979) established that the corrosion layer consists of two distinct layers. The inner layer is dense whilst the outer is porous as illustrated in Figure 13. Microscopic studies confirm that the dense layer is closest to the spine (metal) surface. The dense layer is brownish and strongly adheres to the spine

and it can only be chemically removed. The porous layer lies between the dense layer and the PAM. This outer layer is porous, dark brown and loose.

Furthermore, a conducted experiment of bare spines were exposed to sulfuric acid and constant current charging, developed an oxidised surface. The spines from this experiment are shown in Figure 73 showed that the outer corrosion layer tends to free itself by shedding away from the inner corrosion layer has confirmed Pavlov (1994) and Mahato (1979) finding. As the corrosion layer increases in thickness, the outer corrosion layer becomes more brittle and friable which makes it harder for the active mass alone to hold it in place. It is well known that tubular traction lead-acid batteries have longer cycle life than traction lead-acid batteries constructed with flat plates. A key reason is that the gauntlet retains the outer corrosion layer and the active mass from shedding especially during deep-discharge cycling, thereby resulting in reduced loss of capacity and extending cycle life.

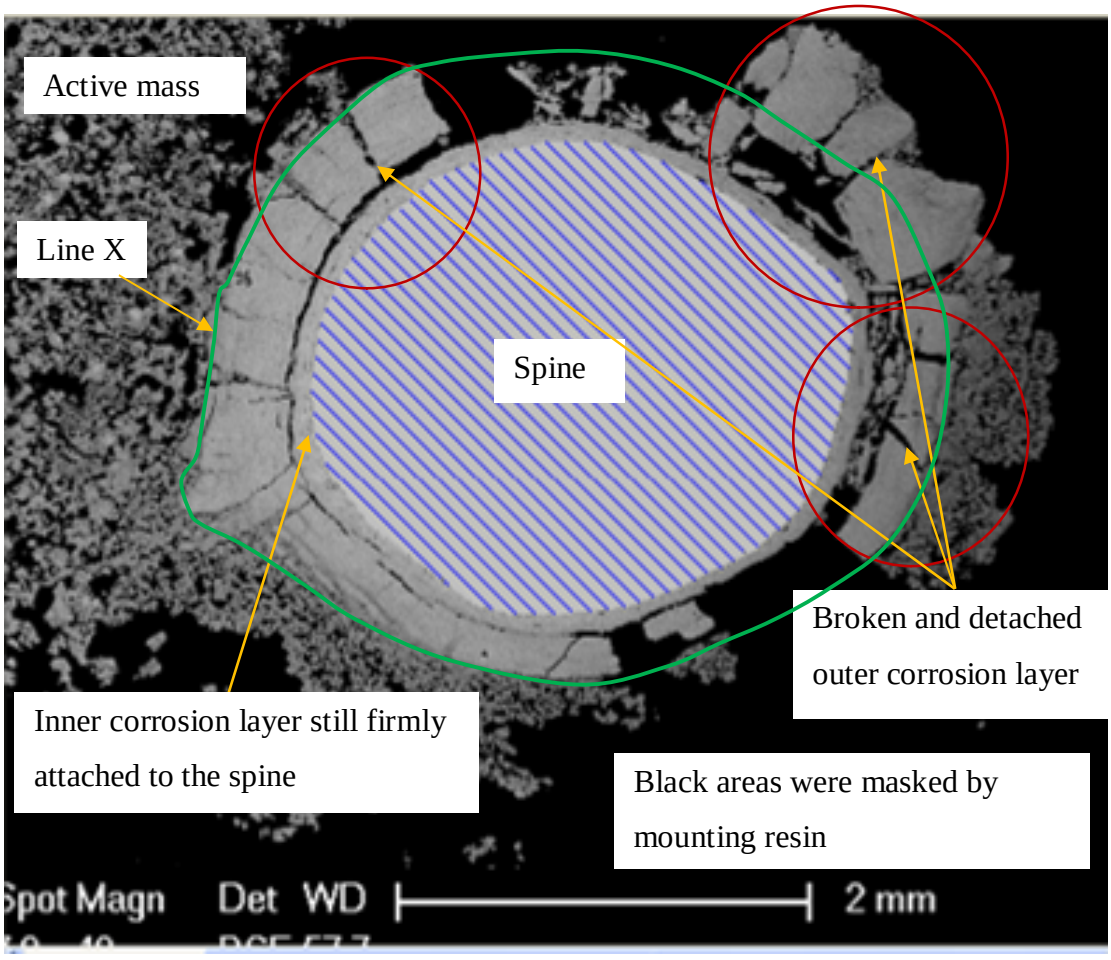

Figure 72 – SEM showing detached broken corrosion layer due to poor adhesion outer layer

Figure 73 – shedding of the outer corrosion due to increase in corrosion product

5.5 Conclusion

The purpose of this study was to investigate the effect of the active mass thickness on the cycle life of low-antimony lead-alloy spine employed in deep-cycle batteries. The following results summarised the outcomes of the study:

The effect of active mass thickness on the cycle life was examined by monitoring the cell capacity performance. Results obtained from the cell capacity performance indicated that tubular-plate with low-antimony lead-alloy spine with active mass thickness of 1.60 mm, 2.15 mm and 2.80 mm have not exhibited signs of rapid reduced capacity under repetitive 20 h discharge cycling.

Quantitative electron microprobe analysis was used to investigate the distribution of sulfur and antimony in the corrosion layer. Results revealed rich layer of lead sulfate was not present in either the corrosion layer or the corrosion layer interface. The reason for the absence of this rich lead sulfate layer in the corrosion layer is likely to be the tubular-plate design. The active mass completely surrounded the spine limiting the access of acid in the spine corrosion layer interface. Because of the limited acid access, the corrosion layer does not participate in the discharge of the cell, thereby preventing a lead sulfate barrier from forming in the corrosion layer.

Corrosion measurements showed that the electrode with the thickest active mass thickness of 2.80 mm had the lowest amount corrosion of the spine, whereas with active mass thicknesses of 2.15 mm and 1.60 mm, the amount of corrosion was higher and similar corrosion. Although lowest corrosion measurement was observed with the thickest active mass thickness of 2.80 mm after cycle number 72, but could not be established that corrosion is reduced with increases in active mass thickness due to inconsistent corrosion results obtained from the active mass thicknesses of 1.60 mm and 2.15 mm and especially without the bare spine to include in the plot.

The active mass was examined during cycling for cracks and porosity. No cracks were found in the active mass. The active mass was porous, thus unlikely to have applied any external force on the corrosion layer or the spine to create the cracks in the corrosion layer.

The corrosion layer was subjected to stress when the electrode was subjected to repetitive deep-discharge cycling. The thickness of the electrode was measured through various stages during cycling. Results indicated that the electrode thickness increased with increasing cycle number. The increase in thickness was mainly contributed due to the growth of the corrosion layer, as a result from an increase in the corrosion product formed during deep-discharge cycling. This increase in size and an observed increase in number of cracks were found with increasing corrosion layer thickness. This suggested that stress was caused by an increase in the corrosion layer thickness and the stress is relieved via crack formation.

Using the measurement of residual cross-sectional area, as opposed to grid weight or grid growth to measure corrosion, it was found to be significantly beneficial for this study. Observations of the cross-sectional area have provided insights into the morphology of the corrosion layer, battery failure mode and highlighted number of defects in the electrode which can be reduced to extend the cycle life of the batteries.
A number of defects were found, such as:

- lead spine with sharp points or corners on the surface;
- Rapid corrosion attack due to defects in the casting;
- voids in the spine;
- lead spine was not centrally located in the gauntlet.

These identified defects in the electrode possibly lead to the spine metal being corroded at a much accelerated rate. This accelerated rate of corrosion impacted on the life of the grid, which could not be offset by the encapsulation of the active mass thickness.

Based on these findings, the conclusion is that the cycle life of positive tubular-plate lead-acid batteries containing low-antimony lead-alloy was limited by grid corrosion resulting from stress. Rich layer of lead sulfate was not found in the corrosion layer due to the spine was encapsulated by the active mass. Grid corrosion was found to reduce with the thickest active mass thickness but there was not enough evidence to establish that increased in the active mass thickness reduced corrosion, hence on the cycle life of low-antimony lead-alloy spine employed in deep-cycle batteries. Therefore, low-antimony lead-alloy grid is more suitable to be used in the design of tubular grid for deep-discharge cycling. Thicker lead spine with a round geometrical design and even surface areas is required for regular deep-discharge cycling due to an increased in corrosion.

6 Recommendations for future study

Some of the following recommendations may be useful and beneficial for the future study in regard to consistent measurements and a more definite result.

- Use spines with even surface areas without surface discontinuities such as flashing and burrs for more uniform corrosion.

- In this study only three different active mass thicknesses were used. However, a wider range of active mass thicknesses between 0 and 3.0 mm will provide a better correlation.

- Cycling ceased after 72 cycles, the outcome of the results would be more definite if the cycling was continued until failure or up to 110 cycles to provide a further two plot data points for better indication of the plot trend.

- The use of alternative technique for polishing such as ultra-microtoming to minimise the destruction to the corrosion layer.

7 References

Alzieu, J & Robert, J 1986, 'Cycle life of stressed lead-acid batteries', *Journal of Power Sources*, vol. 13, pp. 93-100.

Atlung, S & Zachau Christiansen, B 1990, 'Degradation of the positive plate of the lead-acid battery during cycling', *Journal of Power Sources*, vol. 30, pp. 131-141.

Bagshaw, NE 1997, 'Improving active material utilization', *Journal of Power Sources*, vol. 67, pp. 105-109.

Ball, RJ, Kurian, B, Evans, R & Stevens, R 2002, 'Failure mechanisms in valve regulated lead/acid batteries for cyclic applications', *Journal of Power Sources*, vol. 109, pp. 189-202.

Barrett, D, Frost, MT, Hamilton, JA, Harris, k, Harrowfield, IR, Morseby, JF, & Rand, DAJ 1981, 'Laboratory simulated studies of lead-acid traction batteries under duty cycles normal to electric vehicle service', *Journal of Electroanalytical Chemistry*, vol. 118, pp. 131-155.

Battrien, 2002, Battery Technology Handbook, trans. HA Kiehne, Marcek Dekker, New York.

Berndt, D & Nijhwan, SC 1976, 'Lead-acid batteries with low antimonial alloys', *Journal of Power Sources*, vol. 1, pp. 3-15.

Chang, TG & Valeriote, EM 1985, 'Effects of curing and other variables on deep-discharge cycling of Pb-Ca positive plates', *Journal of The Electrochemical Society*, vol. 132, pp. 1983-1987.

Constanti, KK, Hollenkamp, AF, Koop, MJ & McGregor, K 1995, ' Physical change in positive-plate material – an underrated contributor to premature capacity loss', *Journal of Power Sources*, vol. 55, pp. 269-275.

Donovan, JJ & Tingle, TN 1996, 'An Improved Mean Atomic Number Background Correction for Quantitative Microanalysis', *Microscopy and Microanalysis*, vol.1, pp. 1-7.

Garche, J 1995, 'Corrosion of lead and lead alloys: Influence of the active mass and of the polarization conditions', *Journal of Power Sources*, vol. 53, pp. 85-92.

Giess, H 1995, 'The influence of calcium, tin and grid thickness on corrosion-induced grid growth', *Journal of Power Sources*, vol. 53, pp. 31-43.

Hollenkamp, A, Constanti, K, Koop, M, & Apiiteanu, L 1994, 'Effects of grid alloy on the properties of positive-plate corrosion layers in lead/acid batteries. Implications for premature capacity loss under repetitive deep-discharge cycling service', *Journal of Power Sources*, vol. 48, pp. 195-215.

Kurzweil, P 2010, 'Gaston Planté and his invention of the lead–acid battery-The genesis of the first practical rechargeable battery', *Journal of Power Sources*, vol.195, pp. 4424–4434.

Lander, JJ, Simon, AC & Jones, EI 1958, 'The effect of corrosion and growth on life of cycling lead-acid cells', *Naval Research Laboratory Report 4347*, January 31, pp. 1-16.

Lehockey, EM, Limoges, D, Palumbo, G, Sklarchuk, J, Tomantschger, K, & Vincze, A 1999, 'On improving the corrosion and growth resistance of positive Pb-acid battery grids by grain boundary engineering', *Journal of Power Sources*, vol.78, pp. 79–83.

Mahato, KB 1979, 'The cyclic corrosion of the lead-acid battery positive', *Journal of Electrochemical Science and Technology*, vol.126, pp. 365–374.

Miraglio, R, Albert, L, El Ghachcham, A, Steinmetz, J & Hilger, JP 1995, 'Passivation and corrosion phenomena on lead-calcium-tin alloys of lead/acid battery positive electrodes', *Journal of Power Sources*, Vol. 53, pp. 53-61.

Pablov, D 1994, 'Effect of corrosion layer on phenomena that cause premature capacity loss in lead/acid batteries', *Journal of Power Sources*, vol.48, pp. 179-193.

Pablov, D 1995, ‘A theory of the grid/positive active-mass (PAM) interface and possible methods to improve PAM utilization and cycle life of lead.acid batteries’, *Journal of Power Sources*, vol.53, pp. 9-21.

Pavlov & Bashtavelova 1986, ‘Structural properties of the PbO_2 active mass determining its capacity and the “Breathing” of the positive plate during cycling’, *Journal of The. Electrochemical. Society*, Vol 133, pp. 241-248.

Papazov, G, Rogatchev, T & Pablov, D 1981, ‘Influence of the lead dioxide active mass on the corrosion rate of the spines of positive lead-acid battery plates’, *Journal of Power Sources*, vol.6, pp. 15-24.

Prout, L 1994, ‘Aspects of lead/acid battery technology - Grids’, *Journal of Power Sources*, vol.50, pp. 193-257.

Prengaman, RD 2009, ‘Lead alloys’, Elsvier B.V., pp. 648-654.

Rogatchev, T, Papazov, G, & Pavlov, D 1983, ‘The effect of current density and thickness of the active mass upon the corrosion rate of the spines of lead-acid battery plates’, *Journal of Power Sources*, vol. 10, pp. 291- 303.

Ruetschi, P 2004, ‘Aging mechanisms and service life of lead–acid batteries’, *Journal of Power Sources*, vol. 127, pp. 33–44.

Ruetschi, P 1977, ‘Review on the lead-acid battery science and technology’, *Journal of Power Sources*, vol. 2, pp. 3–24.

Shiomi, M, Okada, Y, Tsuboi, Y, Ssumi, S & Tsubota, M 2003, ‘Study of PCL mechanism influence of grid/PAM state on PCL’, *Journal of Power Sources*, vol. 113, pp. 271–276.

Simon, AC 1967, ‘Stress corrosion in the grids of the lead-acid storage battery’, *Journal of Electrochemical Science*, vol. 114, pp. 1–8.

Toniazzo, V 2006, ‘New generation of non-wooven gauntlets for tubular positive plates’, *Journal of Power Sources*, vol. 158, pp. 1062–1068.

Willihnganz, E 1988, ‘The effect of positive polarization on grid growth, cell performance and life’, *IEEE Xplore*, pp. 124-131.

Appendix A – Calibration results of the charge-discharge units

This appendix provided the calibration results for the charge-discharge units used in the capacity testing of the cells.

Table A 1 showing the calibration results and the calibration plots for charge and discharge mode (Figure A 1 and Figure A 2) respectively of the charge-discharge unit #1

Table A 1 - Showing the calibration results of the charge-discharge unit #1

Charge Mode			
Set Current (mA)	Monitor current (mA)	Actual Current (mA)	Error %
100.0	98.8	99.9	-0.1
300.3	299.2	301.6	0.4
500.6	499.5	503.2	0.5
1000.0	999.0	1005.7	0.6
1500.2	1498.8	1508.6	0.6
1700.6	1699.2	1710.3	0.6
2000.9	1999.5	2012.4	0.6
Discharge Mode			
Set Current (mA)	Monitor current (mA)	Actual Current (mA)	Error %
10.0	14.0	9.5	-5.0
30.1	34.3	30.0	-0.3
50.4	54.7	50.5	0.2
70.7	75.2	71.0	0.4
90.0	94.6	90.0	0.0
100.6	105.3	101.0	0.4
150.0	155.0	151.0	0.7
170.2	175.3	171.0	0.5
200.2	205.5	202.0	0.9
250.4	256.0	253.0	1.0

- Set current - current that the charge-discharge unit was set to for calibration
- Monitor current - current showing from the charge-discharge unit feedback
- Actual current - current obtained from the multimeter connected in series with the charge-discharge unit and the battery.
- Error % = ((Actual current - Set current)/Set current))*100

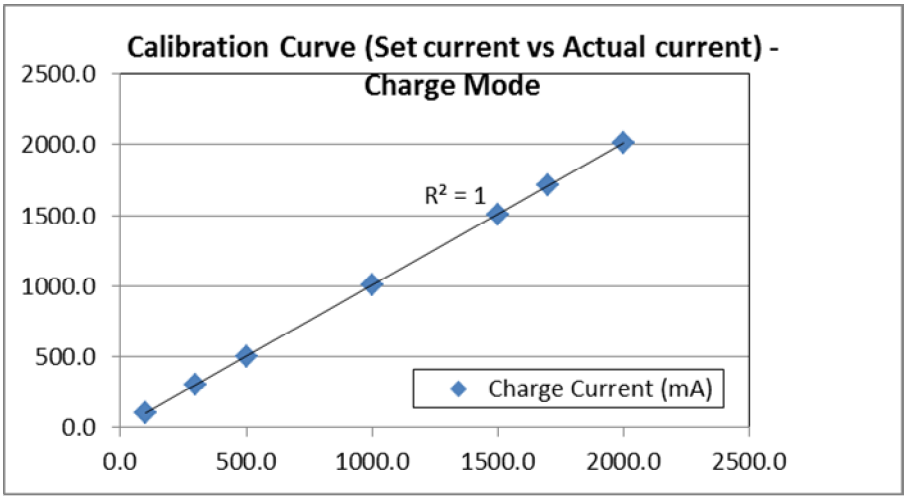

Figure A 1 - Calibration curve at charge mode for charge-discharge unit #1

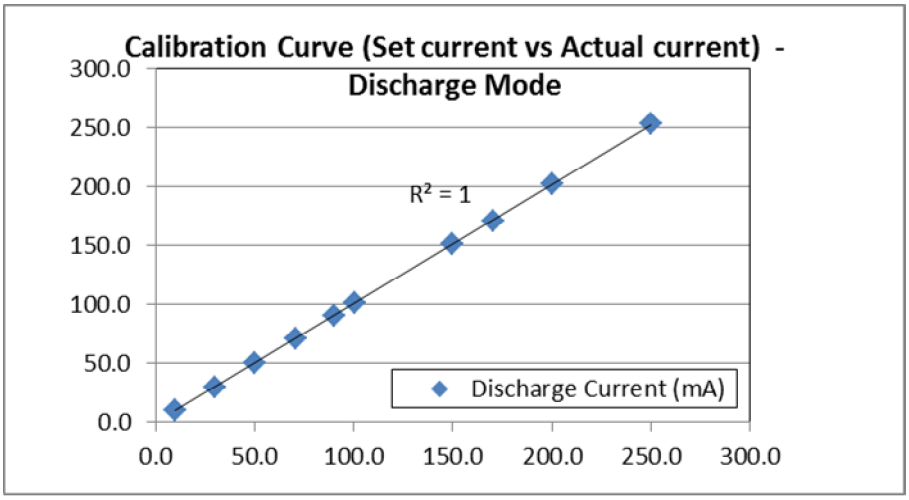

Figure A 2 - Calibration curve at discharge mode for charge-discharge unit

Table A 2 showing the calibration results and the calibration plots for charge and discharge mode (Figure A 3 and Figure A 4) respectively of the charge-discharge unit #2

Table A 2 - Showing the calibration results of the charge-discharge unit #2

Charge Mode			
Set Current (mA)	Monitor current (mA)	Actual Current (mA)	Error %
100.0	100.6	101.7	1.7
299.6	300.3	305.4	1.9
500.0	500.6	506.1	1.2
999.9	1000.6	1012.0	-0.1
1500.9	1500.8	1519.3	0.0
1700.1	1700.4	1721.0	0.0
2000.0	2000.1	2024.4	0.0
Discharge Mode			
Set Current (mA)	Monitor current (mA)	Actual Current (mA)	Error %
10.1	14.0	10.0	-1.0
29.7	33.0	30.0	1.0
50.3	53.0	51.0	1.4
69.9	73.0	71.0	1.6
90.5	94.0	92.0	1.7
100.3	104.0	102.0	1.7
150.3	154.0	152.0	1.1
169.9	174.0	173.0	1.8
200.4	204.0	203.0	1.3
249.7	254.0	255.0	2.1

- Set current - current that the charge-discharge unit was set to for calibration
- Monitor current - current showing from the charge-discharge unit feedback
- Actual current - current obtained from the multimeter connected in series with the charge-discharge unit and the battery.
- Error % = ((Actual current - Set current)/Set current))*100

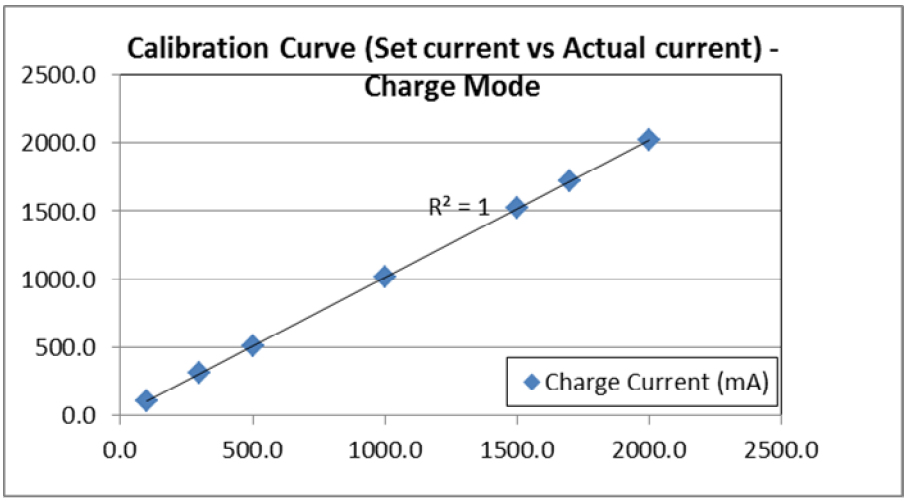

Figure A 3 - Calibration curve at charge mode for charge-discharge unit #2

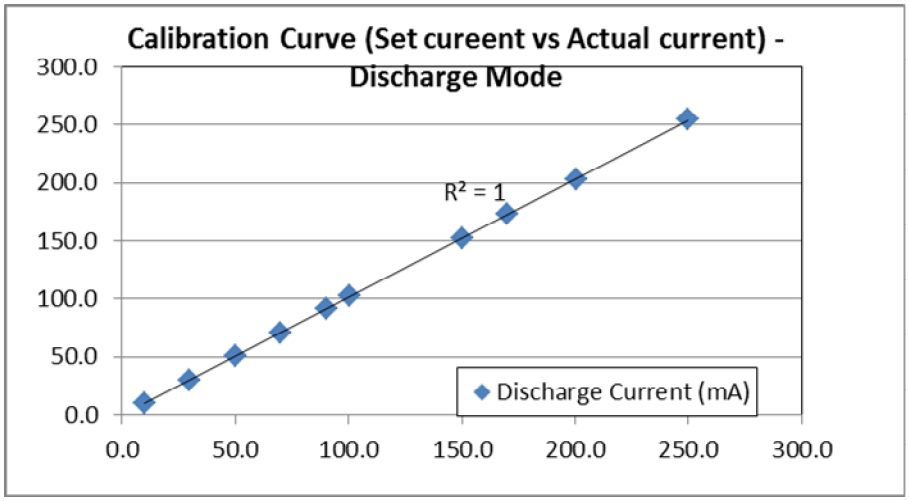

Figure A 4 - Calibration curve at discharge mode for charge-discharge unit #2

Table A 3 showing the calibration results and the calibration plots for charge and discharge mode (Figure A 5 and Figure A 6) respectively of the charge-discharge unit #3

Table A 3 - Showing the calibration results of the charge-discharge unit #3

Charge Mode			
Set Current (mA)	Monitor current (mA)	Actual Current (mA)	Error %
100.3	101.1	101.8	1.5
299.8	300.6	303.1	1.1
500.2	501.1	505.4	1.0
999.9	1000.8	1009.5	1.0
1500.0	1501.2	1514.2	0.9
1699.9	1701.1	1715.5	0.9
1999.9	2001.2	2018.3	0.9
Discharge Mode			
Set Current (mA)	Monitor current (mA)	Actual Current (mA)	Error %
10.0	10.1	10.9	9.0
30.0	30.1	31.2	4.0
50.0	50.2	51.5	3.0
70.0	70.2	71.7	2.5
90.0	90.3	92.0	2.2
100.1	100.4	101.9	1.8
150.1	150.5	153.0	2.0
170.0	170.4	173.0	1.8
200.0	200.5	203.5	1.7
249.7	250.6	254.1	1.8

- Set current - current that the charge-discharge unit was set to for calibration
- Monitor current - current showing from the charge-discharge unit feedback
- Actual current - current obtained from the multimeter connected in series with the charge-discharge unit and the battery.
- Error % = ((Actual current - Set current)/Set current))*100

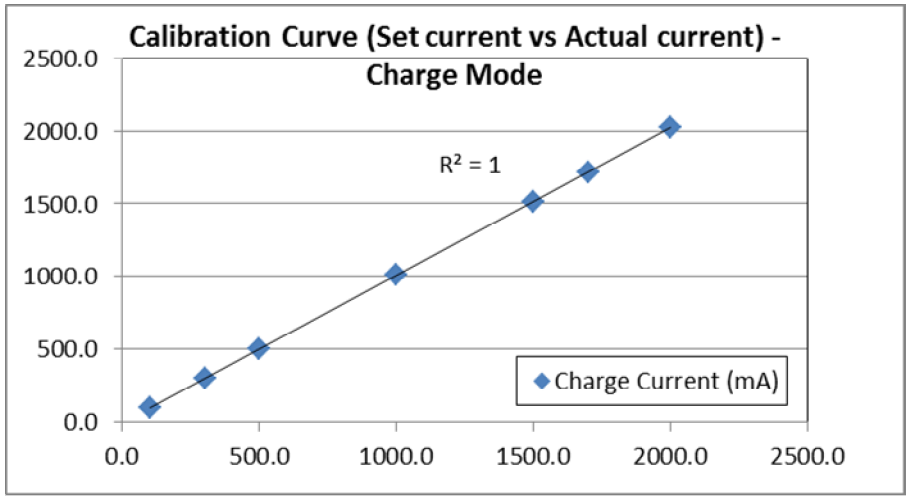

Figure A 5 - Calibration curve at charge mode for charge-discharge unit #3

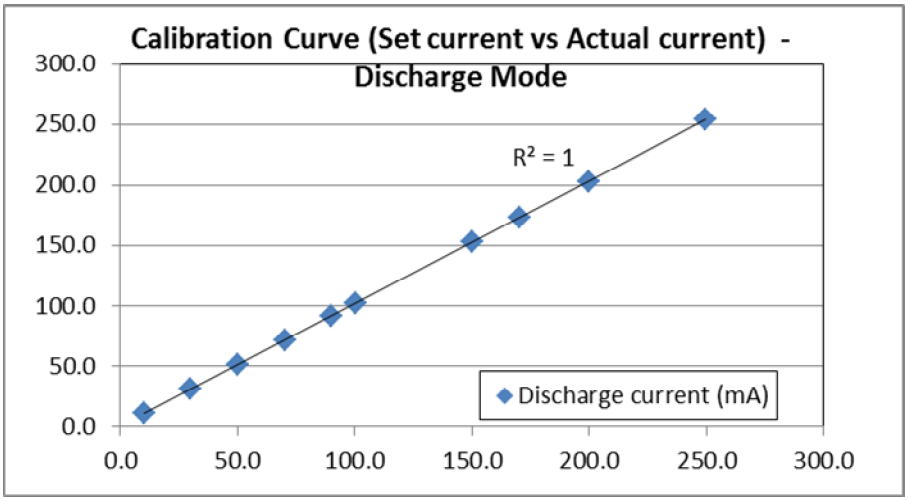

Figure A 6 - Calibration curve at discharge mode for charge-discharge unit #3

Appendix B – Obtained of residual cross-sectional area of the spine and the corrosion layer area from the SEM image of the cross section of the electrode

This appendix illustrated how the residual cross-sectional area of the spine and the corrosion layer area were obtained from the SEM image of the cross section of the electrode using imageJ or iTEM5 image analysis software.

Figure B 1 illustrated of the residual cross-sectional area of an un-cycled spine obtained using iTEM5 image analysis software. Areas shaded represent the residual cross-sectional area of the spine. The active mass of the un-cycled were very loosely

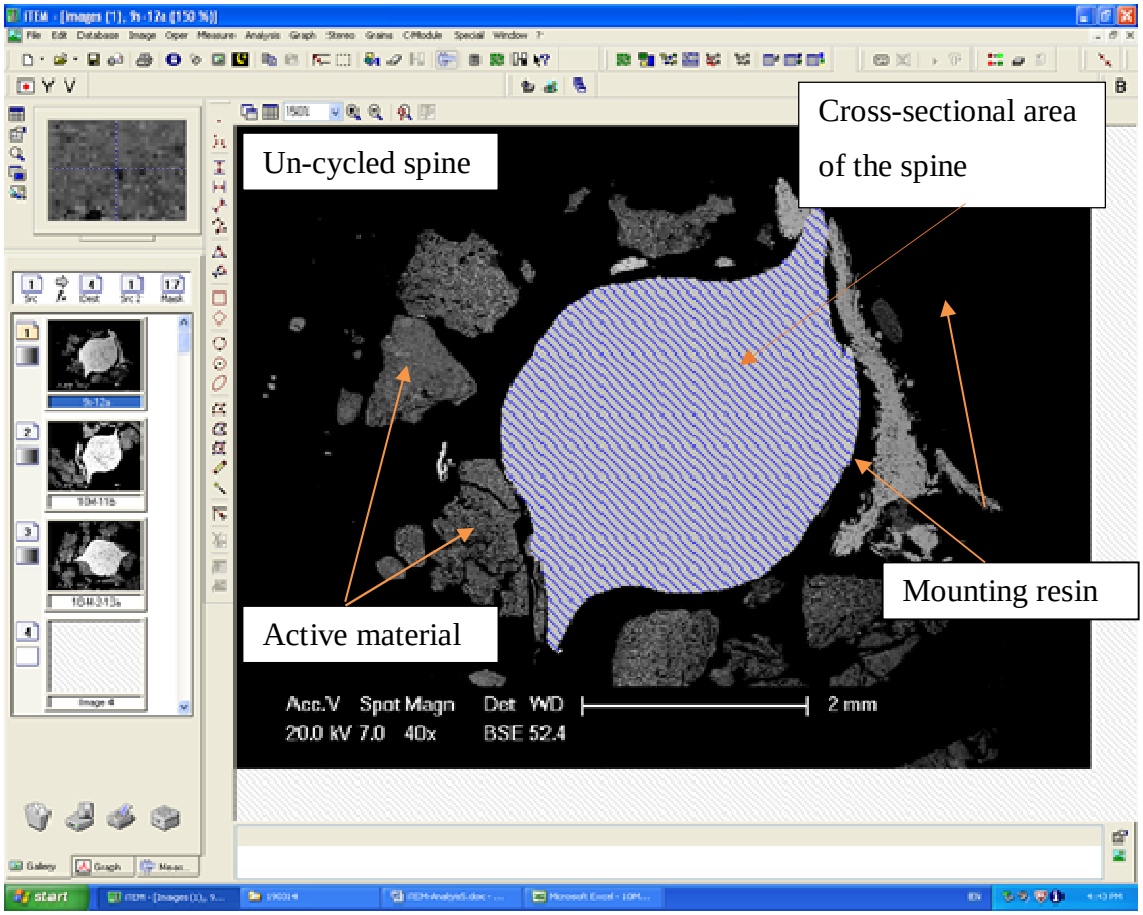

Figure B 1 - Showing cross-sectional area of an un-cycled spine

Figure B 2 illustrated of the residual cross-sectional area of a cycled spine obtained using imageJ software. Areas selected by the yellow dotted line represent the residual cross-sectional area of the spine.

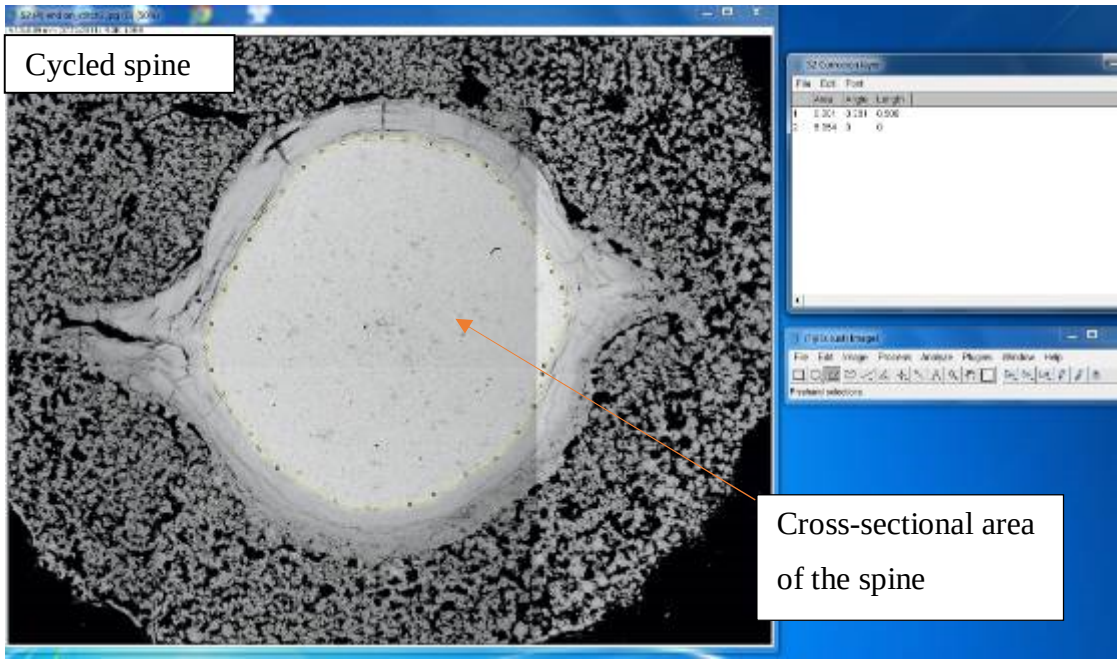

Figure B 2 - A cross-section area of a cycled spine

Figure B3 illustrated of the corrosion layer area of a cycled spine obtained using imageJ software. The area selected by the yellow dotted line represents the total areas of the residual cross-sectional of the spine and the corrosion layer. The area of corrosion layer can be calculated by subtracting the cross-sectional area of the spine (Figure B 2) from the total area (Figure B 3).

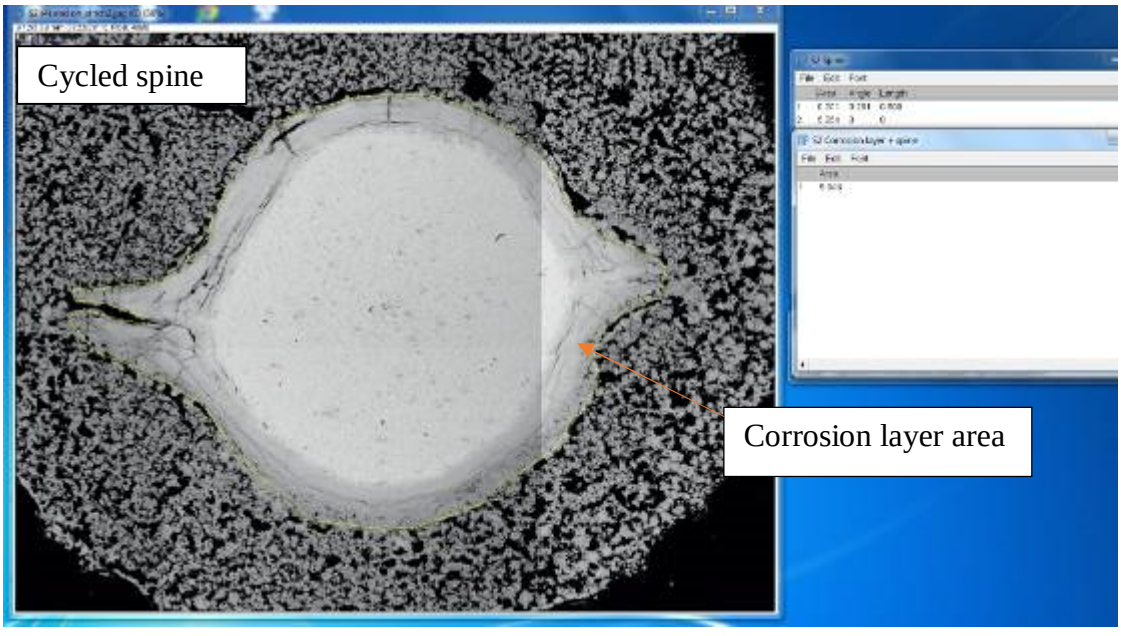

Figure B 3 - Showing total areas of the cross-sectional and the corrosion layer